Spin textures on general surfaces of the correlated topological insulator SmB_6

Pier Paolo Baruselli and Matthias Vojta
Institut für Theoretische Physik, Technische Universität Dresden, 01062 Dresden, Germany
(Received 3 February 2016; published 9 May 2016)

Employing the $\mathbf{k}\cdot\mathbf{p}$ expansion for a family of tight-binding models for SmB_6, we analytically compute topological surface states on a generic (lmn) surface. We show how the Dirac-cone spin structure depends on model ingredients and on the angle θ between the surface normal and the main crystal axes. We apply the general theory to (001), (110), (111), and (210) surfaces, for which we provide concrete predictions for the spin pattern of surface states which we also compare with tight-binding results. As shown in previous work, the spin pattern on a (001) surface can be related to the value of mirror Chern numbers, and we explore the possibility of topological phase transitions between states with different mirror Chern numbers and the associated change of the spin structure of surface states. Such transitions may be accessed by varying either the hybridization between conduction and f electrons or the crystal-field splitting of the low-energy f multiplets, and we compute corresponding phase diagrams. Experimentally, chemical doping is a promising route to realize such transitions.

DOI: 10.1103/PhysRevB.93.195117

I. INTRODUCTION

The material SmB_6 has triggered a large body of research activities recently, given the proposal [1–3] that it realizes a three-dimensional (3D) topological Kondo insulator (TKI). In general, TKIs are strongly correlated systems with f-electron local moments in which a topologically nontrivial band structure emerges at low temperature via Kondo screening [4]. In addition, strong interactions may lead to novel phenomena not present in weakly correlated topological insulators (TIs) such as Bi_2Se_3, etc.

On the experimental front, there is a growing body of results, in particular from transport [5–8] and photoemission studies [9–14], which appear consistent with the hypothesis that SmB_6 indeed realizes a TKI. However, doubts have been raised about the proper interpretation of experimental data [15–17], and recent quantum oscillation measurements have raised a puzzle [18].

Theoretically, band-structure calculations [1,2] confirm SmB_6 to be a strong TI, with $\mathbb{Z}_2$ indices $(\nu_0;\nu_1\nu_2\nu_3) = (1;111)$. In addition, it has been argued [19] that SmB_6 is also a topological crystalline insulator [20], having three nonzero mirror Chern numbers (MCNs), denoted as $\mathcal{C}^+_{k_z=0}$, $\mathcal{C}^+_{k_z=\pi}$, $\mathcal{C}^+_{k_x=k_y}$. While Ref. [19] showed that $\mathcal{C}^+_{k_z=0} = 2 \mod 4$, $\mathcal{C}^+_{k_z=\pi} = 1 \mod 4$, $\mathcal{C}^+_{k_x=k_y} = 1 \mod 2$ independent of band-structure details, recent work [21,22] has demonstrated that the exact values of these MCNs depend on the details of the band structure, with $\mathcal{C}^+_{k_z=\pi} = \pm 1$, $\mathcal{C}^+_{k_z=0} = \pm 2$, and $\mathcal{C}^+_{k_x=k_y} = \pm 1$, giving four possible topological crystalline phases.

Given that the presence of surface states with spin-momentum locking is one of the most characteristic observable properties of TIs, a thorough characterization of these states, also for different surface orientations [23], is of crucial importance. For SmB_6 previous work has mostly focused on the simplest (001) surface, but the combined effects of parity invariants and MCNs promise rich physics on other surfaces, which is mostly unexplored (with notable exceptions in Refs. [18,19,24–26]). We also note that different kinds of spin-momentum locking can lead to different instabilities once electron-electron interactions are considered [27].

The aim of this paper is to close this gap on the theory side: We shall characterize the dispersion and spin structure of the surface states of SmB_6 (and similar materials) for flat surfaces of *general* orientation. To this end, we employ the $\mathbf{k}\cdot\mathbf{p}$ approach, in which an effective Hamiltonian is obtained around the point $X = (0,0,\pi)$ of band inversion. This approach is particularly suitable because it allows to obtain fully analytical results for surface states induced by parity invariants in the limit of small momenta [28]. An obstacle is that the inverted subspace of orbitals couples to the noninverted one due to the low symmetry of a generic (lmn) surface, leading to large matrices which cannot be easily diagonalized. To deal with this, we develop a method which allows one to approximatively compute the effective Hamiltonian on a general surface: by a careful choice of the quantization axis one can find a coordinate system in which the noninverted subspace can be neglected. We compare the results of the $\mathbf{k}\cdot\mathbf{p}$ approach with those from numerical tight-binding calculations and find excellent agreement. In addition, we also discuss the possibility of topological transitions between states with different MCNs [21,22].

On a phenomenological level, this paper extends and generalizes the results of Refs. [21,22] in that it considers generic surfaces; results for the (001) surface will be repeated to lay out the methodology and to give a complete view on the topic. Moreover, the interplay between multiplets is treated in more detail, and the discussion of topological phase transitions is substantially extended with respect to those papers.

A. Summary of results

The first part of the paper is devoted to deriving the low-energy theory for SmB_6 surface states for generic surface orientation. Surface Dirac cones arise from the projection of time-reversal-invariant bulk momenta with inverted bands onto the two-dimensional (2D) surface Brillouin zone (BZ). In SmB_6 bands are inverted at the three bulk X points, yielding in general three Dirac cones of surface states on a (lmn) surface (Fig. 1). To each cone we can assign an angle $\theta \equiv \arctan\sqrt{l^2+m^2}/n$ (and cyclic permutations of l,m,n) with $0 \leqslant \theta \leqslant \pi/2$. For given θ, the effective surface-state

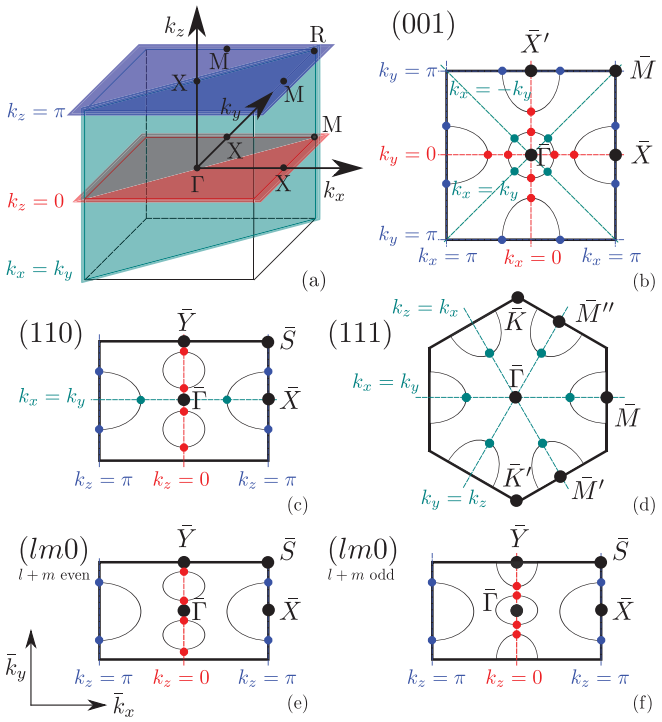

FIG. 1. (a) 3D BZ and mirror planes $k_z = 0$, $k_z = \pi$, $k_x = k_y$; 2D BZ for (b) (001) surface, (c) (011) surface, (d)(111) surface, (e) $(lm0)$ surface, $(l+m)$ even, (f) $(lm0)$ surface, $(l+m)$ odd, and their mirror planes. On all surfaces, $\bar{\Gamma} = (0,0)$; on the (001), $\bar{X} = (\pi,0)$, $\bar{X}' = (0,\pi)$, $\bar{M} = (\pi,\pi)$; on the $(lm0)$, $\bar{X} = (\pi,0)$, $\bar{Y} = (0,\pi/\sqrt{m^2+n^2})$, $\bar{S} = (\pi,\pi/\sqrt{m^2+n^2})$; on the (111), $\bar{K},\bar{K}' = (0,\pm 2\pi\sqrt{2}/3)$, $\bar{M} = (2\pi/\sqrt{6},0)$, $\bar{M}'$, $\bar{M}'' = (\pi/\sqrt{6},\pm\pi/\sqrt{2})$.

Hamiltonian takes the generalized Dirac form

$$H_\theta^{\text{eff}} = -v_y \bar{k}_y \hat{\sigma}_x + v_x \bar{k}_x \hat{\sigma}_y + v_\perp \bar{k}_y \hat{\sigma}_z \equiv \epsilon_{\bar{\mathbf{k}}} \vec{n}_{\bar{\mathbf{k}}} \cdot \vec{\hat{\sigma}}, \quad (1)$$

where $\hat{\sigma}_{x,y,z}$ denote pseudospin operators, $\bar{k}_x$ and $\bar{k}_y$ are momenta parallel to the surface, $\epsilon_{\bar{\mathbf{k}}}$ is the surface-state dispersion, and $v_x, v_y, v_\perp$ are velocities which depend on microscopic parameters and on θ. The unit vector $\vec{n}_{\bar{\mathbf{k}}}$ encodes the direction of the pseudospin for states with positive energy. Its winding number [21,22] $\bar{w}_d \equiv \text{sgn}(v_x v_y)$, which takes a value ± 1 according to the sense of rotation of the pseudospin with respect to momentum, is determined in a nontrivial way by MCNs, model parameters, and the angle θ. However, simplifications occur if the parameter $w = \text{sgn}(\mathcal{C}^+_{k_z=0}\mathcal{C}^+_{k_z=\pi})$, characterizing the topological crystalline phase, is $w = +1$, as suggested [21] by experimental results [14] on SmB_6. In this case, we find that all Dirac cones have a positive winding number $\bar{w}_d = +1$; the same holds for the winding of the physical spin.

In the second part of the paper, we demonstrate how to access topological phase transition between phases with different $w = \pm 1$ by tuning the hybridization term or the crystal-field splitting. We illustrate this scenario by use of numerical diagonalization of tight-binding models, derive relevant phase diagrams, and discuss the observable signatures of the transitions in terms of changes of the surface states. Interestingly, the relevant models also admit phases with higher MCNs, albeit in small windows of parameters. We argue that chemical doping may change the crystal-field splitting in order to drive a topological transition in SmB_6.

B. Outline

The remainder of the paper is organized as follows. General aspects of the employed band-structure model are described in Sec. II. In Sec. III, we derive the $\mathbf{k}\cdot\mathbf{p}$ Hamiltonian which we use to compute surface states on the (001) surface in Secs. IV and V. In Sec. VI, we apply the $\mathbf{k}\cdot\mathbf{p}$ treatment to general surfaces. Section VII is devoted to topological phase transitions between phases with opposite w. The paper closes with concluding remarks in Sec. VIII. Longer derivations are relegated to the Appendixes.

II. MODELING

In this section, we provide information about the orbital basis which our model is built upon, as well as definitions of the pseudospin and of related quantitites.

A. Orbital basis

SmB_6 crystallizes in the simple cubic (SC) structure, with a SC BZ [see Fig. 1(a)]. *Ab initio* calculations [2,29,30] show that only bands arising from Sm orbitals are close to the Fermi energy, and, in particular, a total of 10 rare-earth orbitals per site are needed for a correct tight-binding description [31], namely, the spin-degenerate E_g ($d_{x^2-y^2}$ and d_{z^2}) quadruplet and the lowest-lying f-shell $j = \frac{5}{2}$ multiplet. Other orbitals, including the Sm $j = \frac{7}{2}$ multiplet and all B_6 states, are excluded since their energies are far away from the Fermi level. The cubic crystal field splits the $j = \frac{5}{2}$ multiplet into a Γ_8 quadruplet and a Γ_7 doublet, which can be expressed in terms of $|j_z\rangle$ states as $|\Gamma_8^{(1)}\pm\rangle = \sqrt{\frac{5}{6}}|\pm\frac{5}{2}\rangle + \sqrt{\frac{1}{6}}|\mp\frac{3}{2}\rangle$, $|\Gamma_8^{(2)}\pm\rangle = |\pm\frac{1}{2}\rangle$, $|\Gamma_7\pm\rangle = \sqrt{\frac{1}{6}}|\pm\frac{5}{2}\rangle - \sqrt{\frac{5}{6}}|\mp\frac{3}{2}\rangle$, where $\pm$ denotes a pseudospin index. For the d states, the effect of spin-orbit coupling will be neglected.

In what follows, we abbreviate $d^1 \equiv d_{x^2-y^2}$, $d^2 \equiv d_{z^2}$, $f^1 \equiv \Gamma_8^{(1)}$, $f^2 \equiv \Gamma_8^{(2)}$, $f^7 \equiv \Gamma_7$, so the basis of our Hamiltonian is $|d^1\uparrow\rangle, |d^1\downarrow\rangle, |d^2\uparrow\rangle, |d^2\downarrow\rangle, |f^1+\rangle, |f^1-\rangle, |f^2+\rangle, |f^2-\rangle, |f^7+\rangle, |f^7-\rangle$.

B. Symmetries

The time-reversal operator $T \equiv -2i\hat{S}_y K$, where $\hat{S}_y$ acts on the spin variable and K is the complex conjugation, acts on this basis as

$$T|d^m\sigma\rangle = -i\sigma_y|d^m\sigma'\rangle, \quad m = 1,2;\ \sigma,\sigma' = \uparrow,\downarrow \quad (2)$$

$$T|f^m\sigma\rangle = +i\sigma_y|f^m\sigma'\rangle, \quad m = 1,2,7;\ \sigma,\sigma' = \pm \quad (3)$$

where $\sigma_y \equiv (\sigma_y)_{\sigma\sigma'}$ acts on the subspace spanned by $\sigma,\sigma' = \uparrow,\downarrow$ for d states, or by $\sigma,\sigma' = +,-$ for f states.

Mirror-symmetry operators $M_l \equiv PC_2(l)$, where P is the inversion and $C_2(l)$ is a twofold rotation around axis l, act

as [21]

$$M_l|d^m\sigma\rangle = -i\sigma_l|d^m\sigma'\rangle, \quad m = 1,2 \tag{4}$$

$$M_l|f^m\sigma\rangle = +i\sigma_l|f^m\sigma'\rangle, \quad m = 1,2,7 \tag{5}$$

where $l = x,y,z$; moreover,

$$M_{x\pm y}|d^1\sigma\rangle = +i\sigma_{x\pm y}|d^1\sigma'\rangle, \tag{6}$$

$$M_{x\pm y}|d^2\sigma\rangle = -i\sigma_{x\pm y}|d^2\sigma'\rangle, \tag{7}$$

$$M_{x\pm y}|f^m\sigma\rangle = -i\sigma_{x\pm y}|f^m\sigma'\rangle, \quad m = 1,7 \tag{8}$$

$$M_{x\pm y}|f^m\sigma\rangle = +i\sigma_{x\pm y}|f^m\sigma'\rangle, \quad m = 2 \tag{9}$$

where $\sigma_{x\pm y} = (\sigma_x \pm \sigma_y)/\sqrt{2}$.

MCNs are defined as [19,21,22]

$$\mathcal{C}^{\pm}_{\overline{\mathrm{BZ}}} = \frac{i}{2\pi}\sum_{a,b=1}^{2}\epsilon_{ab}\sum_{n=1}^{N}\int_{\overline{\mathrm{BZ}}} d^2\mathbf{k}\langle\partial_a u^{\pm}_n(\mathbf{k})|\partial_b u^{\pm}_n(\mathbf{k})\rangle, \tag{10}$$

with $M|u^{\pm}_n(\mathbf{k})\rangle = \pm i|u^{\pm}_n(\mathbf{k})\rangle$, and where $\mathbf{k}$ lies in the plane $\overline{\mathrm{BZ}}$ which is invariant with respect to the symmetry operator M ($M = M_z$ when $\overline{\mathrm{BZ}}$ is $k_z = 0$ or $k_z = \pi$, $M = M_{x-y}$ when $\overline{\mathrm{BZ}}$ is $k_x = k_y$), and we sum over all N occupied bands. We note that $\mathcal{C}^{+}_{\overline{\mathrm{BZ}}} + \mathcal{C}^{-}_{\overline{\mathrm{BZ}}} = 0$ and, by cubic symmetry, $\mathcal{C}^{+}_{k_z=0} = \mathcal{C}^{+}_{k_x=0} = \mathcal{C}^{+}_{k_y=0}$, etc.

As remarked, four phases are possible, each characterized by the triplet of numbers $(\mathcal{C}^{+}_{k_z=0},\mathcal{C}^{+}_{k_z=\pi},\mathcal{C}^{+}_{k_x=k_y})$: $(\pm 2, +1, \pm 1)$. Since the sign of MCNs fixes the mirror-symmetry eigenvalues of surface states [32], each phase has different surface-state properties as shown in Refs. [21,22] (see Sec. VI). For SmB_6, the results of Ref. [21] can be written in a concise form using v and w:

$$v \equiv \mathrm{sgn}(\mathcal{C}^{+}_{k_z=0}\mathcal{C}^{+}_{k_x=k_y}), \tag{11}$$

$$w \equiv \mathrm{sgn}(\mathcal{C}^{+}_{k_z=0}\mathcal{C}^{+}_{k_z=\pi}). \tag{12}$$

For (001) surface states $|\phi^{+}(\mathbf{k})\rangle$ of positive energies, i.e., above the Dirac energy, on the $\bar{\Gamma}$ cone the following relations are then satisfied:

$$M_y|\phi^{+}_{\bar{\Gamma}}(|k_x|,0)\rangle = -iw|\phi^{+}_{\bar{\Gamma}}(|k_x|,0)\rangle, \tag{13}$$

$$M_{x-y}|\phi^{+}_{\bar{\Gamma}}(k_x = k_y > 0)\rangle = +ivw|\phi^{+}_{\bar{\Gamma}}(k_x = k_y > 0)\rangle, \tag{14}$$

$$M_x|\phi^{+}_{\bar{\Gamma}}(0,|k_y|)\rangle = +iw|\phi^{+}_{\bar{\Gamma}}(0,|k_y|)\rangle, \tag{15}$$

while on the $\bar{X}$ cone,

$$M_x|\phi^{+}_{\bar{X}}(0,|k_y|)\rangle = +i|\phi^{+}_{\bar{X}}(0,|k_y|)\rangle, \tag{16}$$

$$M_y|\phi^{+}_{\bar{X}}(-|k_x|,0)\rangle = +iw|\phi^{+}_{\bar{X}}(-|k_x|,0)\rangle, \tag{17}$$

and on the $\bar{X}'$ one,

$$M_y|\phi^{+}_{\bar{X}'}(|k_x|,0)\rangle = -i|\phi^{+}_{\bar{X}'}(|k_x|,0)\rangle, \tag{18}$$

$$M_x|\phi^{+}_{\bar{X}'}(0,-|k_y|)\rangle = -iw|\phi^{+}_{\bar{X}'}(0,-|k_y|)\rangle. \tag{19}$$

C. Relation between spin and pseudospin

We start with remarks on notation. With σ_i ($i = x,y,z,0$) we denote the standard Pauli matrices for (pseudo)spin indices, i.e., for d states they act in the space of $\uparrow$, $\downarrow$, while for f states they act in the space of $+,-$. With $\hat{s}_i$ ($i = x,y,z,0$) we denote Pauli matrices for operators acting into an arbitrary two-dimensional space, which is typically the space spanned by the doublet of surface states at $k_\parallel = 0$. With $\hat{S}_i$ ($i = x,y,z$) we denote physical spin operators, with separate contributions from the d ($\hat{S}^d_i$) and f shells ($\hat{S}^f_i$). With $\hat{\sigma}_i$ ($i = x,y,z$) we denote pseudospin operators, still with separate contributions from the d ($\hat{\sigma}^d_i$) and f shells ($\hat{\sigma}^f_i$), and defined as follows.

For d electrons, with spin-orbit coupling neglected, we take the pseudospin to coincide with the physical spin, apart from a factor 2: $2\hat{S}^d_i = \hat{\sigma}^d_i$. For $d_{x^2-y^2}$ states we have in the $|d^1\uparrow\rangle$, $|d^1\downarrow\rangle$ basis

$$\hat{\sigma}^d_x = \begin{pmatrix}0 & 1\\ 1 & 0\end{pmatrix}, \quad \hat{\sigma}^d_y = \begin{pmatrix}0 & -i\\ i & 0\end{pmatrix}, \quad \hat{\sigma}^d_z = \begin{pmatrix}1 & 0\\ 0 & -1\end{pmatrix}. \tag{20}$$

For f electrons, the physical spin in the $\Gamma^{(1)}_8$-$\Gamma^{(2)}_8$-Γ_7 basis is given in Appendix F. If we restrict to $\Gamma^{(1)}_8$ states, we have in the $|f^1+\rangle, |f^1-\rangle$ basis

$$2\hat{S}^f_x = \frac{5}{21}\begin{pmatrix}0 & -1\\ -1 & 0\end{pmatrix}, \quad 2\hat{S}^f_y = \frac{5}{21}\begin{pmatrix}0 & i\\ -i & 0\end{pmatrix},$$
$$2\hat{S}^f_z = \frac{11}{21}\begin{pmatrix}-1 & 0\\ 0 & 1\end{pmatrix}. \tag{21}$$

In the same basis, we take as pseudospin

$$\hat{\sigma}^f_x = \begin{pmatrix}0 & -1\\ -1 & 0\end{pmatrix}, \quad \hat{\sigma}^f_y = \begin{pmatrix}0 & i\\ -i & 0\end{pmatrix}, \quad \hat{\sigma}^f_z = \begin{pmatrix}-1 & 0\\ 0 & 1\end{pmatrix}, \tag{22}$$

that is, we get rid of the prefactors with respect to the real spin. As a consequence, for $\Gamma^{(1)}_8$ states, the spin is parallel to the pseudospin with direction-dependent coefficients 5/21 or 11/21. For Γ_7 states, Eq. (22) continues to apply, whereas all the prefactors in Eq. (21) become $-5/21$, such that spin and pseudospin are antiparallel. We note that the minus sign appearing in our definition of the pseudospin with respect to the standard Pauli matrices is linked to the different behavior of d and f states under mirror operators [see Eqs. (4) and (5)]. Indeed, we can write $M_l = -i\hat{\sigma}_l$, and, as shown in Ref. [22], once the pseudospin has this defined mirror-symmetry property, MCNs fix its texture on surface states.

We also stress that the expectation value of the pseudospin $|\langle\vec{\hat{\sigma}}\rangle|$ is always normalized to unity on surface states, while that of the physical spin $\vec{\hat{S}}$ has no definite normalization, but $|\langle\vec{\hat{S}}\rangle| \leqslant \frac{1}{2}$ holds, with the equal sign for pure d states. Hence, it is often useful to use pseudospin rather than spin operators. In the course of the paper, we will always refer to both quantities, bearing in mind that experiments must be compared to results for the physical spin.

It is also possible to take into account the expectation value of the orbital angular momentum; as shown in Appendix F,

this is zero in the d shell, and equal to (-8) times the spin expectation value in the f shell. We will not refer to this quantity in the rest of the paper.

III. k · p HAMILTONIAN

In this section, we derive the $\mathbf{k}\cdot\mathbf{p}$ Hamiltonian by expanding the tight-binding Hamiltonian of Ref. [31] around $X=(0,0,\pi)$. We measure bulk momenta $\mathbf{k}$ relative to X and keep all first-order terms in k_x,k_y,k_z and all mixed terms up to second order. Even though the lattice is cubic, the $\mathbf{k}\cdot\mathbf{p}$ Hamiltonian has tetragonal symmetry, as dictated by the momentum-space location of X.

We will exclusively work in a renormalized single-particle picture, based on the assumption that many-body effects can be captured by proper renormalizations of single-particle terms, in particular the f kinetic energy and hybridization [33]. For band structures, this assumption has been confirmed by many-body numerical techniques [34,35].

A. Full orbital basis

In the 10-dimensional basis $|d^1\uparrow\rangle$, $|d^1\downarrow\rangle$, $|d^2\uparrow\rangle$, $|d^2\downarrow\rangle$, $|f^1+\rangle$, $|f^1-\rangle$, $|f^2+\rangle$, $|f^2-\rangle$, $|f^7+\rangle$,$|f^7-\rangle$ of bulk Bloch states, the result is as follows:

$$H=\left(\begin{array}{cccc|cccccc}
\epsilon_1^d(\mathbf{k}) & 0 & 0 & 0 & -iVf_1^vk_z & -iVh_1^vk_- & 0 & -iVh_{12}^vk_+ & -iVf_7^vk_z & -iVh_7^vk_- \\
0 & \epsilon_1^d(\mathbf{k}) & 0 & 0 & -iVh_1^vk_+ & iVf_1^vk_z & -iVh_{12}^vk_- & 0 & -iVh_7^vk_+ & iVf_7^vk_z \\
0 & 0 & \epsilon_2^d(\mathbf{k}) & 0 & 0 & -iVh_{21}^vk_+ & -iVf_2^vk_z & -iVh_2^vk_- & 0 & -iVh_{72}^vk_+ \\
0 & 0 & 0 & \epsilon_2^d(\mathbf{k}) & -iVh_{21}^vk_- & 0 & -iVh_2^vk_+ & iVf_2^vk_z & -iVh_{72}^vk_- & 0 \\
\hline
iVf_1^vk_z & iVh_1^vk_- & 0 & iVh_{21}^vk_+ & \epsilon_1^f(\mathbf{k}) & 0 & 0 & 0 & m_{78} & 0 \\
iVh_1^vk_+ & -iVf_1^vk_z & iVh_{21}^vk_- & 0 & 0 & \epsilon_1^f(\mathbf{k}) & 0 & 0 & 0 & m_{78} \\
0 & iVh_{12}^vk_+ & iVf_2^vk_z & iVh_2^vk_- & 0 & 0 & \epsilon_2^f(\mathbf{k}) & 0 & 0 & 0 \\
iVh_{12}^vk_- & 0 & iVh_2^vk_+ & -iVf_2^vk_z & 0 & 0 & 0 & \epsilon_2^f(\mathbf{k}) & 0 & 0 \\
iVf_7k_z & iVh_7^vk_- & 0 & iVh_{72}k_+ & m_{78} & 0 & 0 & 0 & \epsilon_7^f(\mathbf{k}) & 0 \\
iVh_7^vk_+ & -iVf_7k_z & iVh_{72}k_- & 0 & 0 & m_{78} & 0 & 0 & 0 & \epsilon_7^f(\mathbf{k})
\end{array}\right) \tag{23}$$

with $k_\pm\equiv k_x\pm ik_y$. Kinetic energy terms are diagonal, and given by

$$\epsilon_i^d(\mathbf{k})=\epsilon_i^d-t_d\left[k_z^2g_i^d+k_\parallel^2l_i^d\right],\quad i=1,2 \tag{24}$$

$$\epsilon_i^f(\mathbf{k})=\epsilon_i^f-t_f\left[k_z^2g_i^f+k_\parallel^2l_i^f\right],\quad i=1,2,7 \tag{25}$$

with $k_\parallel^2\equiv k_x^2+k_y^2$, $t_d>0$ (electronlike), $t_f<0$ (holelike). The g_i and l_i represent combinations of tight-binding parameters and are defined in Appendix A. At zeroth order, we have a coupling m_{78} between $\Gamma_8^{(1)}$ and Γ_7:

$$m_{78}=-4\eta_{78}^{f1}+8\eta_{x7}^{f2}>0. \tag{26}$$

Hybridization terms are nondiagonal; we will need the following ones:

$$f_1^v=2\eta_x^{v1}+2\eta_x^{v2}+6\eta_z^{v2}>0, \tag{27}$$

$$f_2^v=2\eta_z^{v1}+6\eta_x^{v2}+2\eta_z^{v2}<0, \tag{28}$$

$$f_7^v=2\eta_7^{v1}-4\sqrt{3}\eta_7^{v2}-4\eta_{x7}^{v2}<0, \tag{29}$$

$$h_1^v=-\tfrac{1}{2}\eta_x^{v1}-\tfrac{3}{2}\eta_z^{v1}-3\eta_x^{v2}+3\eta_z^{v2}>0, \tag{30}$$

$$h_2^v=-\tfrac{3}{2}\eta_x^{v1}-\tfrac{1}{2}\eta_z^{v1}+3\eta_x^{v2}-3\eta_z^{v2}<0, \tag{31}$$

$$h_7^v=\eta_7^{v1}+2\sqrt{3}\eta_7^{v2}-6\eta_{x7}^{v2}>0. \tag{32}$$

The explicit form of other terms appearing in the Hamiltonian (23), which are not needed in what follows, is given in Appendix A, together with the meaning of different tight-binding parameters η. We also provide numerical values for some of these parameters, extracted from density-functional-theory (DFT) calculations of Refs. [30,31] for PuB_6, which has a band structure very similar to SmB_6. In the rest of the paper we will not rely on the exact parameter values, but will often make use of (relative) signs, as indicated in Eqs. (26)–(32).

B. Reduced orbital basis

To enable analytical calculations, we will need to work with matrices of dimension (at most) 4×4. This requires a further basis reduction (and associated approximations), and we discuss different possible choices in turn. The best choice will depend on microscopic parameters, in particular the crystal-field splitting between Γ_7 and Γ_8 multiplets.

We may either retain Γ_8 states and work in subspace 1, spanned by $|d^1\uparrow\rangle$,$|d^1\downarrow\rangle$,$|f^1+\rangle$,$|f^1-\rangle$ states [see Fig. 2(a)]. The Hamiltonian becomes

$$H^{(1)}=\left(\begin{array}{cc|cc}
\epsilon_1^d(\mathbf{k}) & 0 & -iVf_1^vk_z & -iVh_1^vk_- \\
0 & \epsilon_1^d(\mathbf{k}) & -iVh_1^vk_+ & iVf_1^vk_z \\
\hline
iVf_1^vk_z & iVh_1^vk_- & \epsilon_1^f(\mathbf{k}) & 0 \\
iVh_1^vk_+ & -iVf_1^vk_z & 0 & \epsilon_1^f(\mathbf{k})
\end{array}\right). \tag{33}$$

Alternatively, we may retain Γ_7 states yielding subspace $1'$, spanned by $|d^1\uparrow\rangle$,$|d^1\downarrow\rangle$,$|f^7+\rangle$,$|f^7-\rangle$ [see Fig. 2(b)]. The Hamiltonian is

$$H^{(1')}=\left(\begin{array}{cc|cc}
\epsilon_1^d(\mathbf{k}) & 0 & -iVf_7^vk_z & -iVh_7^vk_- \\
0 & \epsilon_1^d(\mathbf{k}) & -iVh_7^vk_+ & iVf_7^vk_z \\
\hline
iVf_7^vk_z & iVh_7^vk_- & \epsilon_7^f(\mathbf{k}) & 0 \\
iVh_7^vk_+ & -iVf_7^vk_z & 0 & \epsilon_7^f(\mathbf{k})
\end{array}\right). \tag{34}$$

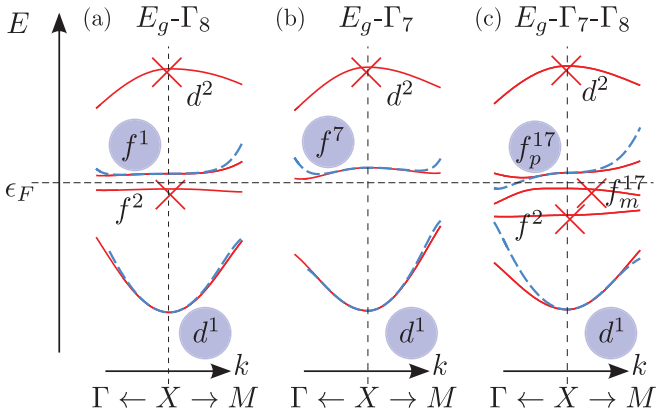

FIG. 2. Schematic bulk band structure around X illustrating the approximation schemes; shown are tight-binding dispersions (solid red) and the $\mathbf{k}\cdot\mathbf{p}$ approximation with four states (dotted blue) (for details, see text). (a) Out of E_g and Γ_8 (eight total states), we keep $d^1 \equiv d_{x^2-y^2}$ and $f^1 \equiv \Gamma_8^{(1)}$, and neglect $d^2 \equiv d_{z^2}$ and $f^2 \equiv \Gamma_8^{(2)}$, which are not inverted. (b) Out of E_g and Γ_7 (six total states), we keep d^1 and $f^7 \equiv \Gamma_7$, and neglect d^2. (c) Out of E_g, Γ_7, and Γ_8 (10 total states), we keep d^1 and the linear combination f_p^{17} of f^1 and f^7 of higher energy, and neglect states d^2, f^2, and the linear combination f_m^{17} of lower energy, which is inverted, but remains below the Fermi energy ϵ_F. All states are twice (pseudo)spin degenerate.

When using both Γ_7 and Γ_8 states, we will just retain the linear combination $|f_p^{17}\pm\rangle$ of $|f^1\pm\rangle$ and $|f^7\pm\rangle$ of higher energy, giving

$$H^{(1)''}=\left(\begin{array}{cc|cc} \epsilon_1^d(\mathbf{k}) & 0 & -iVf_{17}^v k_z & -iVh_{17}^v k_- \\ 0 & \epsilon_1^d(\mathbf{k}) & -iVh_{17}^v k_+ & iVf_{17}^v k_z \\ \hline iVf_{17}^v k_z & iVh_{17}^v k_- & \epsilon_{17}^f(\mathbf{k}) & 0 \\ iVh_{17}^v k_+ & -iVf_{17}^v k_z & 0 & \epsilon_{17}^f(\mathbf{k}) \end{array}\right) \tag{35}$$

with explicit expressions of $f_{17}^v, h_{17}^v, \epsilon_{17}^f(\mathbf{k})$ given in Sec. IV C [see Fig. 2(c)].

Matrices (33), (34), and (35) have the same cylindrical symmetry and the same form, but different parameters. In the kinetic energy sector they are all similar, in that parameters $g_1^d, l_{1,7}^d$ have always a negative sign, indicating the curvature of the band at X: upward for d states, since $(-t_d)$ is negative, and downward for f states, since $(-t_f)$ is positive [see Eqs. (24) and (25)]. However, they differ in the hybridization sector since parameters f_i^v and h_i^v can have all different signs, that we will later link to the topological properties of SmB_6 and to the spin pattern of surface states.

It is also sometimes useful to consider the Hamiltonian in subspace 2, spanned by $|d^2\uparrow\rangle, |d^2\downarrow\rangle, |f^2+\rangle, |f^2-\rangle$:

$$H^{(2)}=\left(\begin{array}{cc|cc} \epsilon_2^d(\mathbf{k}) & 0 & -iVf_2^v k_z & -iVh_2^v k_- \\ 0 & \epsilon_2^d(\mathbf{k}) & -iVh_2^v k_+ & iVf_2^v k_z \\ \hline iVf_2^v k_z & iVh_2^v k_- & \epsilon_2^f(\mathbf{k}) & 0 \\ iVh_2^v k_+ & -iVf_2^v k_z & 0 & \epsilon_2^f(\mathbf{k}) \end{array}\right). \tag{36}$$

Subspace 2 is not inverted, hence not relevant for topological properties. However, Hamiltonian parameters can be tuned [3] to achieve band inversion in this subspace instead of subspace 1, thus, it is instructive to see how this (experimentally irrelevant) situation compares to the others.

We note that subspaces 1 and 1′ together, including both Γ_7 and Γ_8 states, form a six-dimensional space corresponding to $j_z = \pm\frac{3}{2}$, while subspace 2 is four dimensional and corresponds to $j_z = \pm\frac{1}{2}$.

C. Relation to earlier work

A Hamiltonian similar to Eq. (23) was introduced in Ref. [36], with a few differences. First, the d_{z^2} orbital was neglected, reducing the Hilbert space to eight orbitals, this is a meaningful approximation since this orbital is far from the Fermi energy and not involved in the band inversion. Second, instead of working with Γ_7 and Γ_8 states, the authors used eigenstates of the j_z operator, which is just a basis rotation. Finally, the spirit is different: here we derive the Hamiltonian from a tight-binding model constructed from DFT results, and we stress how different parameters affect the effective Hamiltonian, rather than taking numerical values directly from DFT. This leads to a better understanding of how different tight-binding terms affect the topological properties of SmB_6. Taking into account these differences, our approach is compatible with that of Ref. [36], even though we reach a different conclusion about the spin structure on the (001) surface, most likely due to quantitative difference in the numerical value of parameters (see Sec. V).

An approach similar to ours is followed in Ref. [37], where, however, the starting tight-binding model is different; we will return to this point in Sec. IV. In addition, the authors do not focus on the spin structure of surface states, which instead is our primary goal.

IV. EXPANSION AROUND $\bar{\Gamma}$ FOR (001) SURFACE

In this section, we demonstrate the usage of the $\mathbf{k}\cdot\mathbf{p}$ Hamiltonian of Sec. III to compute the effective surface-state Hamiltonian for the Dirac cone at $\bar{\Gamma}$ of a (001) surface. The method consists of finding surface states in the form of a Kramers doublet exactly at $\bar{\Gamma}$, i.e., setting $k_{x,y} = 0$, and then expanding in $k_{x,y}$ to build an effective Hamiltonian for finite $k_{x,y}$ onto the $k_{x,y} = 0$ basis. This is a standard approach in the theory of weakly correlated TIs (see, e.g., Ref. [28]). We will always assume ideal surfaces, i.e., a confining potential which is zero inside the crystal and infinite outside; for details, see Appendixes B and C.

A. E_g-Γ_8 basis

First, we concentrate on E_g and Γ_8 states, i.e., we neglect the Γ_7 states in columns and rows 9 and 10 of Eq. (23). Setting $k_x = k_y = 0$ defines an unperturbed Hamiltonian H_0. It splits into four 2×2 blocks, that we call $H_0^{+(1)}$ with basis $|d^1\uparrow\rangle, |f^1+\rangle$, $H_0^{-(1)}$ with basis $|d^1\downarrow\rangle, |f^1-\rangle$, $H_0^{+(2)}$ with basis $|d^2\uparrow\rangle, |f^2+\rangle$, $H_0^{-(2)}$ with basis $|d^2\downarrow\rangle, |f^2-\rangle$. The fact that there are no terms connecting $H_0^{+/-(1)}$ to $H_0^{+/-(2)}$ is a direct consequence of tetragonal symmetry along the Γ-X direction, and will always be true, even keeping more terms in the Hamiltonian. After finding surface states for $H_0^{(1)}$, we take the Hamiltonian $H_P \equiv H - H_0$, containing all terms in $k_{x,y}$, as a perturbation to get the effective Hamiltonian as a function of $k_{x,y}$.

For the unperturbed Hamiltonian $H_0^{(1,2)}$ blocks, within our model, we get

$$H_0^{+(1,2)} = \begin{pmatrix} \epsilon_{1,2}^d - t_d k_z^2 g_{1,2}^d & -iVk_z f_{1,2}^v \\ iVk_z f_{1,2}^v & \epsilon_{1,2}^f - t_f k_z^2 g_{1,2}^f \end{pmatrix}, \tag{37}$$

while the other two blocks $H_0^{-(1,2)}$ are obtained by substituting V with $(-V)$. As shown in Appendix B, it is possible to analytically compute surface states at $k_{x,y} = 0$. Those exist only in the subspace where band inversion is achieved, that is, in subspace 1 as defined in Sec. III B, since $\epsilon_1^d < \epsilon_1^f$ and $\epsilon_2^d > \epsilon_2^f$. After tracing out the z coordinate of the wave function, they read as

$$\begin{aligned} |\psi_+\rangle &= \alpha|d^1\uparrow\rangle + \beta|f^1+\rangle, \\ |\psi_-\rangle &= \alpha|d^1\downarrow\rangle - \beta|f^1-\rangle, \end{aligned} \tag{38}$$

where the ket vectors are now Bloch states carrying a two-dimensional surface momentum, and

$$\alpha = \sqrt{\frac{t_f g_1^f}{t_f g_1^f - t_d g_1^d}}, \tag{39}$$

$$\beta = -\operatorname{sgn}\left(V f_1^v\right)\sqrt{\frac{t_d g_1^d}{t_d g_1^d - t_f g_1^f}}. \tag{40}$$

We stress that α and β can both be chosen real, with $\alpha^2 + \beta^2 = 1$, and $\beta^2/\alpha^2 \sim |t_d/t_f| \gg 1$, hence, surface states have mainly f character.

After finding surface states at $k_{x,y} = 0$, we can consider the perturbing Hamiltonian, given in Appendix B, and build an effective 2×2 Hamiltonian via

$$H_{\bar{\Gamma}}^{\text{eff}} = \begin{pmatrix} \langle\psi_+|H_P|\psi_+\rangle & \langle\psi_+|H_P|\psi_-\rangle \\ \langle\psi_-|H_P|\psi_+\rangle & \langle\psi_-|H_P|\psi_-\rangle \end{pmatrix} \tag{41}$$

to find

$$H_{\bar{\Gamma}}^{\text{eff}} = |v_0|w'(k_x\hat{s}_y - k_y\hat{s}_x), \tag{42}$$

$$|v_0| \equiv 2\left|Vh_1^v\right|\frac{\sqrt{-t_d t_f g_1^d g_1^f}}{t_f g_1^f - t_d g_1^d}, \tag{43}$$

$$w' \equiv -\operatorname{sgn}\left(\alpha\beta V h_1^v\right) = \operatorname{sgn}\left(f_1^v h_1^v\right) = \pm 1, \tag{44}$$

where $\hat{s}_x, \hat{s}_y, \hat{s}_z$ are Pauli matrices in the $|\psi_\pm\rangle$ basis.

Evaluating the spin expectation values (SEV) in the basis (38) yields

$$2\langle\vec{\hat{S}}\rangle = 2\langle(\hat{S}_x, \hat{S}_y, \hat{S}_z)\rangle = (\gamma_5^+\hat{s}_x, \gamma_5^+\hat{s}_y, \gamma_{11}^-\hat{s}_z), \tag{45}$$

where we introduce

$$\gamma_5^\pm = \alpha^2 \pm \frac{5}{21}\beta^2, \quad \gamma_{11}^\pm = \alpha^2 \pm \frac{11}{21}\beta^2, \tag{46}$$

with the properties $\gamma_5^+, \gamma_{11}^+ > 0$ and $\gamma_5^-, \gamma_{11}^- < 0$ since $\alpha^2 \ll \beta^2$. For the pseudospin we find

$$\langle\vec{\hat{\sigma}}\rangle = \langle(\hat{\sigma}_x, \hat{\sigma}_y, \hat{\sigma}_z)\rangle = (\hat{s}_x, \hat{s}_y, \gamma^-\hat{s}_z), \tag{47}$$

with $\gamma^- = \alpha^2 - \beta^2 < 0$. This shows that we can substitute $\hat{s}_x$ and $\hat{s}_y$ in Eq. (42) exactly with pseudospin operators $\hat{\sigma}_x$ and $\hat{\sigma}_y$ or approximatively with spin operators $\hat{S}_x$ and $\hat{S}_y$. This justifies what we did in Ref. [21], where we wrote the effective Hamiltonian directly in terms of spin operators once knowing the SEV from mirror-symmetry eigenvalues.

We can now easily diagonalize Eq. (42); the state $|\phi^+(\mathbf{k})\rangle$ at a given momentum $\mathbf{k} = (k_x, k_y)$ with positive energy $\epsilon_k = +|v_0|k$ ($k = |\mathbf{k}|$) has the SEV

$$2\langle\phi^+(\mathbf{k})|\vec{\hat{S}}|\phi^+(\mathbf{k})\rangle = w'\gamma_5^+(-\sin\theta_\mathbf{k}, \cos\theta_\mathbf{k}, 0), \tag{48}$$

with $\cos\theta_\mathbf{k} = k_x/k$, $\sin\theta_\mathbf{k} = k_y/k$, and the pseudospin

$$\langle\phi^+(\mathbf{k})|\vec{\hat{\sigma}}|\phi^+(\mathbf{k})\rangle = w'(-\sin\theta_\mathbf{k}, \cos\theta_\mathbf{k}, 0). \tag{49}$$

These equations show that w' dictates the sense of rotation of the SEV (i.e., the chirality) and of the pseudospin. Moreover, $|\phi^+(\mathbf{k})\rangle$ is such that

$$M_y|\phi^+(|k_x|,0)\rangle = -iw'|\phi^+(|k_x|,0)\rangle, \tag{50}$$

$$M_{x-y}|\phi^+(k_x = k_y > 0)\rangle = -iw'|\phi^+(k_x = k_y > 0)\rangle, \tag{51}$$

$$M_x|\phi^+(0,|k_y|)\rangle = +iw'|\phi^+(0,|k_y|)\rangle, \tag{52}$$

which, when comparing to Eqs. (13)–(15), shows that w' from Eq. (44) is actually equal to $w \equiv \operatorname{sgn}(\mathcal{C}_{k_z=0}^+\mathcal{C}_{k_z=\pi}^+)$ from Eq. (12): as a consequence, in what follows, we will simply put $w' = w$; we also obtain $v \equiv \operatorname{sgn}(\mathcal{C}_{k_z=0}^+\mathcal{C}_{k_x=k_y}^+) = -1$ from Eqs. (11), (14), and (51).

As noticed in Ref. [36], due to time-reversal and C_{4v} symmetry (the surface symmetry group must contain a rotation by π along an axis perpendicular to the surface), the SEV along z on this surface is always zero, even beyond the small-momentum expansion.

Equations (38), (42), and (44) represent the most important results of this section. They show that the $\bar{\Gamma}$ cone only exists in subspace 1, and its chirality w depends on the relative sign of the hybridization term in H_0 through f_1^v (27) and in H_P through h_1^v (30). This is in agreement with the results of Ref. [22].

We remark that for the model used in Refs. [3,37] the kinetic energy is such that $\epsilon_1^d > \epsilon_1^f$, $\epsilon_2^d < \epsilon_2^f$. As a result, the minimum in the conduction band at X has d_{z^2} character (X_6^+ symmetry representation instead of X_7^+) and surface states near $\bar{\Gamma}$ only exist in subspace 2, with basis d_{z^2} and $\Gamma_8^{(2)}$. As noted in Ref. [21], this leads to $v = +1$ (instead of $v = -1$). Moreover, with the same procedure as above, we can show that in this case the chirality $w = \operatorname{sgn}(f_2^v h_2^v)$, with f_2^v from Eq. (28) and h_2^v from Eq. (31); this shows that hybridization parameters η_z^{v1} and η_z^{v2}, if dominant, lead to $w = -1$, while dominant η_x^{v2} to $w = +1$ [21]. Most of our equations are formally equivalent to those in Ref. [37], once a proper replacement of quantities from subspace 1 to subspace 2 is performed, while the final results for spin structures are different due to the different expressions for w.

B. E_g-Γ_7 basis

We repeat the calculation, now retaining the Γ_7 doublet together with the E_g quartet, i.e., neglecting rows and columns from 5 to 8 in Eq. (23). Along Γ-X the Γ_7 doublet can only hybridize with $d_{x^2-y^2}$, that we therefore assume to be inverted, and we only consider subspace $1'$ from Sec. III B [see Eq. (34)]. (Note that in the opposite case, with the inversion in d_{z^2}, no

insulator would be obtained.) We can repeat the same steps of the previous subsection with the substitutions

$$\epsilon_1^f \to \epsilon_7^f > \epsilon_1^d, \quad g_1^f \to g_7^f < 0, \quad l_1^f \to l_7^f < 0,$$
$$f_1^v \to f_7^v, \quad h_1^v \to h_7^v, \tag{53}$$

so we obtain the effective surface Hamiltonian (42) with $w = \mathrm{sgn}(f_7^v h_7^v)$ and the basis

$$|\psi_+\rangle = \alpha|d^1\uparrow\rangle + \beta|f^7+\rangle,$$
$$|\psi_-\rangle = \alpha|d^1\downarrow\rangle - \beta|f^7-\rangle. \tag{54}$$

For the pseudospin expectation value, we obtain the same results as in the previous section, Eqs. (47) and (49); the SEV in the basis (54) is

$$2\langle\vec{\hat{S}}\rangle = \left(\gamma_5^-\hat{s}_x, \gamma_5^-\hat{s}_y, \gamma_5^+\hat{s}_z\right), \tag{55}$$

and the wave function $|\phi^+(\mathbf{k})\rangle$ has the SEV

$$2\langle\phi^+(\mathbf{k})|\vec{\hat{S}}|\phi^+(\mathbf{k})\rangle = w\gamma_5^-(-\sin\theta_\mathbf{k}, \cos\theta_\mathbf{k}, 0), \tag{56}$$

which is reversed with respect to the case with the Γ_8 quadruplet since $\gamma_5^- < 0$. This is a consequence of the fact that, for Γ_8 states, SEV and pseudospin are parallel, while for Γ_7 states they are antiparallel [22]. We also notice that $|\phi^+(\mathbf{k})\rangle$ has the same mirror-symmetry eigenvalues as before [Eqs. (50)–(52)], so, given the same MCNs, Γ_7 states give an opposite SEV pattern with respect to Γ_8 states [21]. This is due to the fact that, strictly speaking, MCNs denote the sense of rotation of the pseudospin on surface states [22], while relations for the SEV can be in general more complicated [21,22].

C. E_g-Γ_7-Γ_8 basis

The two different choices of the previous subsections correspond to large values of the crystal-field splitting, such as we can ignore either Γ_7 or Γ_8 states. If we have to take into account both Γ_7 and Γ_8 multiplets, the $\bar{\Gamma}$ cone is composed by $d_{x^2-y^2}$, $\Gamma_8^{(1)}$, and Γ_7 states, Hamiltonian $H_0^{+(1)}$ (37) becomes a 3×3 matrix, and no analytic solution can be found anymore. However, when $k_z = 0$, i.e., exactly at X, we can diagonalize the f block

$$H_0^{1,7} = \begin{pmatrix}\epsilon_1^f & m_{78}\\ m_{78} & \epsilon_7^f\end{pmatrix} = \frac{\epsilon_1^f+\epsilon_7^f}{2} + \begin{pmatrix}-\frac{\Delta}{2} & m_{78}\\ m_{78} & \frac{\Delta}{2}\end{pmatrix}, \tag{57}$$

with $\Delta = \epsilon_7^f - \epsilon_1^f$, out of which we pick the state which is mostly responsible for the band inversion, i.e., the one of higher energy, which is (we do the same for $H_0^{-(1)}$)

$$\left|f_p^{17}\pm\right\rangle = \beta_1|f^1\pm\rangle + \beta_7|f^7\pm\rangle, \tag{58}$$

$$\mathrm{sgn}(\beta_1\beta_7) = \mathrm{sgn}(m_{78}), \quad \beta_1^2+\beta_7^2 = 1. \tag{59}$$

Keeping only $|d^1\uparrow\rangle$ and $|f_p^{17}+\rangle$ states, we now get

$$H_0^{+(1)} = \begin{pmatrix}\epsilon_1^d - t_d k_z^2 g_1^d & -iVk_z f_{17}^v\\ -iVk_z f_{17}^v & \epsilon_+^f - t_f k_z^2 g_{17}^f\end{pmatrix}, \tag{60}$$

which is Eq. (37) with the substitutions $f_1^v \to \beta_1 f_1^v + \beta_7 f_7^v \equiv f_{17}^v$, $g_1^f \to \beta_1^2 g_1^f + \beta_7^2 g_7^f \equiv g_{17}^f < 0$. With this approach we neglect the other linear combination of $|f^1\rangle$ and $|f^7\rangle$ states, called $|f_m^{17}\rangle$ in Fig. 2(c), which at X remains below the Fermi energy.

With this approximation, whose validity we will assess in Sec. VII, the problem is now solvable by hand. We get the doublet in the form

$$|\psi_+\rangle = \alpha|d^1\uparrow\rangle + \beta\beta_1|f^1+\rangle + \beta\beta_7|f^7+\rangle,$$
$$|\psi_-\rangle = \alpha|d^1\downarrow\rangle - \beta\beta_1|f^1-\rangle - \beta\beta_7|f^7-\rangle, \tag{61}$$

with $\mathrm{sgn}(\alpha\beta) = -\mathrm{sgn}(Vf_{17}^v)$. When we project the perturbing Hamiltonian, which is now a 6×6 matrix, we get Eq. (42) with the substitution $h_1^v \to \beta_1 h_1^v + \beta_7 h_7^v \equiv h_{17}^v$. The chirality w, as a consequence, is now given by

$$w = \mathrm{sgn}\left[f_{17}^v h_{17}^v\right]$$
$$= \mathrm{sgn}\left[\left(\beta_1 f_1^v + \beta_7 f_7^v\right)\left(\beta_1 h_1^v + \beta_7 h_7^v\right)\right]. \tag{62}$$

This approach is equivalent to starting from Eq. (35) with the given expressions of f_{17}^v and g_{17}^v, and $\epsilon_{17}^f(\mathbf{k}) = \epsilon_+^f - t_f(k_z^2 g_{17}^f + k_\parallel^2 l_{17}^f), l_{17}^f = \beta_1^2 l_1^f + \beta_7^2 l_7^f$.

Relations for the pseudospin, Eqs. (47) and (49), remain invariant, with a redefinition of w according to Eq. (62). For spin operators we find

$$2\langle\vec{\hat{S}}\rangle = (\gamma_5^{+'}\hat{s}_x, \gamma_5^{+'}\hat{s}_y, \gamma_{11}^{-'}\hat{s}_z), \tag{63}$$

$$\gamma_5^{\pm'} = \alpha^2 \pm \frac{5}{21}\beta^2\beta_1^2 \mp \frac{5}{21}\beta^2\beta_7^2 \mp \frac{4\sqrt{5}}{21}\beta^2\beta_1\beta_7, \tag{64}$$

$$\gamma_{11}^{\pm'} = \alpha^2 \pm \frac{11}{21}\beta^2\beta_1^2 \mp \frac{5}{21}\beta^2\beta_7^2 \pm \frac{8\sqrt{5}}{21}\beta^2\beta_1\beta_7, \tag{65}$$

and for the SEV on the state of positive energy

$$2\langle\phi^+(\mathbf{k})|\vec{\hat{S}}|\phi^+(\mathbf{k})\rangle = w\gamma_5^{+'}(-\sin\theta_\mathbf{k}, \cos\theta_\mathbf{k}, 0). \tag{66}$$

While the pseudospin is the same as before, the SEV, on the other hand, can be parallel or antiparallel to the pseudospin according to the sign of $\gamma_5^{+'}$, which depends on the relative weights β_1 and β_7. We also note that the sign of the interference term in Eq. (64) depends on the relative sign of β_1 and β_7, which is the sign of m_{78} [see Eq. (59)]. *Ab initio* calculations indicate $m_{78} > 0$ for SmB_6 [see Eq. (26)], favoring antiparallel spin and pseudospin.

V. EXPANSION AROUND $\bar{X}$ FOR (001) SURFACE

Here, we employ the same technique as in the previous section, but for the effective Hamiltonian at the surface momenta $\bar{X}, \bar{X}'$ on the (001) surface.

A. E_g-Γ_8 basis

One route to obtain surface states around $\bar{X}$ is to project $X' = (\pi,0,0)$ onto the (001) surface [37]. In this case, $H_0^{+(1)}$ is a 4×4 matrix which does not admit a simple analytical solution. An alternative route is to project $X = (0,0,\pi)$ onto the (100) surface: In this case, k_y and k_z remain good quantum numbers, and we obtain surface states near $k_y = 0$, $k_z = \pi$. To get the effective Hamiltonian for the (001) surface, we then must perform a rotation of the coordinate system.

We will follow this second route, even if apparently more involved, as it allows for a good approximation which makes the problem solvable by hand. Upon retaining the Γ_8 quadruplet, the Hamiltonian H_0^+, obtained by setting $k_y = k_z = 0$, has now as a basis $|d^1\uparrow\rangle, |d^2\uparrow\rangle, |f^1-\rangle, |f^2-\rangle$, but does not decouple any more into two 2×2 blocks, due to the terms in h_{12}^v and h_{21}^v. However, we may adopt the approximation to neglect these couplings between subspaces 1 and 2, such that $|\psi_+\rangle$ and $|\psi_-\rangle$ live entirely into subspace 1, which is reasonable since it is where band inversion is achieved:

$$|\psi_+\rangle \simeq \alpha|d^1\uparrow\rangle + \beta|f^1-\rangle,$$
$$|\psi_-\rangle \simeq \alpha|d^1\downarrow\rangle + \beta|f^1+\rangle. \quad (67)$$

This is found to be an excellent approximation when compared to the tight-binding results in the limit of small momenta: the weight of states in subspace 2 rarely exceeds a few percent. We remark that such a simplification can be achieved only with our choice of projecting $X = (0,0,\pi)$ onto the (100) surface. As shown below, the weight of states in subspace 2 on the (001) surface is 75%, i.e., projecting $X' = (\pi,0,0)$ onto the (001) surface does not admit any obvious approximation.

Neglecting the couplings between subspaces 1 and 2, H_0^+ in the basis $|d^1\uparrow\rangle, |f^1-\rangle$ reads as

$$H_0^+ = \begin{pmatrix} \epsilon_1^d - t_d k_x^2 l_1^d & -iVk_x h_1^v \\ iVk_x h_1^v & \epsilon_1^f - t_f k_x^2 l_1^f \end{pmatrix}, \quad (68)$$

which corresponds to Eq. (37) with the substitution $g_1^d \to l_1^d, g_1^f \to l_1^f, k_z \to k_x, f_1^v \to h_1^v$. We can take coefficients α and β as real, with $\mathrm{sgn}(\alpha\beta) = -\mathrm{sgn}(Vh_1^v)$ from Eq. (40), as a calculation similar to the one of the previous section shows, and which also leads to the effective Hamiltonian for small momenta.

We have, however, to go back to the (001) surface through a coordinate rotation $k_x \to k_z \to k_y \to k_x$, which changes d and f states according to Wigner U matrices [3,31], and a basis rotation $\hat{s}_x \to \hat{s}_z \to \hat{s}_y \to \hat{s}_x$, to get the effective Hamiltonian around $\bar{X}'$:

$$H_{\bar{X}'}^{\mathrm{eff}} = -|v_1| w k_y \hat{s}_x + |v_2| k_x \hat{s}_y, \quad (69)$$

with basis

$$|\psi'_+\rangle = \frac{\alpha}{2}(|d^1\uparrow\rangle - \sqrt{3}|d^2\uparrow\rangle) + \frac{\beta}{2}(|f_1+\rangle - \sqrt{3}|f_2+\rangle),$$
$$|\psi'_-\rangle = \frac{\alpha}{2}(|d^1\downarrow\rangle - \sqrt{3}|d^2\downarrow\rangle) - \frac{\beta}{2}(|f_1-\rangle - \sqrt{3}|f_2-\rangle), \quad (70)$$

and velocities

$$v_1 = -2\alpha\beta V f_1^v = 2w\left|Vf_1^v\right| \frac{\sqrt{-t_d t_f l_1^d l_1^f}}{t_f l_1^f - t_d l_1^d}, \quad (71)$$

$$v_2 = -2\alpha\beta V h_1^v = 2\left|Vh_1^v\right| \frac{\sqrt{-t_d t_f l_1^d l_1^f}}{t_f l_1^f - t_d l_1^d} > 0. \quad (72)$$

It can be observed that the relative sign of the two Dirac velocities, that is the winding number of the $\bar{X}$ cone, is given by $\mathrm{sgn}(v_1 v_2) = w = \mathrm{sgn}(f_1^v h_1^v)$, that is, the same expression which gives the chirality of the $\bar{\Gamma}$ cone. Thus, we recover, through a different derivation, the results of Ref. [22].

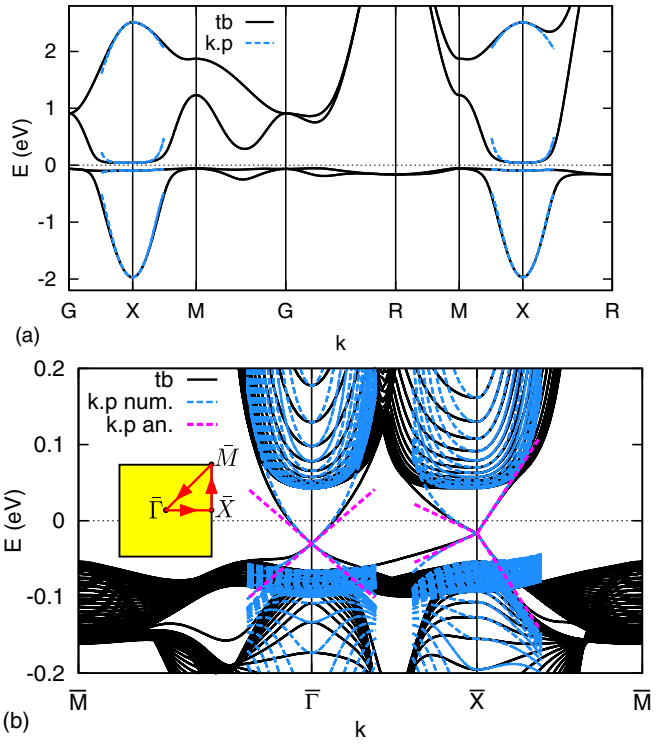

FIG. 3. (a) Bulk tight-binding band structure for parameters $t_c = 0.8\,\mathrm{eV}, t_f = -0.002\,\mathrm{eV}, V = 0.063\,\mathrm{eV}, \eta_z^{d1} = \eta_z^{f1} = 0.8, \eta_z^{d2} = -0.3, \eta_z^{f2} = -0.45, \epsilon_d - \epsilon_8 = 1.45$ eV, $\eta_z^{v1} = -2.1, \eta_z^{v2} = 0.6$. Also shown is the result of the $\mathbf{k}\cdot\mathbf{p}$ approximation around X [see Fig. 2(a)]. (b) Tight-binding band structure for a (001) slab of 30 layers, together with the analytical $\mathbf{k}\cdot\mathbf{p}$ approximation of surface states described in the text, and the numerical solution of the $\mathbf{k}\cdot\mathbf{p}$ model including bulk states (see Appendix E). We see that both $\mathbf{k}\cdot\mathbf{p}$ solutions give Dirac energies and velocities in excellent agreement with the tight-binding solution; obtaining accurate velocities requires to take into account third-order terms in $\mathbf{k}$ for the hybridization (see Appendix D).

In Fig. 3, we present a comparison between the analytical $\mathbf{k}\cdot\mathbf{p}$ result and the numerical tight-binding solution. We note that obtaining the exact value of the velocities v_0, v_1, v_2 requires to take into account higher-order terms in the small-momentum expansion (see Appendix D); for our choice of the parameters, it is enough to take the hybridization up to third order in $\mathbf{k}$.

We also remark that the reported dispersion of surface states does not fully agree with photoemission results, in that the Dirac energies are here inside the bulk gap, while experimentally they appear to be in the valence band [9–14]. One plausible explanation is the so-called "Kondo-breakdown" scenario in which f electrons on the surface are no more Kondo screened, yielding surface states with larger velocity [38]. In an effective single-particle description, Kondo breakdown is equivalent to an infinite f-electron scattering potential at the surface [39] which, however, does no longer allow for an analytical treatment within the $\mathbf{k}\cdot\mathbf{p}$ approach. Importantly, a comparison of numerical results with and without this

scattering potential indicates that the spin pattern of surface states is robust to this perturbation.

Spin and pseudospin operators become

$$2\langle\vec{\hat{S}}\rangle = (\gamma_5^+\hat{s}_x,\gamma_{11}^+\hat{s}_y,\gamma_5^-\hat{s}_z), \tag{73}$$

$$\langle\vec{\hat{\sigma}}\rangle = (\hat{s}_x,\hat{s}_y,\gamma^-\hat{s}_z), \tag{74}$$

which shows that operators $\hat{s}_x$ and $\hat{s}_y$ in Eq. (69) can be substituted exactly by pseudospin operators $\hat{\sigma}_x$ and $\hat{\sigma}_y$, or, up to a constant factor, by spin operators $\hat{S}_x$ and $\hat{S}_y$, once again justifying writing the effective Hamiltonian in terms of spin operators [21]. For the state $|\phi^+_{\bar{X}'}(\mathbf{k})\rangle$ with positive energy $\epsilon_{\mathbf{k}} = \sqrt{v_1^2k_y^2 + v_2k_x^2}$ at a given momentum $\mathbf{k}$ for Eq. (69) the SEV and pseudospin are

$$2\langle\phi^+_{\bar{X}'}(\mathbf{k})|\vec{\hat{S}}|\phi^+_{\bar{X}'}(\mathbf{k})\rangle = (-\gamma_5^+ w\sin\theta_{\mathbf{k}},\gamma_{11}^+\cos\theta_{\mathbf{k}},0), \tag{75}$$

$$\langle\phi^+_{\bar{X}'}(\mathbf{k})|\vec{\hat{\sigma}}|\phi^+_{\bar{X}'}(\mathbf{k})\rangle = (-w\sin\theta_{\mathbf{k}},\cos\theta_{\mathbf{k}},0), \tag{76}$$

with $\cos\theta_{\mathbf{k}} = |v_2|k_x/\epsilon_{\mathbf{k}}$, $\sin\theta_{\mathbf{k}} = |v_1|k_y/\epsilon_{\mathbf{k}}$. Moreover, we find

$$M_y|\phi^+_{\bar{X}'}(|k_x|,0)\rangle = -i|\phi^+_{\bar{X}'}(|k_x|,0)\rangle, \tag{77}$$

$$M_x|\phi^+_{\bar{X}'}(0,-|k_y|)\rangle = -iw|\phi^+_{\bar{X}'}(0,-|k_y|)\rangle, \tag{78}$$

which agrees with Eqs. (18) and (19), confirming that $w = \mathrm{sgn}(f_1^v h_1^v) = \mathrm{sgn}(\mathcal{C}^+_{k_z=0}\mathcal{C}^+_{k_z=\pi})$.

After a $\pi/2$ rotation we also obtain the effective Hamiltonian around $\bar{X}$:

$$H^{\mathrm{eff}}_{\bar{X}} = |v_1|wk_x\hat{s}_y - |v_2|k_y\hat{s}_x, \tag{79}$$

and similar expressions hold for the SEV and the pseudospin:

$$2\langle\phi^+_{\bar{X}}(\mathbf{k})|\vec{\hat{S}}|\phi^+_{\bar{X}}(\mathbf{k})\rangle = (-\gamma_{11}^+\sin\theta_{\mathbf{k}},\gamma_5^+ w\cos\theta_{\mathbf{k}},0), \tag{80}$$

$$\langle\phi^+_{\bar{X}}(\mathbf{k})|\vec{\hat{\sigma}}|\phi^+_{\bar{X}}(\mathbf{k})\rangle = (-\sin\theta_{\mathbf{k}},w\cos\theta_{\mathbf{k}},0), \tag{81}$$

where now $\cos\theta_{\mathbf{k}} = |v_1|k_x/\epsilon_{\mathbf{k}}$ and $\sin\theta_{\mathbf{k}} = |v_2|k_y/\epsilon_{\mathbf{k}}$. Moreover, Eqs. (16) and (17) hold.

Equations (69), (70), and (79) are the most important results of this section: they show that Dirac cones at $\bar{X}$ and $\bar{X}'$ have two different velocities, whose relative sign is given by Eq. (44), that is, the same expression which gives the chirality of the $\bar{\Gamma}$ cone. Equation (70) implies that in our approximation, the Dirac cones at $\bar{X},\bar{X}'$ are composed from 75% of $\Gamma_8^{(2)}$ and d_{z^2} states and from 25% of $\Gamma_8^{(1)}$ and $d_{x^2-y^2}$ states. This is in good agreement with tight-binding results, which for typical values of the parameters shows these percentages to be $\gtrsim 70\%$ and $\lesssim 30\%$. We recall that, for the present reduced basis, the $\bar{\Gamma}$ cone is entirely composed by $\Gamma_8^{(1)}$ and $d_{x^2-y^2}$ states.

B. E_g-Γ_7 basis

When using the Γ_7 doublet instead of Γ_8 quadruplet, the basis for H_0^+ is spanned by $|d^1\uparrow\rangle, |d^2\uparrow\rangle, |f^7-\rangle$; with the same approximation of the previous subsection we can neglect term h_{72}^v in Eq. (23), hence, $|d^2\uparrow\rangle$. The basis for surface states at $k_y = 0, k_z = \pi$ on the (100) surface becomes

$$|\psi_+\rangle = \alpha|d^1\uparrow\rangle + \beta|f^7-\rangle,$$
$$|\psi_-\rangle = \alpha|d^1\downarrow\rangle + \beta|f^7+\rangle. \tag{82}$$

After rotation, the effective Hamiltonian is Eq. (69) with basis

$$|\psi'_+\rangle = \frac{\alpha}{2}(|d_1\uparrow\rangle - \sqrt{3}|d_2\uparrow\rangle) - \beta|f_7+\rangle,$$
$$|\psi'_-\rangle = \frac{\alpha}{2}(|d_1\downarrow\rangle - \sqrt{3}|d_2\downarrow\rangle) + \beta|f_7-\rangle, \tag{83}$$

and the usual substitutions $f_1^v, h_1^v, l_1^{d,f} \to f_7^v, h_7^v, l_7^{d,f}$; the winding number has the same expression of the chirality at $\bar{\Gamma}$: $w = \mathrm{sgn}(f_7^v h_7^v)$.

The pseudospin behaves as in the previous section, Eqs. (74) and (76). Spin operators are

$$2\langle\vec{S}\rangle = (\gamma_5^-\hat{s}_x,\gamma_5^-\hat{s}_y,\gamma_5^+\hat{s}_z), \tag{84}$$

and the SEV on the state with positive energy is

$$2\langle\phi^+_{\bar{X}'}(\mathbf{k})|\vec{\hat{S}}|\phi^+_{\bar{X}'}(\mathbf{k})\rangle = \gamma_5^-(-w\sin\theta_{\mathbf{k}},\cos\theta_{\mathbf{k}},0), \tag{85}$$

which is antiparallel with respect to the Γ_8 case since $\gamma_5^- < 0$.

We see that when performing the rotation to go back to the (001) surface, Γ_7 goes into itself [Eq. (83)], so now surface states at $\bar{X}$ are mostly Γ_7 in character, just like surface states at $\bar{\Gamma}$. In this case, when projecting along the x direction, the approximation of neglecting subspace 2 is always reliable since here we are only discarding a d state (d_{z^2}), which contributes a small weight to surface states; this is confirmed by tight-binding results.

C. E_g-Γ_7-Γ_8 basis

With the choice of the basis

$$|\psi_+\rangle = \alpha|d^1\uparrow\rangle + \beta\beta_1|f^1-\rangle + \beta\beta_7|f^7-\rangle,$$
$$|\psi_-\rangle = \alpha|d^1\downarrow\rangle + \beta\beta_1|f^1+\rangle + \beta\beta_7|f^7+\rangle, \tag{86}$$

we obtain the same Hamiltonian at $\bar{X}'$ [Eq. (69)], with the new definition of the winding number [Eq. (62)]. The relations for the pseudospin (74) and (76) remain invariant. For the spin we find

$$2\langle\vec{\hat{S}}\rangle = (\gamma_5^{+'}\hat{s}_x,\gamma_{11}^{+'}\hat{s}_y,\gamma_5^{-'}\hat{s}_z), \tag{87}$$

and for the SEV on the state of positive energy

$$2\langle\phi^+(\mathbf{k})|\vec{\hat{S}}|\phi^+(\mathbf{k})\rangle = (-w\gamma_5^{+'}\sin\theta_{\mathbf{k}},\gamma_{11}^{+'}\cos\theta_{\mathbf{k}},0). \tag{88}$$

Similar relations hold at $\bar{X}$.

We note that terms $\gamma_5^{+'}$ and $\gamma_{11}^{+'}$ [Eqs. (64) and (65)] can be positive or negative according to the relative weight of β_1 and β_7 in $|f_p^{17}\pm\rangle$. Even if unlikely, it may also happen that, when $|\beta_1| \sim |\beta_7|$, they carry different signs; in this case the winding number of the SEV would be different from the winding number of the pseudospin, with only the latter directly related to the topological phase. In Ref. [21] we assumed this scenario not to occur, which should be a safe assumption for most of parameter space.

D. Comparison with DFT and experiments

We now relate our model-dependent analysis to concrete results for SmB_6 found in the literature. As we have shown, the winding number $w \equiv \mathrm{sgn}(\mathcal{C}^+_{k_z=0}\mathcal{C}^+_{k_z=\pi})$ depends on the retained f multiplet (Γ_7 or Γ_8), the symmetry of the inverted subspace ($d_{x^2-y^2}$ subspace-1-symmetry representation X_7^+, or d_{z^2} subspace-2-symmetry representation X_6^+), and the hybridization. Based on DFT results [29–31], we can safely state that the band inversion happens in subspace 1, which is spanned by $d_{x^2-y^2}$, $\Gamma_8^{(1)}$, and Γ_7. This leads to $v \equiv \mathrm{sgn}(\mathcal{C}^+_{k_z=0}\mathcal{C}^+_{k_x=k_y}) = -1$, and, when we take into account the Γ_8 quadruplet only, to $w = \mathrm{sgn}(f_1^v h_1^v)$; as a consequence, η_z^{v2} leads to $w = +1$, while η_x^{v1} and η_x^{v2} to $w = -1$ [see Eqs. (27) and (30)]. *Ab initio* calculations [30,31] show the largest hybridization term to be η_z^{v1}, which, however, does not lead alone to a gap by symmetry mismatch (actually, it does not appear in f_1^v); the second most important term is η_z^{v2}, hence, $w = +1$; numerical solutions by keeping many hybridization terms show $w = +1$ to remain the correct solution. When we use the Γ_7 doublet, instead, $w = \mathrm{sgn}(f_7^v h_7^v)$, which gives $w = +1$ for η_7^{v1} and $\eta_{x^2}^{v2}$, and $w = -1$ for η_7^{v2} [see Eqs. (29) and (32)], which is the largest term in *ab initio* calculations, leading to $w = -1$ even when keeping more hybridization terms. Hence, retaining different multiplets leads to different values of w, and to different topological phases.

Spin-resolved photoemission data [14] indicate a winding number $w = +1$ on the $\bar{X}$ cone, leading to a preference toward our Γ_8 model; this is in agreement with Ref. [40], which finds surface states to be mostly Γ_8. While early theory papers [1–3] have not discussed the Dirac-cone spin structure, it was shown in Refs. [21,22] that a full characterization of the SmB_6 electronic structure requires the knowledge of the exact value of MCNs, which directly influence the spin structure of surface states. In a few *ab initio* calculations, the spin structure is addressed: in Ref. [36] it seems to contradict experimental results, rather suggesting $w = -1$; while the one of Ref. [35] agrees with experiments, as well as the one of Ref. [31], which is, however, based on PuB_6 *ab initio* calculations [30]. We thus believe that the question deserves further consideration; from our point of view it reduces to understanding if Γ_7 ($w = -1$) or Γ_8 ($w = +1$) states are mostly responsible for the bulk gap and the composition of surface states; in Sec. VII, we show that varying their relative energy leads to a topological phase transition $w = -1 \leftrightarrow +1$ between these two possibilities, where the latter one should be realized in "clean" SmB_6.

VI. GENERIC FLAT SURFACE

So far, we have studied surface states on the (001) surface, well studied already in previous papers. The power of the $\mathbf{k}\cdot\mathbf{p}$ approach is, however, that we can obtain analytical results also for a generic flat (lmn) surface without much additional effort. Here, we will in particular consider (110), (111), and (210) surfaces. We note that, by construction, the $\mathbf{k}\cdot\mathbf{p}$ approach only yields results for surface Dirac cones protected by parity invariants because those arise from bands near time-reversal-invariant momenta. In contrast, Dirac cones only protected by mirror symmetries are not accessible; this will be relevant for the (110) surface of SmB_6.

In the following, we denote surface momenta as $\bar{k}_x$ and $\bar{k}_y$ to distinguish them from bulk momenta, a distinction which on the (001) surface is not needed since there $\bar{k}_x = k_x$, $\bar{k}_y = k_y$.

A. Surface states from parity invariants and mirror Chern numbers

Since there are three bulk X points with band inversion, parity invariants predict in general three Dirac ones in the 2D BZ. Mirror symmetries might complicate the situation, and we discuss a number of surfaces explicitly.

On the (110) surface, one X point is projected onto the $\bar{X} = (\pi,0)$ point of the rectangular surface BZ, while the other two onto $\bar{Y} = (0,\pi/\sqrt{2})$, which will then hybridize and gap out: as a consequence, only a single Dirac cone is predicted by parity invariants at $\bar{X}$. As shown in Ref. [19], MCNs predict the presence of two additional Dirac cones along the $\bar{\Gamma}$-$\bar{Y}$ direction. Indeed, the $k_z = 0$ plane is projected to $\bar{k}_x = 0$, while $k_z = \pi$ to $\bar{k}_x = \pi$, and $k_x = k_y$ to $\bar{k}_y = 0$ [see Fig. 1(c)]. We must therefore have a Dirac cone along $\bar{X}$-$\bar{S}$ and $\bar{X}$-$\bar{\Gamma}$, which is simply the cone at $\bar{X}$ predicted by parity invariants, and two new cones along $\bar{\Gamma}$-$\bar{Y}$ as a consequence of $\mathcal{C}^+_{k_x=k_y} = \pm 2$; these cones are protected by mirror symmetry only. In addition to this, we can characterize the $\bar{X}$ cone with a winding number; its SEV is fixed along the $\bar{X}$-$\bar{S}$ direction by $\mathcal{C}^+_{k_z=\pi} = +1$, but it changes along the $\bar{X}$-$\bar{\Gamma}$ direction according to $\mathcal{C}^+_{k_x=k_y}$ and $\mathcal{C}^+_{k_z=\pi}$; while the first one fixes mirror eigenvalues, the second one tells what the SEV for a given mirror eigenvalue is. As a result, the winding number of the $\bar{X}$ cone is w, the same as on the (001) surface. This is shown in Fig. 5. We note, however, that the winding number on the $\bar{X}$ cone of the (110) surface is only fixed at low energies [21], when we can neglect subspace 2; at higher energies the spin direction along $\bar{k}_y = 0$ can thus in principle be reversed, and so the winding number. This is different from the (001) surface where the winding number is constrained by the symmetry operation M_z.

On the (210) surface, the situation is different: one X point is projected onto the $\bar{X} = (\pi,0)$ point of the rectangular surface BZ, as for the (110) surface; however, the other two X points are projected to $\bar{\Gamma} = (0,0)$ and $\bar{Y} = (0,\pi/\sqrt{5})$. Hence, parity invariants predict three Dirac cones, with no additional cones protected by mirror symmetry only. Since no Dirac cone is crossed by two mirror planes [see Fig. 1(e)], we cannot make any general predictions on the winding number.

On the (111) surface, the three bulk X points are projected to the three inequivalent $\bar{M}$ points of the hexagonal surface BZ. Mirror planes $k_x = k_y, k_y = k_z, k_z = k_x$ are projected along the three $\bar{\Gamma}$-$\bar{M}$ directions, fixing mirror-symmetry eigenvalues of Dirac cones along those lines; the only information we get is that the SEV is antiparallel at the two extrema of each cone, and nothing can be said about winding numbers using mirror eigenvalues only. These results are shown in Fig. 6.

We finally stress that for all the surfaces, the qualitative spin structure along high-symmetry directions only depends on w as one can realize by comparing in each of the Figs. 4, 5, 6, the pairs of panels (a) and (c) and (b) and (d), which share the same w, differ by v, and still have the same SEV. The number v, on the other hand, dictates the orbital composition

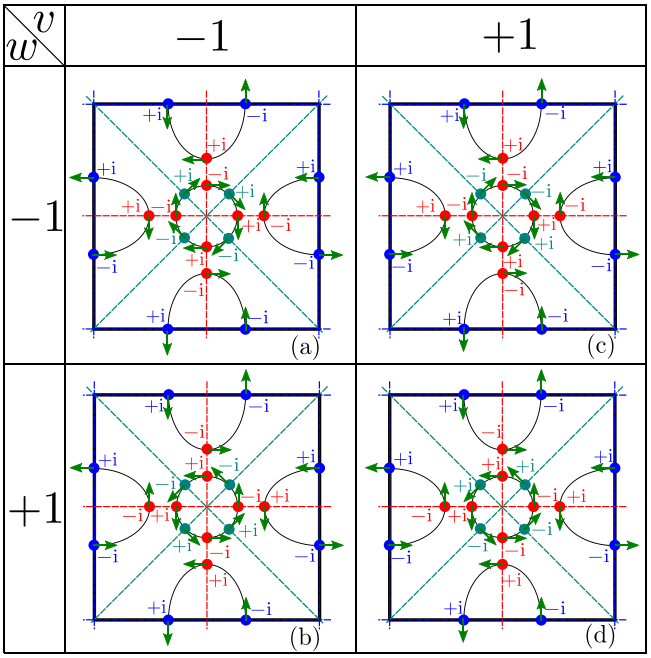

FIG. 4. Mirror planes as in Fig. 1 together with mirror-symmetry eigenvalues and SEV (green arrows) on the surface BZ for a (001) surface, as a function of $v \equiv \mathrm{sgn}(\mathcal{C}^+_{k_z=0}\mathcal{C}^+_{k_x=k_y})$ and $w \equiv \mathrm{sgn}(\mathcal{C}^+_{k_z=0}\mathcal{C}^+_{k_z=\pi})$. The panels correspond to MCNs $(\mathcal{C}^+_{k_z=0},\mathcal{C}^+_{k_z=\pi},\mathcal{C}^+_{k_x=k_y})$ as follows: (a) $(-2,+1,+1)$, (b) $(+2,+1,-1)$, (c) $(-2,+1,-1)$, (d) $(+2,+1,+1)$. To draw the SEV we assume Γ_8 states; for Γ_7 states the SEV is reversed. From Ref. [21].

of the different cones, and does not give any information on the spin.

B. Geometrical considerations

We want to develop a general theory for the spin structure of a Dirac cone on a given surface, following what we did in Secs. IV and V.

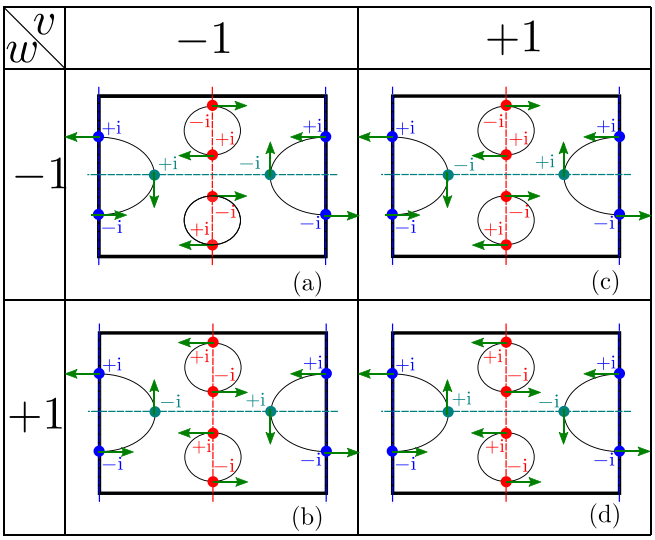

FIG. 5. Mirror planes, mirror-symmetry eigenvalues, and SEV on the BZ for a (110) surface for the same cases as in Fig. 4.

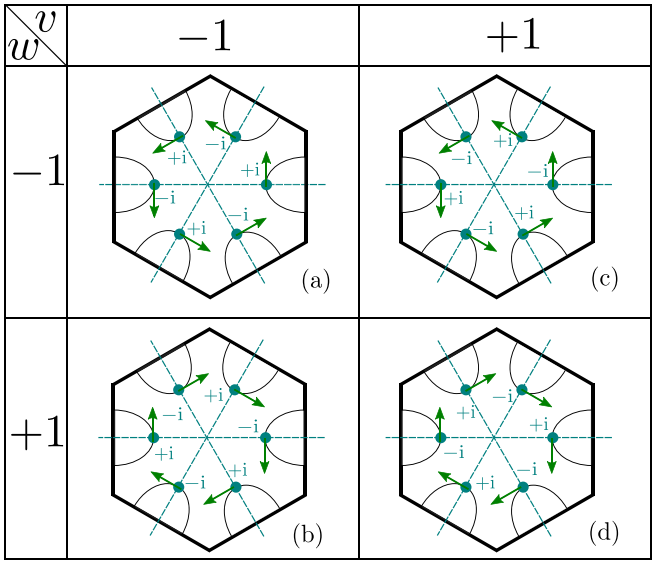

FIG. 6. Mirror planes, mirror-symmetry eigenvalues, and SEV on the BZ for a (111) surface for the same cases as in Fig. 4.

Given a generic (lmn) surface (without loss of generality, we will only consider non-negative l,m,n integers), the three indices are equivalent due to cubic symmetry. However, when we choose to expand around $X = (0,0,\pi)$, the resulting $\mathbf{k}\cdot\mathbf{p}$ Hamiltonian has tetragonal symmetry, with the z direction inequivalent to x and y. Consequently, the third index, which fixes the new z direction, is inequivalent to the first two: so we introduce the (lm/n) notation, to stress that index n is inequivalent from l and m. So, given (lmn), we have in general three inequivalent triplets $(lm/n) = (ml/n)$, $(mn/l) = (nm/l)$, and $(ln/m) = (nl/m)$ which correspond to the three possible choices for the z axis, or, alternatively, to the $\mathbf{k}\cdot\mathbf{p}$ expansion at each of the three different X points.

The (lm/n) triplet describes the direction along which $\bar{k}_z$ points, with polar angles

$$\theta \equiv \arctan\frac{\sqrt{l^2+m^2}}{n}, \tag{89}$$

$$\phi \equiv \arctan\frac{m}{l}, \tag{90}$$

and $\bar{k}_z \to -id/dz$, while $\bar{k}_x$ and $\bar{k}_y$ will remain good quantum number.

We can thus perform a rotation in momentum space with Euler angles $\omega,\omega' = \theta,\omega'' = \phi$ (we adopt the zyz convention), where ω, which is for the moment arbitrary, corresponds to a rotation in the $\bar{k}_x,\bar{k}_y$ plane; details are given in Appendix G. When $\omega = 0$ we find that the $X = (0,0,\pi)$ point is projected at

$$\bar{\mathbf{k}}_X = (-\pi\sin\theta, 0), \tag{91}$$

so $\bar{k}_x$ is the direction which joins $\bar{\Gamma}$ to the position of the cone, unless $\theta = 0$, which corresponds to the $\bar{\Gamma}$ cone on the (001) surface, for which $\bar{k}_x$ and $\bar{k}_y$ directions are equivalent. Also, to the X point we can assign the (lm/n) triplet, and an angle θ as defined in Eq. (89).

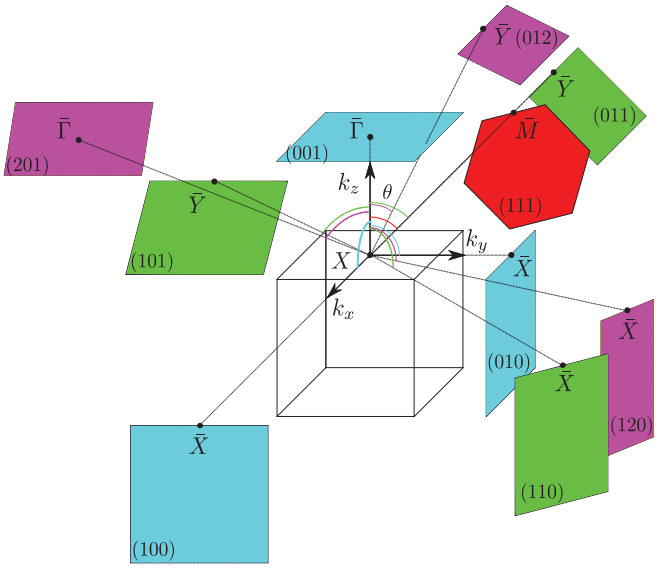

FIG. 7. The projection along different directions gives rise to different surface BZs, and the $X = (0,0,\pi)$ point is projected on different surface HSP. For a given (lmn) surface, we project the X point along the (lmn), (mnl), and (nlm) directions [we use the same color for each triplet (lmn)], giving rise to three surface Dirac cones. The only relevant parameter for each surface cone is the angle θ between k_z and the projection direction, which enters the expression for the winding number Eq. (113).

We can also find that $X' = (\pi,0,0)$ and $X'' = (0,\pi,0)$ are projected, respectively, to

$$\bar{\mathbf{k}}_{X'} = \pi(\cos\theta\cos\phi, -\sin\phi), \tag{92}$$

$$\bar{\mathbf{k}}_{X''} = \pi(\cos\theta\sin\phi, \cos\phi), \tag{93}$$

which are the positions of the two other Dirac cones in the 2D BZ when $\omega = 0$.

However, as argued in Sec. V, it is advantageous to always project X since this allows to safely neglect subspace 2. Hence, instead of considering three distinct X points and projecting them onto the same (lmn) surface, we follow the equivalent procedure of only considering the single $X = (0,0,\pi)$ point which we project onto the three (lmn),(mnl),(nlm) surfaces, as sketched in Fig. 7. Equations (89) and (90) continue to apply, but with a permutation of the indices l,m,n in such a way that, given a (lmn) surface, the triplets (lm/n),(mn/l),(nl/m) correspond each to one of the cones, with angles θ, θ', and θ'' (see also Appendix G). Specifically, on the (001) surface the $\bar{\Gamma}$ cone corresponds to the triplet (00/1) while the $\bar{X}$ and $\bar{X}'$ cones to (10/0) and (01/0), respectively. Similarly, the $\bar{X}$ cone on the (110) surface corresponds to (11/0), while (10/1) and (01/0) correspond to the two $\bar{Y}$ cones. Finally, on the (111) surface, all cones are equivalent. We stress that, in our approximation, all Dirac cones will live in subspace 1, but with a cone-dependent orbital quantization axis.

C. Results for a generic surface

In this section, we find the effective surface Hamiltonian for a given (lm/n) triplet; this Hamiltonian is valid for small momenta around the surface point $\bar{\mathbf{k}}_X$ on which the bulk $X = (0,0,\pi)$ point is projected; details are given in Appendix G. As before, we focus on subspace 1, so ignoring any coupling to subspace 2, and for the moment use only Γ_8 states.

We find that the effective Hamiltonian, up to the linear term in $\bar{\mathbf{k}}_\parallel$, is

$$\begin{aligned} H_\theta^{\text{eff}} &= v_1\bar{k}_x\hat{s}_y - v_2\bar{k}_y\hat{s}_x \\ &= |v_1|w\bar{k}_x\hat{s}_y - |v_2|\bar{k}_y\hat{s}_x, \end{aligned} \tag{94}$$

where v_1 and v_2 depend on θ:

$$v_1(\theta) = 2\left|Vh_1^v\right|\frac{f_1^v}{\bar{f}_1^v(\theta)}\frac{\sqrt{-t_d t_f \bar{g}_1^d(\theta)\bar{g}_1^f(\theta)}}{t_f\bar{g}_1^f(\theta) - t_d\bar{g}_1^d(\theta)}, \tag{95}$$

$$v_2(\theta) = 2\left|Vh_1^v\right|\frac{\sqrt{-t_d t_f \bar{g}_1^d(\theta)\bar{g}_1^f(\theta)}}{t_f\bar{g}_1^f(\theta) - t_d\bar{g}_1^d(\theta)} > 0, \tag{96}$$

with

$$\bar{g}_1^a(\theta) = g_1^a\cos^2\theta + l_1^a\sin^2\theta < 0, \quad a = d/f \tag{97}$$

$$\bar{f}_1^v(\theta) = \sqrt{\left(f_1^v\right)^2\cos^2\theta + \left(h_1^v\right)^2\sin^2\theta}\,\operatorname{sgn}\left(h_1^v\right). \tag{98}$$

Limiting cases are $|v_1(0)| = |v_2(0)| = |v_0|$ from Eq. (43), $v_1(\pi/2) = v_1$ from Eq. (71), and $v_2(\pi/2) = v_2$ from Eq. (72). Moreover, the center of the cone is at the energy

$$E(\theta) = \frac{\epsilon_1^f t_d\bar{g}_1^d(\theta) - \epsilon_1^d t_f\bar{g}_1^f(\theta)}{t_d\bar{g}_1^d(\theta) - t_f\bar{g}_1^f(\theta)}. \tag{99}$$

Equation (94) has the same form as Eq. (79) for the $\bar{X}$ cone on the (001) surface, but the basis is in general different, as well as the values of the velocities v_1, v_2. It also has formally the same spectrum $E_{\bar{\mathbf{k}}} = \pm\epsilon_{\bar{\mathbf{k}}} = \pm\sqrt{v_1^2\bar{k}_x^2 + v_2^2\bar{k}_y^2}$, which gives rise to elliptic isoenergy contours.

When we look at pseudospin operators, we discover that $\hat{s}_x$ is in general not simply proportional to $\hat{\sigma}_x$, but contains a $\hat{\sigma}_z$ component as well:

$$\langle\vec{\hat{\sigma}}\rangle = (A_\theta\hat{s}_x + B_\theta\gamma^-\hat{s}_z, \hat{s}_y, -B_\theta\hat{s}_x + A_\theta\gamma^-\hat{s}_z), \tag{100}$$

with

$$A_\theta = \frac{\left|h_1^v\right|\sin^2\theta + w\left|f_1^v\right|\cos^2\theta}{|\bar{f}_1^v|}, \tag{101}$$

$$B_\theta = \frac{\left|h_1^v\right| - w\left|f_1^v\right|}{\left|\bar{f}_1^v\right|}\sin\theta\cos\theta. \tag{102}$$

As a consequence, we find

$$\hat{s}_x = A_\theta\hat{\sigma}_x - B_\theta\hat{\sigma}_z, \quad \hat{s}_y = \hat{\sigma}_y \tag{103}$$

since $A_\theta^2 + B_\theta^2 = 1$. Inserting these expressions into Eq. (94) we obtain the Hamiltonian in terms of pseudospin operators

$$\begin{aligned} H_\theta^{\text{eff}} &= v_1\bar{k}_x\hat{\sigma}_y - v_2\bar{k}_y A_\theta\hat{\sigma}_x + v_2\bar{k}_y B_\theta\hat{\sigma}_z \qquad (104)\\ &= |v_1|w\bar{k}_x\hat{\sigma}_y - |v_2A_\theta|w\bar{w}_d(\theta)\bar{k}_y\hat{\sigma}_x + v_2B_\theta\bar{k}_y\hat{\sigma}_z \\ &\equiv |v_x|w\bar{k}_x\hat{\sigma}_y - |v_y|w\bar{w}_d(\theta)\bar{k}_y\hat{\sigma}_x + v_\perp\bar{k}_y\hat{\sigma}_z, \qquad (105) \end{aligned}$$

with $v_x = v_1$, $v_y = v_2 A_\theta$, $v_\perp = v_2 B_\theta$, and

$$\bar{w}_d(\theta) = \mathrm{sgn}\left(|f_1^v|\cos^2\theta + w|h_1^v|\sin^2\theta\right) = \mathrm{sgn}\left[|f_1^v|n^2 + w|h_1^v|(l^2+m^2)\right]. \quad (106)$$

Equivalently, this can be written as

$$H_\theta^{\mathrm{eff}} = \epsilon_{\bar{\mathbf{k}}}\left(n_{\bar{\mathbf{k}}}^x\hat{\sigma}_x + n_{\bar{\mathbf{k}}}^y\hat{\sigma}_y + n_{\bar{\mathbf{k}}}^z\hat{\sigma}_z\right) = \epsilon_{\bar{\mathbf{k}}}\vec{n}_{\bar{\mathbf{k}}}\cdot\vec{\hat{\sigma}}, \quad (107)$$

$$\vec{n}_{\bar{\mathbf{k}}} = (-v_y\bar{k}_y, v_x\bar{k}_x, v_\perp\bar{k}_y)/\epsilon_{\bar{\mathbf{k}}}, \quad (108)$$

with $\vec{n}_{\bar{\mathbf{k}}}$ a unit vector; this is Eq. (1) quoted in the Introduction. Hence, surface states are eigenstates of the pseudospin operator $\vec{n}_{\bar{\mathbf{k}}}\cdot\vec{\hat{\sigma}}$; due to spin-orbit coupling, surface states are never eigenstates of the physical spin operator $\vec{\hat{S}}$.

We can read off that the pseudospin of the state $|\phi^+(\bar{\mathbf{k}})\rangle$ with positive energy $\epsilon_{\bar{\mathbf{k}}}$ is $\vec{n}_{\bar{\mathbf{k}}}$, or

$$\langle\phi^+(\bar{\mathbf{k}})|\vec{\hat{\sigma}}|\phi^+(\bar{\mathbf{k}})\rangle = \vec{n}_{\bar{\mathbf{k}}} = [-\sin\theta_{\bar{\mathbf{k}}}|A_\theta|w\bar{w}_d(\theta), w\cos\theta_{\bar{\mathbf{k}}}, \sin\theta_{\bar{\mathbf{k}}}B_\theta], \quad (109)$$

where we have defined $\sin\theta_{\bar{\mathbf{k}}} = |v_2|\bar{k}_y/\epsilon_{\bar{\mathbf{k}}}$, $\cos\theta_{\bar{\mathbf{k}}} = |v_1|\bar{k}_x/\epsilon_{\bar{\mathbf{k}}}$. For the SEV we find

$$2\langle\phi^+(\bar{\mathbf{k}})|\vec{\hat{S}}|\phi^+(\bar{\mathbf{k}})\rangle = [-\sin\theta_{\bar{\mathbf{k}}}|A_\theta^+|w\bar{w}(\theta), \gamma_5^+ w\cos\theta_{\bar{\mathbf{k}}}, \sin\theta_{\bar{\mathbf{k}}}B_\theta^+] \quad (110)$$

with

$$A_\theta^+ = \frac{|h_1^v|\gamma_{11}^+\sin^2\theta + w|f_1^v|\gamma_5^+\cos^2\theta}{|\bar{f}_1^v|}, \quad (111)$$

$$B_\theta^+ = \frac{|h_1^v|\gamma_{11}^+ - w|f_1^v|\gamma_5^+}{|\bar{f}_1^v|}\sin\theta\cos\theta, \quad (112)$$

and

$$\bar{w}(\theta) = \mathrm{sgn}\left(|f_1^v|\gamma_5^+\cos^2\theta + w|h_1^v|\gamma_{11}^+\sin^2\theta\right) = \mathrm{sgn}\left[|f_1^v|\gamma_5^+ n^2 + w|h_1^v|\gamma_{11}^+(l^2+m^2)\right]. \quad (113)$$

Equations (109) and (110) constitute central results of this section, to be analyzed in the following. We first notice that there is no ϕ dependence, as a consequence of the cylindrical symmetry of the $\mathbf{k}\cdot\mathbf{p}$ Hamiltonian (33). For the in-plane SEV, we can define a θ-dependent winding number $\bar{w}(\theta)$. The winding number can be simply found by looking at the relative sign of the in-plane SEV component along $\bar{k}_x$ and $\bar{k}_y$, to get $\bar{w}(\theta) = \mathrm{sgn}(wA_\theta^+)$, leading to Eq. (113).

First, we will consider for simplicity $\bar{w}_d(\theta)$ from Eq. (106), which represents the winding number of the pseudospin [see Eq. (109)]. This winding number $\bar{w}_d(\theta)$ depends both on the surface geometry via the angle θ as well as on microscopic details of the material via $\mathbf{k}\cdot\mathbf{p}$ parameters f_1^v and h_1^v. As a consequence, $\bar{w}_d(\theta)$ is in general not uniquely determined by $w \equiv \mathrm{sgn}(\mathcal{C}_{k_z=0}^+\mathcal{C}_{k_z=\pi}^+)$, the latter characterizing the topological phase. The only exceptions are $\theta = 0$ and $\pi/2$. In particular, for $\theta = 0, \bar{w}_d(0) = +1$, which says that the $\bar{\Gamma}$ cone on the (001) surface always has a positive winding number due to its high symmetry (see Sec. IV). When $\theta = \pi/2$, instead, $\bar{w}_d(\pi/2) = w$, which says that for the $\bar{X}$ cone on the (100) surface the winding number depends directly on the topological phase (see Sec. V). This also applies to the $\bar{X}$ cone of all $(lm0)$ surfaces [but only at small momenta, whereas on the (001) surface it holds at any momenta as a consequence of mirror planes [21,22]]. We further notice that $\bar{w}_d(\theta)$ is always positive if $w = +1$. In contrast, for $w = -1$ there exists a critical angle $\theta_c = \arctan(f_1^v/h_1^v)^2$ such that $\bar{w}_d(\theta) = +1$ (-1) for $\theta < \theta_c$ $(\theta > \theta_c)$, respectively.

The qualitative behavior of the winding number of the SEV, $\bar{w}(\theta)$, is very similar to the one of the pseudospin, $\bar{w}_d(\theta)$. It displays a different critical value θ_c if $w = -1$, dictated by $A_{\theta_c}^+ = 0$ instead of $A_{\theta_c} = 0$, but remains $+1$ always if $w = +1$.

We then note that the SEV perpendicular to the surface is in general nonzero, unless $\theta = 0$, $\theta = \pi/2$, or $f_1^v = h_1^v$ (which corresponds to the limiting case of a hybridization with cubic symmetry in the $\mathbf{k}\cdot\mathbf{p}$ Hamiltonian). Being proportional to $\bar{k}_y$, it will point along the positive z direction on half of the cone, and along the negative direction on the other half. We stress that when $w = +1$, the out-of-plane component of the SEV and of the pseudospin is likely to be small since the two terms of Eqs. (112) and (102) tend to cancel each other ($|f_1^v| \approx |h_1^v|$), while it is expected to be large were the $w = -1$ phase realized, since in that case the two terms would sum. In this case, the effect would be mostly visible close to θ_c; in particular, exactly at θ_c, at $\bar{k}_x = 0$ the SEV would point perpendicular to the surface.

For Γ_7 states, results for the pseudospin are identical; for the real spin, we have to substitute $\gamma_5^\pm, \gamma_{11}^\pm \to \gamma_5^\mp$: as usual, this implies that the SEV has opposite sign with respect to Γ_8 states, so it is antiparallel to the pseudospin. For the Γ_7-Γ_8 case, results for the pseudospin are identical, with the usual redefinition of w according to Eq. (62); for the real spin, we have to substitute $\gamma_5^\pm, \gamma_{11}^\pm \to \gamma_5^{\pm'}, \gamma_{11}^{\pm'}$. As already remarked in Sec. V, the SEV is usually either parallel (when $|\beta_1| \gg |\beta_7|$) or antiparallel (when $|\beta_7| \gg |\beta_1|$) to the pseudospin, while for $|\beta_1| \sim |\beta_7|$ pathological situations can arise, in which the SEV is somewhere parallel, somewhere else antiparallel to the pseudospin in a momentum-dependent way; we, however, ignore this (unlikely) situation.

The possible scenarios for the spin structure are summarized in Fig. 8. We stress that these results refer to the $\omega = 0$ case; for finite ω one has to rigidly rotate these patterns by an angle ω.

We now apply this general theory to a few particular cases. We note that, when compared to tight-binding results, the values of the velocities (95) and (96) are not exact. As explained in Appendix D, higher-order terms in $\mathbf{k}$ need to be kept to reproduce these velocities exactly: while those can be easily taken into account for the (001) surface, on a general (lmn) it is not straightforward, so in what follows we will stick to the simple theory of this section. We finally remark that keeping more terms will also in general break the cylindrical symmetry of the Hamiltonian (33) by introducing a ϕ dependence in the effective Hamiltonian.

D. Results for (001) surface

First, we can obtain again the results of Secs. IV and V for a (001) surface. For the $\bar{\Gamma}$ cone, $\theta = 0, \bar{w}(0) = \bar{w}_d(0) = +1, B_0 = 0, A_0^+ = w\gamma_5^+, A_0 = w$. The effective Hamiltonian (105) corresponds to Eq. (42) with $v_x = v_y \equiv v_0$ (there we showed $\hat{s}_{x,y} = \hat{\sigma}_{x,y}$). The SEV (110) becomes Eq. (48); the pseudospin (109) gives Eq. (49).

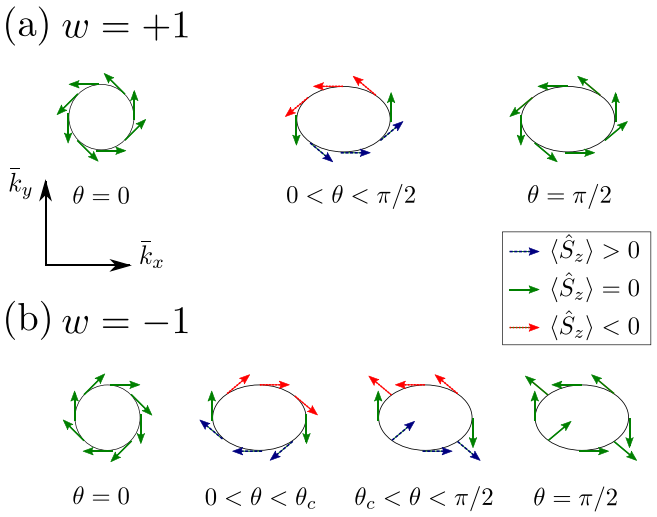

FIG. 8. Possible scenarios for the SEV of a Dirac cone at linear order in the $\mathbf{k} \cdot \mathbf{p}$ expansion on a general (lmn) surface, as a function of $w \equiv \mathrm{sgn}(\mathcal{C}^+_{k_z=0}\mathcal{C}^+_{k_z=\pi})$ and of $\theta \equiv \arctan \sqrt{l^2+m^2}/n$. (a) When $w = +1$, the winding number is positive for every $\theta, \bar{w}(\theta) = +1$. When $\theta \neq 0, \pi/2$, the SEV acquires an out-of-plane component (in the figure encoded by the color of the arrows), which is proportional to $\bar{k}_y = 0$, and depends on the parameter B^+_θ of Eq. (112), which is in general small. (b) When $w = -1$, the winding number is negative when θ is larger than a critical value θ_c, and in particular when $\theta = \pi/2$, and positive when $\theta < \theta_c$, and in particular when $\theta = 0$. Like for $w = +1$, when $\theta \neq 0, \pi/2$, the SEV acquires an out-of-plane component, which in this case can be large.

For the $\bar{X}$ cone, $\theta' = \theta'' = \pi/2, \bar{w}(\pi/2) = \bar{w}_d(\pi/2) = w, B_{\pi/2} = 0, A^+_{\pi/2} = \gamma^+_{11}, A_{\pi/2} = 1$. The effective Hamiltonian (105) becomes Eq. (79). The SEV (110) becomes Eq. (80); the pseudospin (109) gives Eq. (81). Results for the $\bar{X}'$ cone can be achieved by rotating the results for $\bar{X}$ by the same angle $\omega = \pi/2$ in both momentum and spin space.

Predictions for the SEV in the small-momentum limit for this surface, when $w = +1$, are shown in Fig. 9(a). As remarked, these predictions hold also for larger momenta along high-symmetry directions.

E. Results for (110) surface

On this surface, one bulk X point is projected onto $\bar{X}$, while two X points are projected onto $\bar{Y}$. We start with $\bar{X}$ which corresponds to the triplet (11/0), hence giving $\theta = \pi/2$. We observe that it is the same value of θ which describes the $\bar{X}$ cone on the (001) surface; hence, we can apply most of the results of Sec. V and of the previous subsection. In particular, the effective Hamiltonian is

$$H^{\mathrm{eff}}_{\theta=\pi/2} = |v_1| w \bar{k}_x \hat{\sigma}_y - |v_2| \bar{k}_y \hat{\sigma}_x, \tag{114}$$

and the SEV on eigenstates is given by

$$2\langle \phi^+(\mathbf{k}) | \vec{\hat{S}} | \phi^+(\mathbf{k}) \rangle = (-\sin\theta_{\mathbf{k}} \gamma^+_{11}, \cos\theta_{\mathbf{k}} \gamma^+_5, 0), \tag{115}$$

so the SEV lies in the surface plane, and w still denotes the SEV winding number. The only difference with respect to Sec. V is that here we cannot express our basis with a quantization axis perpendicular to the surface without enlarging the basis [as we did in Eq. (70)] because a $\phi = \pi/4$ rotation does not belong to cubic symmetry operations. We can only state that, in our approximation, surface states at $\bar{X}$ are composed of $\Gamma^{(1)}_8$ and $d_{x^2-y^2}$ states w.r.t. a quantization axis parallel to $\bar{k}_x$.

In fact, this same theory applies to all $(lm0)$ surfaces, which all have a Dirac cone at $\bar{X}$. For the (110) surface, which has C_{2v} symmetry, the spin remains within the surface plane even beyond the present approximation (see Sec. V). However, other surfaces have only C_s symmetry, not containing a rotation by π, and the SEV can point out of the surface beyond this approximation.

Turning to the cones at $\bar{Y}$, we note that in the low-order $\mathbf{k} \cdot \mathbf{p}$ approximation they are projected exactly at the same energy, which is given by Eq. (99) with $\theta' = \theta'' = \pi/4$. We also find $\omega' = -\pi/2$, $\omega'' = \pi/2$, which implies that one cone is rotated by π with respect to the other one. This means that their combined SEV perpendicular to the surface is zero in agreement with C_{2v} symmetry.

However, when solving the tight-binding model [19], the two cones are projected at *different* energies. They then anticross, hence get gapped and become topological trivial, except along the $\bar{\Gamma}$-$\bar{Y}$ direction where their crossing leads to two new cones protected by mirror symmetry (see Fig. 10). These cones are topological nontrivial but not originating from parity invariants, such that the $\mathbf{k} \cdot \mathbf{p}$ method is not applicable as noted before. Predictions for the SEV in the small-momentum limit for this surface, when $w = +1$, are shown in Fig. 9(c).

We note that, provided that the Fermi energy lies above the Dirac energy of all cones, our results are compatible with that of a very recent ARPES experiment [26] on SmB_6 where two surface states were observed, centered at $\bar{X}$ and $\bar{Y}$, respectively.

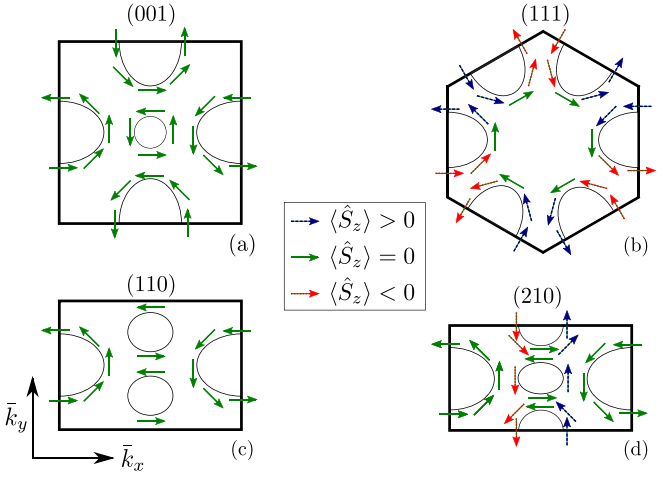

FIG. 9. Predicted SEV for surface states above the Dirac energies from the perturbative calculation in the small-momentum limit, when we assume $w = +1$, for all the surfaces considered in this paper: (a) (001), (b) (111), (c) (110) and $(lm0)$ with $l + m$ even, (d) (210) and $(lm0)$ with $l + m$ odd. In all Dirac cones at high-symmetry points the winding number is positive; for Dirac cones not at high-symmetry points, i.e., the two central cones in case (c), our perturbative approach cannot be applied so we cannot make predictions, except along the high-symmetry direction $\bar{k}_x = 0$. The color of the arrows encodes the expectation value of the spin perpendicular to the surface as in Fig. 8; this value is generally small.

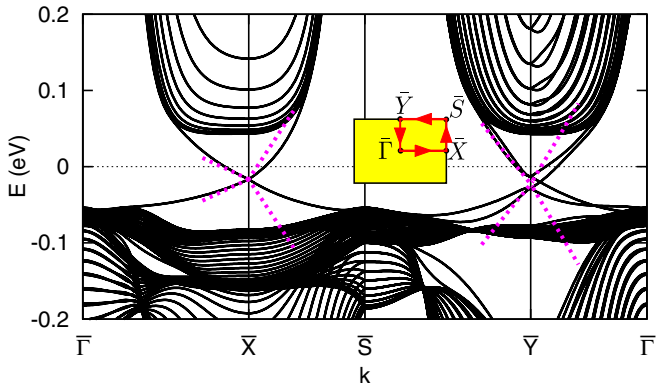

FIG. 10. Tight-binding band structure for a (110) slab of 30 layers, together with the analytical $\mathbf{k}\cdot\mathbf{p}$ approximation of surface states for the same parameters as Fig. 3. Note that the low-order $\mathbf{k}\cdot\mathbf{p}$ approximation yields two identical cones at $\bar{Y}$, while in the full solution the two cones hybridize and gap out, except along the $\bar{Y}$-$\bar{\Gamma}$ direction, where two new cones protected by mirror symmetry appear (only one is shown).

In that case, the signal at $\bar{Y}$ should arise from two nearly degenerate cones.

F. Results for (111) surface

In this case, all indices are equal, and $\theta=\theta'=\theta''=\arctan\sqrt{2}$. The X point is projected at $\bar{M}=(2\pi/\sqrt{6},0)$. This is the situation in which none of the terms in Eq. (105) vanish. The SEV can point out of the surface, and the winding number depends on model details according to

$$\bar{w}_d(\theta=\arctan\sqrt{2})=\mathrm{sgn}\left(2w\left|h_1^v\right|+\left|f_1^v\right|\right). \tag{116}$$

The two other cones, at $\bar{M}'$ and $\bar{M}''$, are equivalent to the one at $\bar{M}$, and their effective Hamiltonians and SEV can be found after a $\omega',\omega''=\pm 2\pi/3$ rotation.

Predictions about the SEV in the small-momentum limit for this surface, when $w=+1$, are shown in Fig. 9(b); an example of the band structure is given in Fig. 11.

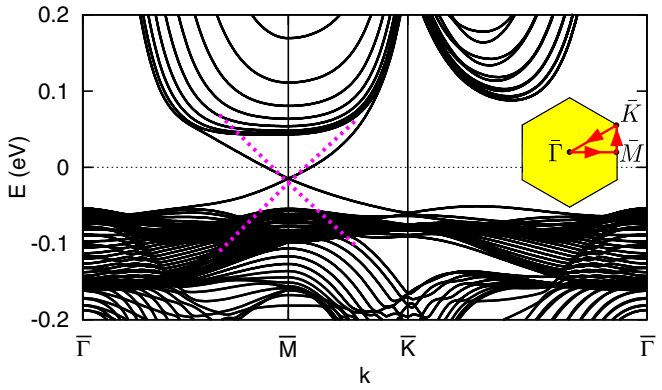

FIG. 11. Tight-binding band structure for a (111) slab of 30 layers, and analytical $\mathbf{k}\cdot\mathbf{p}$ approximation of surface states for the same parameters as Fig. 3. We show just one of the three equivalent $\bar{M}$ points.

G. Results for ($lm0$) surfaces

Now, we consider a ($lm0$) surface for which $\theta=\pi/2$. Equations (91), (92), and (93) yield

$$\bar{\mathbf{k}}_X=(\pi,0), \tag{117}$$

$$\bar{\mathbf{k}}_{X'}=(0,-\pi\sin\phi)=(0,-m\pi/\sqrt{l^2+m^2}), \tag{118}$$

$$\bar{\mathbf{k}}_{X''}=(0,\pi\cos\phi)=(0,l\pi/\sqrt{l^2+m^2}). \tag{119}$$

The 2D BZ is defined by $\mathbf{k}_1=(2\pi,0)$, $\mathbf{k}_2=(0,2\pi/\sqrt{l^2+m^2})$, so $\bar{\mathbf{k}}_{X''}-\bar{\mathbf{k}}_{X'}=(0,(l+m)\pi/\sqrt{l^2+m^2})$ is zero up to a multiple of $\mathbf{k}_2$ if $l+m$ is even, while it is equal to $\mathbf{k}_2/2=(0,\pi/\sqrt{l^2+m^2})$ when $l+m$ is odd. We thus arrive at the conclusion that if $(l+m)$ is even, both X' and X'' are projected onto the same 2D BZ point, and parity invariants predict a single Dirac point at $\bar{X}$, while, if $(l+m)$ is odd, X' and X'' are projected onto different 2D BZ points, and parity invariants predict three Dirac points at $\bar{X},\bar{Y},\bar{\Gamma}$. In the first case, to which the (110) surface belongs, MCNs still predict two Dirac cones along the $\bar{Y}$-$\bar{\Gamma}$ direction; while, in the second case, to which the (210) surface belongs, there are already two Dirac cones along this direction predicted by parity invariants, so MCNs do not predict any more cones.

In addition, when $l\neq m$, so, for all these surfaces except the (110) one, the $k_x=k_y$ mirror plane is no more projected onto $\bar{k}_y=0$, while $k_z=0,\pi$ is always projected onto $\bar{k}_x=0,\pi$, so two mirror planes survive. However, no Dirac cone is cut by two mirror planes, so we cannot in general define winding numbers without resorting to a concrete model; and, when it exists, the $\bar{\Gamma}$ cone is anisotropic since $\bar{k}_x$ and $\bar{k}_y$ correspond to inequivalent bulk directions, except on the (001) surface.

For the (210) surface, the cone at $\bar{\Gamma}$ is described by $\theta''=\arctan 2$, and the cone at $\bar{Y}$ by $\theta'=\arctan(1/2)$; $\bar{X}$ corresponds to $\theta=\pi/2$, always leading to winding number $\bar{w}(\theta)=w$. We can thus see that, varying l and m, this class of surfaces allows to tune the winding number on the $\bar{\Gamma}$ and $\bar{Y}$ cones when $w=-1$.

We remark that, except for the (110) one, these surfaces have C_s symmetry, which does not contain rotations by π, so in general the SEV can point also out of plane: this happens already in the low-order $\mathbf{k}\cdot\mathbf{p}$ approximation for cones $\bar{\Gamma}$ and $\bar{Y}$, while for $\bar{X}$ we would need to keep more terms in the small-momentum expansion. A numerical diagonalization of the tight-binding model shows that, with reference to Fig. 9(d) (where we show predictions about the SEV in the small-momentum limit), when $w=+1,\langle\hat{S}_z\rangle<0$ for $\bar{k}_x-\pi<0$, and $\langle\hat{S}_z\rangle>0$ otherwise. In Fig. 12, we give an example for the band structure.

H. Summary of results on different surfaces

At this point, it is useful to summarize our main results for SmB_6 surface states. All Dirac cones can be described by a generalized Dirac Hamiltonian, and the winding number of the SEV, defined ignoring the out-of-plane component of the spin, is $\bar{w}(\theta)$ in Eq. (113). For $\theta=\pi/2$, corresponding to the $\bar{X}$ cone on the (001) surface, we get

$$\bar{w}_d(\pi/2)=\bar{w}(\pi/2)=w=\mathrm{sgn}\left(f_1^v h_1^v\right)=\mathrm{sgn}(\mathcal{C}^+_{k_z=0}\mathcal{C}^+_{k_z=\pi}). \tag{120}$$

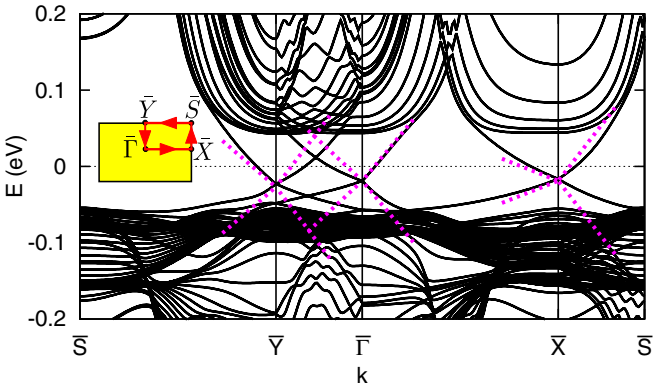

FIG. 12. Tight-binding band structure for a (210) slab of 30 layers, and analytical $\mathbf{k}\cdot\mathbf{p}$ approximation of surface states for the same parameters as Fig. 3.

Making use of the experimental fact [14] that the winding number of this cone is $w=+1$ we deduce that

$$\bar{w}_d(\theta)=\mathrm{sgn}\left(\sin^2\theta\left|h_1^v\right|+\cos^2\theta\left|f_1^v\right|\right)=+1=\bar{w}(\theta). \tag{121}$$

Hence, the winding number $\bar{w}(\theta)$ is $+1$ for all Dirac cones on all surfaces; exceptions could by those Dirac cones protected by mirror symmetry only [being present on $(lm0)$ surface with $(l+m)$ even], as the $\mathbf{k}\cdot\mathbf{p}$ approach is not applicable there. A concise summary is in Table I and Fig. 9.

To derive these results, the following approximations were made, to be discussed in turn: (i) We have used an effective single-particle approach, (ii) we have worked in the small-momentum limit, (iii) we have ignored the coupling to subspace 2, (iv) we have treated the interplay between Γ_7 and Γ_8 states in an approximate way, and (v) we have ignored surface details.

Approximation (i) implies that, after renormalization effects due to the Hubbard repulsion taken into account, the SEV behaves as in the noninteracting picture. This is based on assumptions frequently made in the field of heavy-fermion metals [33], but would need to be verified in many-body calculations based, e.g., on dynamical mean-field theory (DMFT). Approximation (ii) is standard in the context of TI surface states; we remark that, on the (001) surface, the presence of mirror planes allows to extend our results to larger momenta [21]. Approximation (iii) can be verified within our model by comparing to tight-binding results, and we have found it justified in all the cases we analyzed. Approximation (iv) is somewhat delicate, as both Γ_7 and Γ_8 states are known to be close to the Fermi energy [2,35], and, as a consequence, both contribute to surface states. We have argued in Ref. [21] that a minimal model can ignore Γ_7 states, but a definite answer requires more accurate *ab initio* calculations which are not available at present. Approximation (v) requires thorough consideration, especially because SmB_6 surfaces are known not to cleave well [41,42]. On the (001) surface, topological arguments can help making general claims [21,22], but on other surfaces microscopic details may become important. We have recently studied effects of surface reconstruction and surface scattering potentials for the (001) surface within

TABLE I. For each (lmn) surface we report its symmetry ("/" denoting no symmetry), the surface momenta $\bar{\mathbf{k}}_X$ to which each of the X points is projected, the corresponding (lm/n) triplet, which is obtained fixing the z direction in the $\mathbf{k}\cdot\mathbf{p}$ Hamiltonian, the symmetry at $\bar{\mathbf{k}}_X$, the angle θ at which the X point is projected on the surface, and the pseudospin winding number $\bar{w}_d(\theta)$ from Eq. (106); for the physical spin, a similar result is given by Eq. (113). For $(lm0)$ surfaces we assume l odd, m even. In the definition of surface momenta $\bar{\mathbf{k}}_X$ we keep minus signs to agree with the general (lmn) formulas of the last three rows. The asterisk denotes that on the (110) surface we can formally apply our theory to the two cones at $\bar{Y}$, but those become topologically trivial since they come in pair.

Surface	Symm.	Triplet	$\bar{\mathbf{k}}_X$	S. at $\bar{\mathbf{k}}_X$	θ	$\bar{w}_d(\theta)$
(001)	C_{4v}	(00/1)	$\bar{\Gamma}=(0,0)$	C_{4v}	0	1
		(01/0)	$\bar{X}=(\pi,0)$	C_{2v}	$\pi/2$	w
		(10/0)	$\bar{X}'=(0,\pi)$	C_{2v}	$\pi/2$	w
(110)	C_{2v}	(11/0)	$\bar{X}=(-\pi,0)$	C_{2v}	$\pi/2$	w
		(10/1)	$\bar{Y}=(0,-\pi/\sqrt{2})$	C_s	$\pi/4^*$	$\mathrm{sgn}(\lvert f_1^v\rvert+w\lvert h_1^v\rvert)^*$
		(01/1)	$\bar{Y}=(0,\pi/\sqrt{2})$	C_s	$\pi/4^*$	$\mathrm{sgn}(\lvert f_1^v\rvert+w\lvert h_1^v\rvert)^*$
(111)	C_{3v}	(11/1)	$\bar{M}=(-2\pi/\sqrt{6},0)$	C_s	$\arctan\sqrt{2}$	$\mathrm{sgn}(\lvert f_1^v\rvert+2w\lvert h_1^v\rvert)$
		(11/1)	$\bar{M}'=(\pi/\sqrt{6},-\pi/\sqrt{2})$	C_s	$\arctan\sqrt{2}$	$\mathrm{sgn}(\lvert f_1^v\rvert+2w\lvert h_1^v\rvert)$
		(11/1)	$\bar{M}''=(\pi/\sqrt{6},\pi/\sqrt{2})$	C_s	$\arctan\sqrt{2}$	$\mathrm{sgn}(\lvert f_1^v\rvert+2w\lvert h_1^v\rvert)$
(210)	C_s	(21/0)	$\bar{X}=(-\pi,0)$	C_s	$\pi/2$	w
		(10/2)	$\bar{Y}=(0,-\pi/\sqrt{5})$	C_s	$\arctan(1/2)$	$\mathrm{sgn}(4\lvert f_1^v\rvert+w\lvert h_1^v\rvert)$
		(02/1)	$\bar{\Gamma}=(0,0)$	C_s	$\arctan(2)$	$\mathrm{sgn}(\lvert f_1^v\rvert+4w\lvert h_1^v\rvert)$
$(lm0)$	C_s	$(lm/0)$	$\bar{X}=(-\pi,0)$	C_s	$\pi/2$	w
l even		$(m0/l)$	$\bar{Y}=(0,-\frac{\pi}{\sqrt{m^2+n^2}})$	C_s	$\arctan(m/l)$	$\mathrm{sgn}(l^2\lvert f_1^v\rvert+wm^2\lvert h_1^v\rvert)$
m odd		$(0l/m)$	$\bar{\Gamma}=(0,0)$	C_s	$\arctan(l/m)$	$\mathrm{sgn}(m^2\lvert f_1^v\rvert+wl^2\lvert h_1^v\rvert)$
(lmn)	/	(lm/n)	$\bar{\mathbf{k}}_X=\pi(-\frac{\sqrt{l^2+m^2}}{\sqrt{l^2+m^2+n^2}},0)$	/	$\arctan(\sqrt{l^2+m^2})/n)$	$\mathrm{sgn}(n^2\lvert f_1^v\rvert+w(l^2+m^2)\lvert h_1^v\rvert)$
		(mn/l)	$\bar{\mathbf{k}}_{X'}=\frac{\pi}{\sqrt{l^2+m^2}}(\frac{nl}{\sqrt{l^2+m^2+n^2}},-m)$	/	$\arctan(\sqrt{m^2+n^2})/l)$	$\mathrm{sgn}(l^2\lvert f_1^v\rvert+w(m^2+n^2)\lvert h_1^v\rvert)$
		(nl/m)	$\bar{\mathbf{k}}_{X''}=\frac{\pi}{\sqrt{l^2+m^2}}(\frac{mn}{\sqrt{l^2+m^2+n^2}},l)$	/	$\arctan(\sqrt{n^2+l^2})/m)$	$\mathrm{sgn}(m^2\lvert f_1^v\rvert+w(n^2+l^2)\lvert h_1^v\rvert)$

tight-binding models in some detail [39], showing that band backfolding and the possibly resulting crossings of Dirac cones are the main effects. Similar studies for other surfaces are left for future work.

VII. TOPOLOGICAL PHASE TRANSITIONS

The first part of the paper, together with previous work [21,22], that the spin winding numbers $\bar{w}(\theta)$ for surface Dirac cones depend on the relative strength of different hybridization terms, with a central role played by the combination of MCNs $w \equiv \mathrm{sgn}(\mathcal{C}^+_{k_z=0}\mathcal{C}^+_{k_z=\pi})$. This prompts us to study the possibility of bulk topological phase transitions between states with different $w = \pm 1$ which could be observed as a change in the spin structure of surface states; this is the subject of the second part of the paper. We will consider the tuning of both hybridization terms and crystal-field splitting, noting that the latter is more likely to be accessible by pressure or doping.

A. Varying the hybridization

Theoretically, the easiest way to induce a topological transition is to consider two different hybridization terms in a given model and to change their relative strength [22]. For example, we can take the E_g-Γ_8 model with hybridization terms η_x^{v2} and η_z^{v2}, both leading to a fully insulating phase, the first one with $w = -1$ and the second one with $w = +1$. We now study how the system evolves when we take $\eta_x^{v2} = \cos\xi$, $\eta_z^{v2} = \sin\xi$, so that $\xi = 0$ yields $w = +1$ and $\xi = \pm\pi/2$ yields $w = -1$. When we retain these two hybridization terms, we get $f_1^v(\xi) = 2\cos\xi + 6\sin\xi$, $h_1^v(\xi) = -3\cos\xi + 3\sin\xi$, so $w(\xi) = \mathrm{sgn}[f_1^v(\xi)h_1^v(\xi)]$, and we expect a topological phase transition for $w(\xi_c) = 0$, so when $2\cos\xi + 6\sin\xi = 0$, leading to $\xi_{c1} = -\arctan(1/3)$, or when $-3\cos\xi + 3\sin\xi = 0$, leading to $\xi_{c2} = \pi/4$.

By numerically diagonalizing the tight-binding model, with results shown in Fig. 13(a), we find that this prediction is partially true, but the situation is more involved. When $f_1^v(\xi) = 0$ the gap closes at $\xi = \xi_{c1}$ along the X-Γ direction, and when $h_1^v(\xi) = 0$ the gap closes at $\xi = \xi_{c2}$ along the X-M direction. However, a third transition at $\xi = \xi_{c3}$, whose value is parameter dependent, occurs along the X-R direction. To account for this third transition requires to take into account the full momentum dependence of the hybridization term [22] or at least higher-order terms in the $\mathbf{k}\cdot\mathbf{p}$ expansion (see Appendix D). In general, the closing of the gap along X-M and X-R does not happen at the same energy; when $\xi_{c3} < \xi < \xi_{c2}$, we find a phase with MCNs $(-2,-3,-1)$. For the $\mathbf{k}\cdot\mathbf{p}$ Hamiltonian with all eight orbitals [Fig. 13(b)] and with the four orbitals in subspace 1 [Fig. 13(c)], the gap closes for the predicted values of ξ_{c1} and ξ_{c2}, but the $(-2,-3,-1)$ phase is not described.

As a second example, we consider tuning via $\eta_z^{v1} = \cos\xi$, $\eta_z^{v2} = \sin\xi$. In this case, the $\mathbf{k}\cdot\mathbf{p}$ Hamiltonian with four orbitals predicts a bulk gap closing at $\xi_{c1} = 0$ and $\xi_{c2} = \arctan(1/2) \simeq 0.15\pi$, as shown in Fig. 14(c). The tight-binding model [Fig. 14(a)] confirms that $\xi_{c1} = 0$, but also gives $\xi_{c2} = 0.11\pi$, $\xi_{c3} = 0.18\pi$, with a $(+2,-3,+1)$ phase for $\xi_{c2} < \xi < \xi_{c3}$. The $\mathbf{k}\cdot\mathbf{p}$ Hamiltonian with all eight orbitals [Fig. 14(b)] in contrast to the reduced $\mathbf{k}\cdot\mathbf{p}$ Hamiltonian with four orbitals, yields $\xi_{c3} \neq \xi_{c2}$, with values only slightly different from the tight-binding solution ($\xi_{c2} = 0.10\pi$, $\xi_{c3} = 0.21\pi$). This shows that in this case, to justify $\xi_{c3} \neq \xi_{c2}$ and the presence of the additional $(+2,-3,+1)$ phase, one has to take into account the coupling to subspace 2. We note that it is exactly this coupling, described by parameters $h_{12}^v, h_{21}^v, h_{17}^v$, that lowers the cylindrical symmetry of the $\mathbf{k}\cdot\mathbf{p}$ Hamiltonian restricted to subspace 1 [Eq. (33)] to the tetragonal symmetry of the full $\mathbf{k}\cdot\mathbf{p}$ Hamiltonian [Eq. (23)], making the X-M and X-R directions inequivalent, hence allowing $\xi_{c3} \neq \xi_{c2}$.

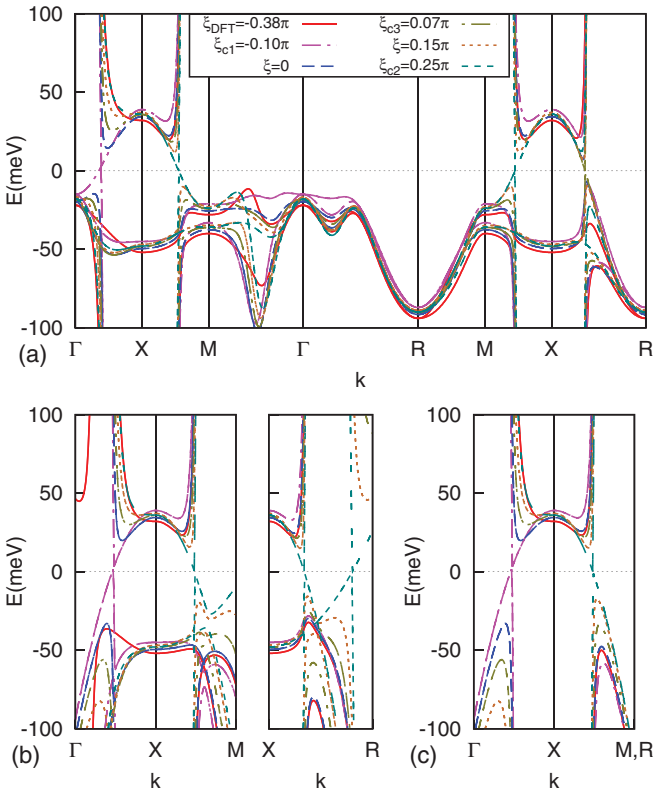

FIG. 13. Evolution of the band structure as a function of the hybridization for the E_g-Γ_8 model when $\eta_x^{v2} = \cos\xi$, $\eta_z^{v2} = \sin\xi$, (a) for the tight-binding model, (b) for the $\mathbf{k}\cdot\mathbf{p}$ Hamiltonian, (c) for the $\mathbf{k}\cdot\mathbf{p}$ Hamiltonian in subspace 1. In (a), the gap closes along X-Γ at $\xi_{c1} = -\arctan(1/3) \simeq -0.1\pi$, along X-M at $\xi_{c2} = \pi/4$, and along X-R at $\xi_{c3} \simeq 0.07\pi$ denoting the topological phase transitions among the three phases $(+2,+1,-1)$ (red curve), $(-2,+1,+1)$ (blue curve), $(-2,-3,-1)$ (orange curve). This is summarized in Fig. 15(a). In (b) and (c), $\xi_{c3} = \xi_{c2}$; in (b) the second pair of bands crossing along X-R is in subspace 2 due to the vanishing of h_2^v. Other nonzero parameters are $t_c = 0.8$ eV, $t_f = -0.015$ eV, $V = 0.03$ eV, $\eta_z^{d1} = \eta_z^{f1} = 0.8$, $\eta_z^{d2} = \eta_z^{f2} = -0.3$, $\epsilon_d - \epsilon_8 = 1.45$ eV, which are chosen to reproduce qualitatively (but not quantitatively) the band structure of Refs. [30,31].

The MCNs can be understood by the fact that, when the gap closes along X-Γ (so, four times at $k_z = 0$ and twice at $k_x = k_y$), MCNs change by $(\pm 4,0,\pm 2)$, along X-M (four times at $k_z = 0$ and $k_z = \pi$) by $(\pm 4,\pm 4,0)$, and along X-R (four times at $k_z = \pi$ and twice $k_x = k_y$) by $(0,\pm 4,\pm 2)$ [22]. As a consequence, the properties $\mathcal{C}^+_{k_z=0} = 2 \mod 4$, $\mathcal{C}^+_{k_z=\pi} = 1 \mod 4$, $\mathcal{C}^+_{k_x=k_y} = 1 \mod 2$ are always satisfied. We recall that higher MCNs lead, in general, to more surface Dirac cones.

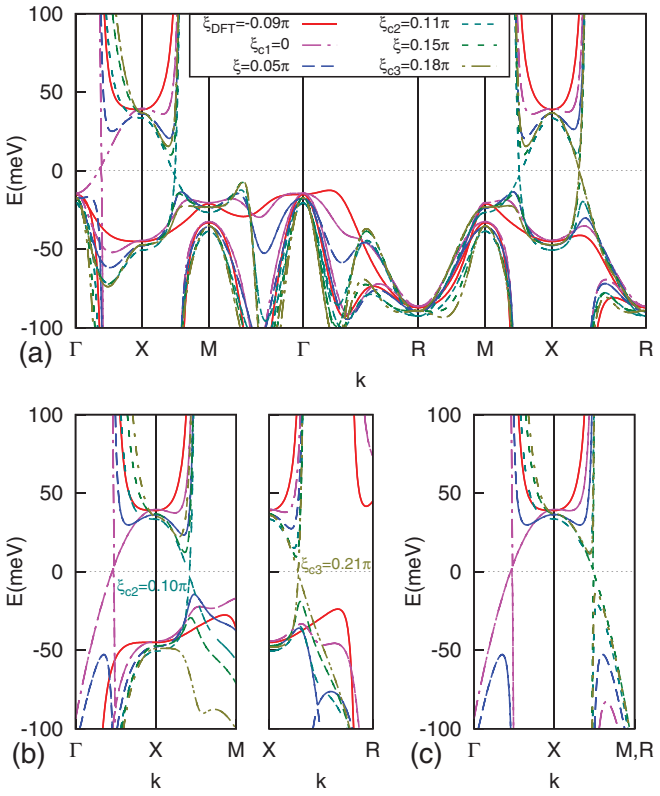

FIG. 14. Same as Fig. 13 but with $\eta_z^{v1} = \cos\xi$, $\eta_z^{v2} = \sin\xi$. In (a), the gap closes along X-Γ at $\xi_{c1} = 0$, along X-M at $\xi_{c2} \simeq 0.11\pi$, and along X-R at $\xi_{c3} \simeq 0.18\pi$ denoting the topological phase transitions among the three phases $(+2,+1,-1)$ (red curve), $(-2,+1,+1)$ (blue curve), $(+2,-3,+1)$ (green curve). This is summarized in Fig. 15(b). In (b), $\xi_{c2} = 0.10\pi$, $\xi_{c3} = 0.21\pi$; in (c) $\xi_{c3} = \xi_{c2} = \arctan(1/2) \simeq 0.15\pi$.

To conclude, in our cylindrical approximation the $\mathbf{k}\cdot\mathbf{p}$ method restricted to subspace 1 always gives $\xi_{c2} = \xi_{c3}$, predicting only the $w = \pm 1$ phases. In contrast, additional intermediate phases $(+2,-3,+1)$ or $(-2,-3,-1)$, with $\xi_{c2} \neq \xi_{c3}$, exist once the symmetry is lowered from cylindrical to tetragonal, by keeping either all orbitals or more terms in the $\mathbf{k}\cdot\mathbf{p}$ expansion; this is generally achieved in the tight-binding model. (Such phases were already discussed in Ref. [22] for a simplified model.) Schematic phase diagrams are shown in Fig. 15; similar results are achieved for all other pairs of hybridization terms.

We remark that, using realistic parameters for SmB_6 from DFT/Wannier calculations [30,31], $\eta_z^{v2}/\eta_x^{v2} \simeq -2.6$, $\eta_z^{v2}/\eta_z^{v1} \simeq -0.3$ (denoted as $\xi_{\rm DFT}$ in Fig. 14), so in both cases we are deep in the $(+2,+1,-1)$ $(w=+1)$ phase. This remains true even when considering more hybridization terms, so the Γ_8-only model has $w = +1$ and is most likely not close to a phase transition.

From Fig. 16(a) we see that across the $w = +1 \leftrightarrow w = -1$ transition, the SEV on the $\bar{\Gamma}$ cone is reversed, just like the SEV on the $\bar{X}$ cone along the $\bar{X}$-$\bar{\Gamma}$ direction, as a consequence of the change of surface mirror eigenvalues. Along the $\bar{X}$-$\bar{M}$ direction, instead, the SEV is the same because $\mathcal{C}^{+}_{k_z=\pi} = +1$ is left invariant. As shown in Refs. [21,43], the spin structure

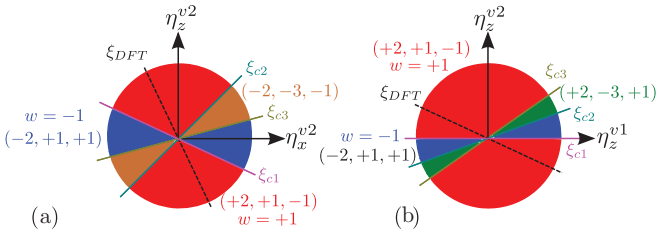

FIG. 15. Topological crystalline phases as a function of two hybridization parameters, (a) $\cos\xi = \eta_x^{v2}$, $\sin\xi = \eta_z^{v2}$, (b) $\cos\xi = \eta_z^{v1}$, $\sin\xi = \eta_z^{v2}$. The bulk gap closes along X-Γ at ξ_{c1}, along X-M at ξ_{c2}, along X-R at ξ_{c3}. The phases $(+2,+1,-1), w=+1$ and $(-2,+1,+1), w=-1$ always appear; according to the relative value of $\xi_{c1},\xi_{c2},\xi_{c3}$, a third phase can appear, which is (a) $(-2,-3,-1)$, corresponding to Fig. 13, or (b) $(+2,-3,+1)$, corresponding to Fig. 14; these two additional phases are not predicted by the $\mathbf{k}\cdot\mathbf{p}$ method, for which $\xi_{c2} = \xi_{c3}$, since they require the knowledge of the full momentum dependence of the hybridization. In both cases, the physical system is in the $(+2,+1,-1)$, $w=+1$, phase, as denoted by $\xi_{\rm DFT}$; we note that the overall sign of the hybridization terms is arbitrary, so ξ is defined modulo π.

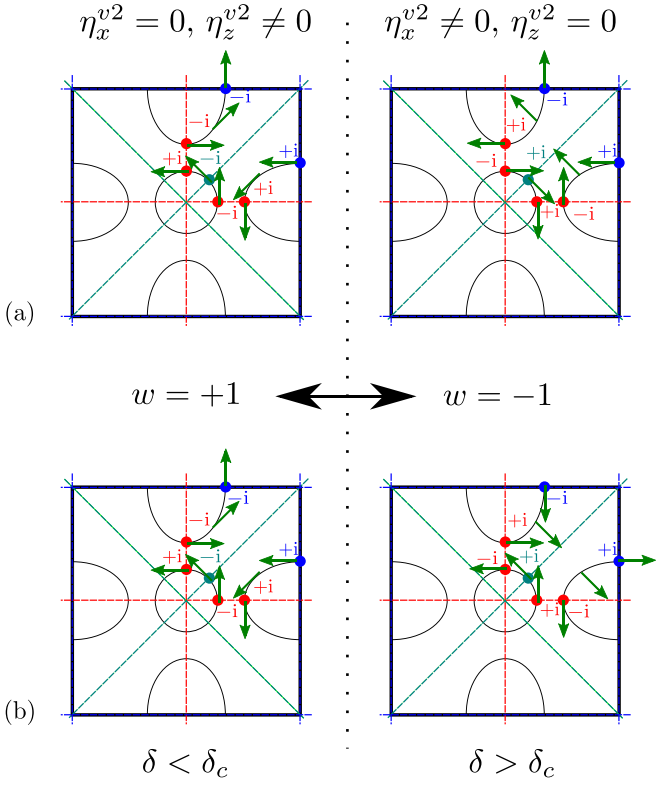

FIG. 16. Schematic $w=+1 \leftrightarrow w=-1$ transition for surface states on a (001) surface at energies above the Dirac points (a) varying the hybridization with Γ_8 states only, (b) varying the relative onsite energy of Γ_7 and Γ_8 states: when $\delta<\delta_c, w=+1$, surface states are mostly Γ_8, when $\delta>\delta_c, w=-1$, they are mostly Γ_7; mirror planes are as in Fig. 1. In both cases, mirror eigenvalues change in the same way, but, when $w=-1$, the spin in (b) is opposite as in (a), because Γ_7 states have opposite spin given the same mirror eigenvalues.

of the $\bar{X}$ cones strongly affects intercone scattering: as a consequence, in quasiparticle interference (QPI) experiments, the transition from $w=+1$ to $w=-1$ can be observed on a (001) surface by the appearance of peaks due to intercone $\bar{X}$-$\bar{X}'$ scattering.

We could repeat the same analysis with the Γ_7 doublet, with exactly the same results, the only difference being that the SEV would be everywhere reversed. From a quantitative point of view, following Refs. [30,31], the Γ_7-only model is in the $w=-1$ phase, and presumably far from a transition.

B. Varying the relative multiplet energy

A topological transition can also be realized by tuning the crystal-field splitting, based on the fact that, for realistic choices of the parameters, the E_g-Γ_8 model is in the $w=+1$ phase, while the E_g-Γ_7 one is in the $w=-1$ phase. Given that about half a hole is expected in the $j=\frac{5}{2}$ multiplet, large crystal-field splitting will put the hole in the energetically higher of the Γ_7 and Γ_8 multiplets which will then determine the value of w. In practice, since the crystal-field splitting is comparable to the kinetic energy, both multiplets will be partly unoccupied, and w results from a competition between the two. The ARPES results of Ref. [14] indicate that SmB_6 is in the $w=+1$ phase, which leads us to conclude that Γ_8 are more important [21]. Consequently, tuning the Γ_7 orbitals to higher energies can induce a transition to the $w=-1$ phase. Experimentally, this could be achieved, e.g., by negatively doping the B_6 cages (preserving cubic symmetry) since Γ_7 orbitals have maxima along their direction, while Γ_8 have minima. We note that a change of the crystal-field splitting might even be interaction induced [44], such that DFT and more advanced computational methods might predict different phase due to interaction-driven renormalizations; this is beyond the scope of this paper.

We can expect a phase transition when w from Eq. (62) is zero. We can here put $\beta_1 \equiv \cos\xi$, $\beta_7 \equiv \sin\xi$, leading to

$$w = \mathrm{sgn}\left[\left(f_1^v \cos\xi + f_7^v \sin\xi\right)\left(h_1^v \cos\xi + h_7^v \sin\xi\right)\right], \tag{122}$$

which gives $\tan\xi_{c1} = -f_1^v/f_7^v$ and $\tan\xi_{c2} = -h_1^v/h_7^v$. To simplify things, we use the results quoted in Appendix A and Refs. [30,31], which tell us that $f_1^v, h_1^v, h_7^v > 0, f_7^v < 0$. As a consequence, when the coupling m_{78} from Eq. (26) obeys $m_{78} > 0$ (corresponding to the physical system), only ξ_{c1} exists, which corresponds to $f_{17}^v = 0$, so to a gap closing along X-Γ. On the other hand, when $m_{78} < 0$, only ξ_{c2} exists, which corresponds to $h_{17}^v = 0$, so to a gap closing along X-M and X-R. Finally, if $m_{78} = 0$ we expect a gap closing at X.

We can also predict the value of Δ_c required for the transition

$$\Delta_c = m_{78}\frac{\left(f_1^v\right)^2 - \left(f_7^v\right)^2}{\left|f_1^v f_7^v\right|}, \quad m_{78} > 0 \tag{123}$$

$$\Delta_c = |m_{78}|\frac{\left(h_1^v\right)^2 - \left(h_7^v\right)^2}{h_1^v h_7^v}, \quad m_{78} < 0 \tag{124}$$

$$\Delta_c = 0, \quad m_{78} = 0. \tag{125}$$

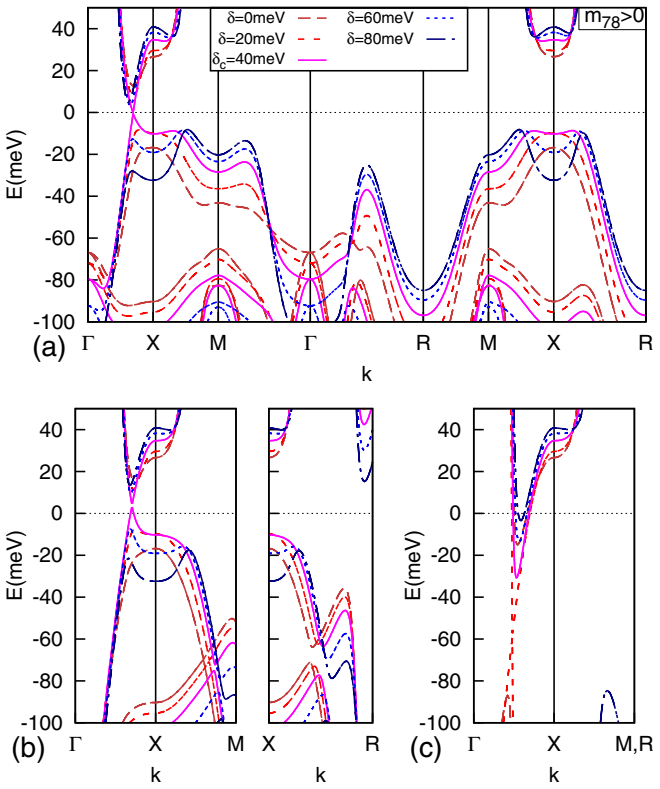

FIG. 17. Evolution of the band structure for the E_g-Γ_7-Γ_8 model as a function of the energy difference $\delta \equiv \epsilon_7 - \epsilon_8$ (crystal-field splitting) between the Γ_7 doublet and the Γ_8 quadruplet, (a) for the tight-binding model, (b) for the $\mathbf{k}\cdot\mathbf{p}$ Hamiltonian with all 10 orbitals, (c) for the $\mathbf{k}\cdot\mathbf{p}$ Hamiltonian with 4 orbitals, that we used in the text to allow for analytical calculations. In (a), the gap closes at $\delta = \delta_c$ along X-Γ denoting the topological phase transition: when $\delta < \delta_c$, $w = +1$, while when $\delta > \delta_c$, $w = -1$; in (b) the $\mathbf{k}\cdot\mathbf{p}$ method captures qualitatively and quantitatively the details of the transition; in (c) the reduced $\mathbf{k}\cdot\mathbf{p}$ method captures qualitatively the details of the transition, but it misses the exact value of δ_c. Nonzero parameters are $t_c = 0.8$ eV, $t_f = -0.015$ eV, $V = 0.05$ eV, $\eta_z^{d1} = \eta_z^{f1} = 0.8$, $\eta_z^{d2} = -0.3$, $\eta_z^{f2} = -0.5$, $\epsilon_d - \epsilon_8 = 1.45$ eV, $\eta_7^{f2} = 0.5$, $\eta_7^{f3} = 0.25$, $\eta_{x7}^{f2} = 0.16$, $\eta_z^{v1} = -2.1$, $\eta_z^{v2} = 0.6$, $\eta_7^{v2} = 0.5$.

In Fig. 17,we show an example with $m_{78} = 8\eta_{x7}^{f2} > 0$, corresponding to the physical system (additional examples with $m_{78} = 0$ and $m_{78} < 0$ are shown in Appendix H). We note that in the tight-binding model we can fix the onsite energy difference $\delta \equiv \epsilon_7 - \epsilon_8$, with Δ depending on δ and on the hopping parameters according to Eqs. (A24) and (A26). Figure 17(a) shows the results for the tight-binding model: the gap closes along Γ-X at $\delta = \delta_c$, and a direct $w = -1 \leftrightarrow +1$ transition can be achieved: when $\delta < \delta_c, w = +1$, while when $\delta > \delta_c, w = -1$. Figure 17(b) shows the $\mathbf{k}\cdot\mathbf{p}$ approximation, which captures all the details of the transition, while Fig. 17(c) shows that the $\mathbf{k}\cdot\mathbf{p}$ approximation with four orbitals captures qualitatively the transition, but misses the exact value of δ_c. This shows that the approximation of Sec. IV C is qualitatively correct, but not enough to get accurate quantitative results.

We remark that, when taking into account terms in the Hamiltonian coming from further nearest neighbors, as we

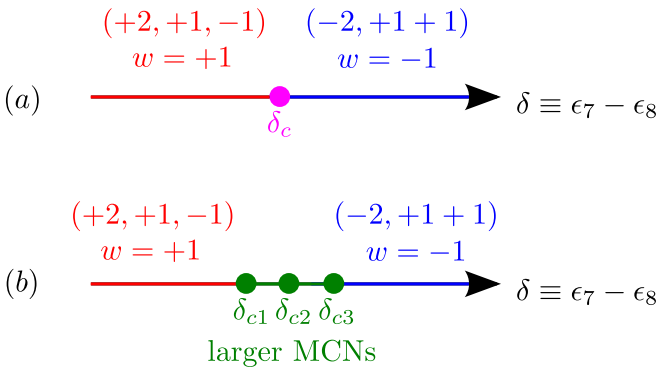

FIG. 18. The $w = -1 \leftrightarrow +1$ transition as a function of the crystal-field splitting δ between the Γ_7 and Γ_8 multiplets can happen directly, as shown in (a), where at $\delta = \delta_c$ the bulk gap closes along Γ-X (see Fig. 17) or via intermediate transitions as shown in (b), where at $\delta = \delta_{c1}, \delta_{c2}, \ldots$ the gap closes along X-Γ, X-M, X-R, or at low-symmetry points giving rise to intermediate phases with larger MCNs.

did in Ref. [31], other phases with larger MCNs can appear between the $w = \pm 1$ phases, with the bulk gap closing at points away from high-symmetry directions. Such transitions change only one MCN at a time: by symmetry considerations, $\mathcal{C}^+_{k_z=0}$ and $\mathcal{C}^+_{k_z=\pi}$ must change by ± 8 and $\mathcal{C}^+_{k_x=k_y}$ by ± 4. As a consequence, transitions like $(-2,+1,+1) \leftrightarrow (-2,+1,-3) \leftrightarrow (+6,+1,-3) \leftrightarrow (+2,+1,-1)$ can be observed, where in the first two cases we have, respectively, $\Delta\mathcal{C}^+_{k_x=k_y} = -4$ and $\Delta\mathcal{C}^+_{k_z=0} = +8$, while the last one corresponds to closing the gap along Γ-X with $\Delta\mathcal{C}^+_{k_z=0} = -4$ and $\Delta\mathcal{C}^+_{k_x=k_y} = +2$; if the order of the first two transitions is inverted, we have $(-2,+1,+1) \leftrightarrow (+6,+1,+1) \leftrightarrow (+6,+1,-3) \leftrightarrow (+2,+1,-1)$. The two kinds of transition, with and without intermediate phases, are shown schematically in Fig. 18. However, the appearance of these intermediate phases is not required, depends on the details of the Hamiltonian, and their range of δ is in any case small.

As shown in Fig. 16(b), with respect to the case in Sec. VII A, the SEV across the transition changes in a different way because Γ_7 states have the opposite SEV given the same mirror-symmetry eigenvalue, so the SEV in the $w = -1$ phase, Fig. 16(b) right, where surface states have mainly Γ_7 character, is reversed with respect to Fig. 16(a) right, where only Γ_8 states are used, while in the $w = +1$ phase, Fig. 16(b) left, surface states have mainly Γ_8 character, and the SEV is as in Fig. 16(a) left. As a consequence, the SEV on the $\bar{\Gamma}$ cone is the same on both sides of the transition, just like the SEV on the $\bar{X}$ cone along the $\bar{X}$-$\bar{\Gamma}$ direction, while the SEV on the $\bar{X}$ cone along the $\bar{X}$-$\bar{M}$ direction is now reversed. We point out that Fig. 16 is qualitative in the sense that things can become more involved very close to a transition: for example, the SEV, even if small, does not reverse exactly at the transition.

We finally recall that the discussion of this section relies on the assumption that Γ_7 and Γ_8 multiplets, when taken alone, give rise to distinct topological phases. This is found to be true in *ab initio* calculations for PuB_6 [30,31], whose band structure is very similar to that of SmB_6. The only *ab initio* data we have for SmB_6 is the $\mathbf{k}\cdot\mathbf{p}$ expansion from Ref. [36]. Using their data, we were not able to confirm the above assumption, with more details given in Appendix I. We note, however, that Ref. [36] predicts a spin structure on the (001) surface corresponding to $w = -1$, in disagreement with experiment [14], casting doubts on the accuracy of the description.

VIII. CONCLUSIONS

In this paper, we have shown how the use of the $\mathbf{k}\cdot\mathbf{p}$ theory for SmB_6 allows to perturbatively compute surface states and their symmetry properties. A central role is played by the parameters v and w constructed from MCNs, $v \equiv \mathrm{sgn}(\mathcal{C}^+_{k_z=0}\mathcal{C}^+_{k_x=k_y})$ and $w \equiv \mathrm{sgn}(\mathcal{C}^+_{k_z=0}\mathcal{C}^+_{k_z=\pi})$, which determine the topological phase of a particular model for SmB_6. We have concrete provided predictions for the spin structure on general surfaces. Given the experimental information [14,21] $w = +1$, we find all cones to have an in-plane winding number $+1$, and on surfaces of low symmetry a small out-of-plane component of the spin is expected.

We have also proposed a simple physical mechanism for inducing topological phase transition. This exploits the fact that different phases $w = \pm 1$ are realized in models which retaining only the Γ_7 or Γ_8 multiplets, such that varying the relative energy of these multiplets will lead to a topological phase transition with a sign change of MCNs and hence of w. Experimentally, this could be in principle achieved by doping the material in such a way that B_6 cages acquire a more negative charge. The topological phase transition is marked by a closing of the bulk gap, and can be observed as a change of the spin structure of surface states. We also stress that the renormalization of parameters due to the Hubbard repulsion could lead to an interaction-induced topological phase transition [44].

Our results are based on a number of assumptions, most importantly the validity of a renormalized single-particle picture and the presence of flat nonreconstructed surfaces. A partial discussion of these issues, focusing on (001) surface states, is in Ref. [39], but it is clear that work beyond single-particle approximations is needed to fully validate our analysis.

We close by noting that our results will not only be important for interpreting results from future photoemission and tunneling experiments, which will be able to probe surface states on arbitrary surfaces of SmB_6 and related materials, but also for understanding the results of *ab initio* DFT calculations: Here, different spin structures have been reported in the DFT literature, but not conclusively assigned to distinct topological phases.

ACKNOWLEDGMENTS

We thank O. Rader, S. Wirth, and M. Legner for illuminating discussions. This research was supported by the DFG through Grants No. SFB 1143 and No. GRK 1621 as well as by the Helmholtz association through Grant No. VI-521.

APPENDIX A: PARAMETERS FOR THE k · p HAMILTONIAN

Parameters of the $\mathbf{k}\cdot\mathbf{p}$ Hamiltonian (23) are defined as follows:

$$\epsilon_d = \langle d^1\uparrow|H|d^1\uparrow\rangle_{000} = \langle d^2\uparrow|H|d^2\uparrow\rangle_{000}, \quad \text{(A1)}$$

$$\epsilon_8 = \langle f^1+|H|f^1+\rangle_{000} = \langle f^2+|H|f^2+\rangle_{000}, \quad \text{(A2)}$$

$$\epsilon_7 = \langle f^7+|H|f^7+\rangle_{000}, \quad \text{(A3)}$$

$$t_d\eta_x^{d1} = \langle d^1\uparrow|H|d^1\uparrow\rangle_{001}, \quad \text{(A4)}$$

$$t_d\eta_z^{d1} = \langle d^2\uparrow|H|d^2\uparrow\rangle_{001}, \quad \text{(A5)}$$

$$t_d\eta_z^{d2} = \langle d^2\uparrow|H|d^2\uparrow\rangle_{110}, \quad \text{(A6)}$$

$$t_f\eta_x^{f1} = \langle f^1+|H|f^1+\rangle_{001}, \quad \text{(A7)}$$

$$t_f\eta_z^{f1} = \langle f^2+|H|f^2+\rangle_{001}, \quad \text{(A8)}$$

$$t_f\eta_z^{f2} = \langle f^2+|H|f^2+\rangle_{110}, \quad \text{(A9)}$$

$$t_f\eta_7^{f1} = \langle f^7+|H|f^7+\rangle_{001}, \quad \text{(A10)}$$

$$t_f\eta_7^{f2} = \langle f^7+|H|f^7+\rangle_{110}, \quad \text{(A11)}$$

$$t_f\eta_7^{f3} = \langle f^7+|H|f^7+\rangle_{111}, \quad \text{(A12)}$$

$$t_f\eta_{78}^{f1} = \langle f^1+|H|f^7+\rangle_{001}, \quad \text{(A13)}$$

$$t_f\eta_{x7}^{f2} = \langle f^1+|H|f^7+\rangle_{110}, \quad \text{(A14)}$$

$$V\eta_x^{v1} = \langle d^1\uparrow|H|f^1+\rangle_{001}, \quad \text{(A15)}$$

$$V\eta_z^{v1} = \langle d^2\uparrow|H|f^2+\rangle_{001}, \quad \text{(A16)}$$

$$V\eta_x^{v2} = \langle d^1\uparrow|H|f^1+\rangle_{110}, \quad \text{(A17)}$$

$$V\eta_z^{v2} = \langle d^2\uparrow|H|f^2+\rangle_{110}, \quad \text{(A18)}$$

$$V\eta_7^{v1} = \langle d^1\uparrow|H|f^7+\rangle_{001}, \quad \text{(A19)}$$

$$V\eta_7^{v2} = \langle d^2\uparrow|H|f^7+\rangle_{110}, \quad \text{(A20)}$$

$$V\eta_{x7}^{v2} = \langle d^1\uparrow|H|f^7+\rangle_{110}, \quad \text{(A21)}$$

where the subscripts 000, 001, 110, or 111 denote the direction along which the matrix element is calculated.

Further quantities appearing in Hamiltonian (23) are the energies

$$\epsilon_1^d = \epsilon_d - t_d\big(3\eta_z^{d1} - \eta_x^{d1} - 6\eta_z^{d2}\big), \quad \text{(A22)}$$

$$\epsilon_2^d = \epsilon_d - t_d\big(3\eta_x^{d1} - \eta_z^{d1} + 2\eta_z^{d2}\big), \quad \text{(A23)}$$

$$\epsilon_1^f = \epsilon_8 - t_f\big(3\eta_z^{f1} - \eta_x^{f1} - 6\eta_z^{f2}\big), \quad \text{(A24)}$$

$$\epsilon_2^f = \epsilon_8 - t_f\big(3\eta_x^{f1} - \eta_z^{f1} + 2\eta_z^{f2}\big), \quad \text{(A25)}$$

$$\epsilon_7^f = \epsilon_7 - t_f\big(2\eta_7^{f1} - 4\eta_7^{f2} - 8\eta_7^{f3}\big), \quad \text{(A26)}$$

the kinetic energy parameters in k_z,

$$g_1^d = \eta_x^{d1} + 3\eta_z^{d2} < 0, \quad \text{(A27)}$$

$$g_2^d = \eta_z^{d1} + \eta_z^{d2} > 0, \quad \text{(A28)}$$

$$g_1^f = \eta_x^{f1} + 3\eta_z^{f2} < 0, \quad \text{(A29)}$$

$$g_2^f = \eta_z^{f1} + \eta_z^{f2} > 0, \quad \text{(A30)}$$

$$g_7^f = \eta_7^{f1} + 4\eta_7^{f2} + 4\eta_7^{f3} < 0, \quad \text{(A31)}$$

and those in $k_\parallel$,

$$l_1^d = \tfrac{1}{4}\big(-\eta_x^{d1} - 3\eta_z^{d1} + 6\eta_z^{d2}\big) < 0, \quad \text{(A32)}$$

$$l_2^d = \tfrac{1}{4}\big(-3\eta_x^{d1} - \eta_z^{d1} - 6\eta_z^{d2}\big) > 0, \quad \text{(A33)}$$

$$l_1^f = \tfrac{1}{4}\big(-\eta_x^{f1} - 3\eta_z^{f1} + 6\eta_z^{f2}\big) < 0, \quad \text{(A34)}$$

$$l_2^f = \tfrac{1}{4}\big(-3\eta_x^{f1} - \eta_z^{f1} - 6\eta_z^{f2}\big) > 0, \quad \text{(A35)}$$

$$l_7^f = -\eta_7^{f1} + 4\eta_7^{f3} < 0. \quad \text{(A36)}$$

Finally, hybridization terms other than the ones quoted in the main text are

$$h_{12}^v = h_{21}^v = \frac{\sqrt{3}}{2}\big(-\eta_x^{v1} + \eta_z^{v1} - 2\eta_x^{v2} + 2\eta_z^{v2}\big), \quad \text{(A37)}$$

$$h_{72}^v = \sqrt{3}\eta_7^{v1} - 2\eta_7^{v2} + 2\sqrt{3}\eta_{x7}^{v2}. \quad \text{(A38)}$$

We note that, when keeping more hybridization terms than the ones used in this work, in general $h_{12}^v \neq h_{21}^v$.

Using values from Ref. [31] we find

$$g_1^d = -0.96, \quad l_1^d = -1.02, \quad \text{(A39)}$$

$$g_2^d = 0.52, \quad l_2^d = 1.20, \quad \text{(A40)}$$

$$g_1^f = -8.00, \quad l_1^f = -6.19, \quad \text{(A41)}$$

$$g_2^f = 1.92, \quad l_2^f = 3.27, \quad \text{(A42)}$$

$$g_7^f = -14.70, \quad l_7^f = -5.14, \quad \text{(A43)}$$

$$f_1^v = 3.91, \quad h_1^v = 5.42, \quad \text{(A44)}$$

$$f_2^v = -4.52, \quad h_2^v = -2.04, \quad \text{(A45)}$$

$$f_7^v = -3.27, \quad h_7^v = 2.44, \quad \text{(A46)}$$

$$h_{12}^v = -0.89, \quad h_{72}^v = -1.79, \quad \text{(A47)}$$

together with $t_d = 1$ eV, $t_f = -0.01$ eV, and $V = 0.1$ eV.

These values mainly serve as approximate guide since they refer to PuB_6. A fully accurate microscopic description in any case requires longer-range tight-binding terms to be precise.

APPENDIX B: DETAILS OF THE CALCULATION AT $\bar{\Gamma}$

Here, we illustrate how to get the doublet of surface states at $\bar{\Gamma}$, following Refs. [28,37]. We start from Eq. (37). In a semi-infinite slab geometry, we want to find surface states at $\bar{\Gamma}$, so we transform $k_z \to -id/dz$, and we pose $\psi_+^n(z) = e^{\lambda z}\psi_+^n(\lambda) = e^{\lambda z}(\alpha_+^n(\lambda),\beta_+^n(\lambda))$, so that

$$H_0^{+(n)}(k_z \to -i\lambda)\psi_+^n(\lambda) = E_+^n(\lambda)\psi_+^n(\lambda), \quad n = 1,2 \tag{B1}$$

together with $\psi(z=0) = \psi(z \to -\infty) = 0$. We can now write

$$(B-\lambda^2)\alpha_+^1 - D_1\lambda\beta_+^1 = 0, \tag{B2}$$

$$D_2\lambda\alpha_+^1 + (C-\lambda^2)\beta_+^1 = 0 \tag{B3}$$

with [we set $E = E_+^1(\lambda)$]

$$B = \frac{\epsilon_1^d - E}{-t_d g_1^d}, \quad C = \frac{\epsilon_1^f - E}{-t_f g_1^f}, \tag{B4}$$

$$D_1 = \frac{Vf_1^v}{-t_d g_1^d}, \quad D_2 = \frac{Vf_1^v}{-t_f g_1^f}, \tag{B5}$$

from which

$$\lambda^4 - \lambda^2(B + C - D_1D_2) + BC = 0, \tag{B6}$$

which determines four solutions $\lambda_i(E)$, $i = 1,2,3,4$, in the form $\pm\sqrt{\Lambda_i}$, $i = 1,2$, where $\lambda^2 = \Lambda$. In order to have surface states we require two solutions λ_1 and λ_2 to have a positive real part. This is equivalent to saying that Λ_i are both real positive, which leads to $\lambda_i = +\sqrt{\Lambda_i}$, or complex conjugate, which leads to λ_1 and λ_2 being complex conjugate, too. So,

$$\psi_+^1(z) = e^{\lambda_1 z}(\alpha_+^{1'},\beta_+^{1'}) + e^{\lambda_2 z}(\alpha_+^{1''},\beta_+^{1''}), \tag{B7}$$

where, imposing the boundary condition at $z = 0$ we get $\alpha_+^{1'} = -\alpha_+^{1''} \equiv \alpha$, $\beta_+^{1'} = -\beta_+^{1''} \equiv \beta$, and

$$\frac{D_2\lambda_1}{C-\lambda_1^2} = \frac{D_2\lambda_2}{C-\lambda_2^2}, \tag{B8}$$

$$\frac{B-\lambda_1^2}{D_1\lambda_1} = \frac{B-\lambda_2^2}{D_1\lambda_2}, \tag{B9}$$

from which $B = C = -\lambda_1\lambda_2 < 0$,

$$E = \frac{\epsilon_1^f t_d g_1^d - \epsilon_1^d t_f g_1^f}{t_d g_1^d - t_f g_1^f}, \tag{B10}$$

$$B = C = \frac{\epsilon_1^f - \epsilon_1^d}{t_d g_1^d - t_f g_1^f}, \tag{B11}$$

and finally, after integrating in dz from $-\infty$ to 0

$$\psi_+^1 = N\left(\frac{1}{\lambda_1} - \frac{1}{\lambda_2}\right)[1, D_2/(\lambda_1+\lambda_2)]$$
$$= N\left(\frac{1}{\lambda_1} - \frac{1}{\lambda_2}\right)[1, -(\lambda_1+\lambda_2)/D_1], \tag{B12}$$

where N is an unimportant normalization factor. We also find that $D_1D_2 = -(\lambda_1+\lambda_2)^2 < 0$, which leads to $B < 0$, $C < 0$, and $D_1D_2 < 0$ as conditions for having surface states.

For $\Gamma_8^{(2)}$ states we note that, while $\epsilon_1^d < \epsilon_1^f$, now $\epsilon_2^d > \epsilon_2^f$, which means that in this subspace no inversion is achieved, and topological surface states are not allowed. Indeed, we observe that the kinetic energy is such that d_{z^2} and $\Gamma_8^{(2)}$ bands never cross along Γ-X, while $d_{x^2-y^2}$ and $\Gamma_8^{(1)}$ do [2,29].

So, surface states at $\bar{\Gamma}$ only exist in the $d_{x^2-y^2}$-$\Gamma_8^{(1)}$ subspace, and we can write after the dz integration

$$|\psi_+\rangle = \alpha|d^1\uparrow\rangle + \beta|f^1+\rangle,$$
$$|\psi_-\rangle = \alpha|d^1\downarrow\rangle - \beta|f^1-\rangle, \tag{B13}$$

which corresponds to Eq. (38); $|\psi_-\rangle$ can be obtained with the same procedure for $H_0^{-(1)}$, or simply as $|\psi_-\rangle = T|\psi_+\rangle$, and

$$\alpha = \sqrt{\frac{t_f g_1^f}{t_f g_1^f - t_d g_1^d}}, \tag{B14}$$

$$\beta = \alpha\frac{Vf_1^v}{-t_f g_1^f(\lambda_1+\lambda_2)} = \alpha\frac{t_d g_1^d(\lambda_1+\lambda_2)}{Vf_1^v}$$
$$= -\operatorname{sgn}\left(Vf_1^v\right)\sqrt{\frac{t_d g_1^d}{t_d g_1^d - t_f g_1^f}}, \tag{B15}$$

where we have used $t_d > 0$, $g_1^d < 0$, or, equivalently, $t_f < 0$, $g_1^f < 0$, and $\lambda_1 + \lambda_2 > 0$ because they are both positive, or complex conjugate with a positive real part. These correspond to Eqs. (39) and (40).

After finding surface states at $k_{x,y} = 0$, we can look at the perturbing Hamiltonian H_P, which is, in the basis $|d_1\uparrow\rangle$, $|d_1\downarrow\rangle, |f_1+\rangle, |f_1-\rangle$,

$$H_P = \begin{pmatrix} -t_d k_\parallel^2 l_1^d & 0 & 0 & -iVh_1^v k_- \\ 0 & -t_d k_\parallel^2 l_1^d & -iVh_1^v k_+ & 0 \\ 0 & iVh_1^v k_- & -t_f k_\parallel^2 l_1^f & 0 \\ iVh_1^v k_+ & 0 & 0 & -t_f k_\parallel^2 l_1^f \end{pmatrix}, \tag{B16}$$

from which we get Eqs. (42)–(44) at the linear order.

When we retain Γ_7 and Γ_8 states, we have

$$H_0^{+(1)} = \begin{pmatrix} \epsilon_1^d - t_d k_z^2 g_1^d & -iVk_z f_1^v & -iVk_z f_7^v \\ iVk_z f_1^v & \epsilon_1^f - t_f k_z^2 g_1^f & m_{78} \\ iVk_z f_7^v & m_{78} & \epsilon_7^f - t_f k_z^2 g_7^f \end{pmatrix}, \tag{B17}$$

which we reduce to Eq. (60) by keeping $|d^1\uparrow\rangle$ and $|f_p^{17}+\rangle$.

APPENDIX C: SPATIAL DEPENDENCE OF SURFACE STATES

We now consider the spatial dependence of surface states. Knowing that $B = C$, Eq. (B11), we can write Eq. (B6) as

$$0 = \lambda^4 - \lambda^2(2B - D_1D_2) + B^2$$
$$= (\lambda^2 - \sqrt{-D_1D_2}\lambda - B)(\lambda^2 + \sqrt{-D_1D_2}\lambda - B) \tag{C1}$$

which reduces to

$$\lambda^2 - \sqrt{-D_1D_2}\lambda - B = 0 \tag{C2}$$

if we require the real part of $\lambda_{1,2}$ to be positive, with solution

$$2\lambda_{1,2} = \sqrt{-D_1 D_2} \pm \sqrt{-D_1 D_2 + 4B} = \sqrt{|D_1 D_2|} \pm \sqrt{|D_1 D_2| - 4|B|}, \quad \text{(C3)}$$

where $\lambda_{1,2}$ can be real or complex conjugate. The spatial part of the wave function is

$$\psi(z) = N(e^{\lambda_1 z} - e^{\lambda_2 z}), \quad \text{(C4)}$$

where we take

$$\int_{-\infty}^{0} \psi^2(z) dz = 1. \quad \text{(C5)}$$

We observe that $\psi(z)$ can always be taken as real; useful integrals are

$$\int_{-\infty}^{0} \psi'(z)\psi(z) dz = 0, \quad \text{(C6)}$$

$$\int_{-\infty}^{0} \psi''(z)\psi(z) dz = -\lambda_1\lambda_2 = B, \quad \text{(C7)}$$

which hold for both real and complex conjugate $\lambda_{1,2}$.

We note that, for a slave-boson-like renormalization $t_f \to b^2 t_f$, $V \to bV$, $b < 1$, $D_1 D_2$ is not affected [see Eq. (B5)], while B only slightly, and in the limit $b^2 t_f \to 0$ it becomes $B = (\epsilon_1^f - \epsilon_1^d)/t_d g_1^d$ [see Eq. (B11)]. If we insert numerical values from Appendix A, and we take $\epsilon_1^f - \epsilon_1^d = 1.6$ eV, corresponding to the minimum of the d band with respect to the Fermi energy, we get $D_1 D_2 = -1.99$, $B = -1.67$. This leads to $\lambda_{1,2} = (0.71 \pm i\,1.08)$, which shows that we are in the regime in which the solutions are complex conjugate, hence, the spatial part of the wave function oscillates, and is

$$\psi_{\bar\Gamma}(z) = 2.01 e^{0.71 z} \sin(1.08 z), \quad \text{(C8)}$$

where z is expressed in units of a_0, the lattice spacing, that we set to 1 everywhere. This holds at $\bar\Gamma$ for a (001) surface.

At $\bar X$, as shown in the main text, we have to substitute $f_1^v \to h_1^v$, $g_1^a \to l_1^a$, $a = d/f$. This leads to the new values of $D_1 D_2 = -4.65$, $B = -1.57$, $\lambda_{1,2} = (1.08 \pm i\,0.64)$, and

$$\psi_{\bar X}(z) = 4.08 e^{1.08 z} \sin(0.64 z). \quad \text{(C9)}$$

If, instead, we use Γ_7 states, at $\bar\Gamma$, $f_1^v \to f_7^v$, $g_1^f \to g_7^f$, we find $D_1 D_2 = -0.76$, $B = -1.67$, $\lambda_{1,2} = (0.43 \pm i\,1.21)$,

$$\psi_{\bar\Gamma}^{\Gamma_7}(z) = 1.40 e^{0.43 z} \sin(1.21 z), \quad \text{(C10)}$$

and at $\bar X$, $f_1^v \to h_7^v$, $g_1^f \to l_7^f$, $D_1 D_2 = -1.14$, $B = -1.57$, $\lambda_{1,2} = (0.53 \pm i\,1.13)$,

$$\psi_{\bar\Gamma}^{\Gamma_7}(z) = 1.61 e^{0.53 z} \sin(1.13 z). \quad \text{(C11)}$$

These are shown in Fig. 19. We notice that in all cases the wave function has a maximum at about $z = -1$, and decays quickly within a few layers. This justifies the argument that a perturbation in the first layer, for example, Kondo breakdown [38] or surface reconstruction [39], should have a significant impact on the wave function and of the dispersion of surface states. However, we stress that the exact z dependence of the wave function does not affect the results of the paper.

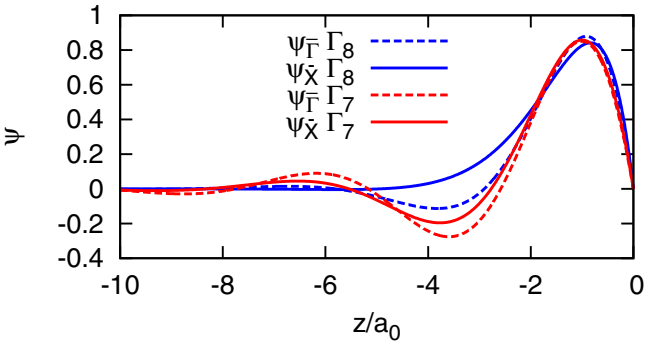

FIG. 19. Spatial part of the wave function $\psi(z)$ at $\bar\Gamma$ and $\bar X$ on a (001) surface, in our approximation with realistic parameters from Ref. [31]; we consider either the Γ_8 or the Γ_7 multiplets.

APPENDIX D: THIRD-ORDER CORRECTIONS TO THE VELOCITIES

We note that our theory is in general not enough to give the exact value of the velocities v_0, v_1, v_2. We can realize this by noting that cubic terms proportional to $k_z^2 k_{x,y}$ in the hybridization, that we have ignored in the main text, will give rise to linear terms in $k_{x,y}$ once $k_z \to -id/dz$, and the same holds for $k_x^2 k_{y,z}$ once $k_x \to -id/dx$. The same will happen for higher powers in the momentum $\mathbf{k}$. These higher-order terms come from next-nearest neighbors (NNs): first-NN terms only give rise to linear terms (for which our theory is exact) and to terms of the form $k_{x,y,z}^{2n+1}$ (which do not create linear correction terms), while second-NN terms to the mentioned mixed cubic terms, and so on. This makes a general treatment quite involved. We can, however, restrict our analysis up to second-NN hybridization, and in particular to terms $\eta_x^{v1}, \eta_z^{v1}, \eta_z^{v2}$, to find

$$f_1^v \to 2\eta_x^{v1} + 6\eta_z^{v2}\left(1 - \frac{k_\parallel^2}{4}\right) \equiv f_1^v + f_1' k_\parallel^2, \quad \text{(D1)}$$

$$h_1^v \to -\frac{1}{2}\eta_x^{v1} - \frac{3}{2}\eta_z^{v1} + 3\eta_z^{v2}\left(1 - \frac{k_z^2}{2}\right) \equiv h_1^v + h_1' k_z^2, \quad \text{(D2)}$$

with $f_1' = h_1' = -3\eta_z^{v2}/2$. These expressions, which come, respectively, from the expansion of $(\cos k_x + \cos k_y)$ and $\cos k_z$ (see Ref. [31]) must be inserted into Eq. (23). Here, we ignore term η_x^{v2} since it introduces an even more complicated momentum dependence in $(k_+^2 - k_-^2)k_+$ for h_1^v, and it is anyway smaller than the other three terms [31]. Now, for the $\bar\Gamma$ cone on the (001) surface, $k_z \to -id/dz$, so we can ignore the quadratic term in $k_\parallel^2$ in f_1^v, while in h_1^v, k_z^2 becomes

$$k_z^2 \to -\frac{d^2}{dz^2} = -B > 0, \quad \text{(D3)}$$

from Eq. (C7), with $B \sim -1$ from Eq. (B11), so we get

$$h_1^v \to -\frac{1}{2}\eta_x^{v1} - \frac{3}{2}\eta_z^{v1} + 3\eta_z^{v2}\left(1 + \frac{B}{2}\right) = h_1^v - h_1' B, \quad \text{(D4)}$$

which must be inserted in Eq. (43) to get the right value of the velocity v_0. For the $\bar X$ cone on the same surface, $k_x \to -id/dx$, so we can ignore the quadratic terms in k_z^2 in h_1^v and

in k_y^2 in f_1^v, while in f_1^v,k_x^2 becomes

$$k_x^2 \to -\frac{d^2}{dz^2} = -B' > 0, \tag{D5}$$

where B' is obtained by B from Eq. (B11) with the usual substitution $g_1^{d,f} \to l_1^{d,f}$. Hence, the value of v_2 Eq. (72)] is unchanged, while for v_1 [Eq. (71)] we have to substitute

$$f_1^v \to 2\eta_x^{v1} + 6\eta_z^{v2}\left(1 + \frac{B'}{4}\right) = f_1^v - f_1' B'. \tag{D6}$$

With these corrections we get the exact values of the velocities, as drawn in Fig. 3; we note that, since $B, B' < 0$, these corrections reduce the value of the velocities, by a factor which can be as large as ~ 2.

For a general surface, things are more complicated. On general grounds, linear terms in H_P proportional to $\bar{k}_{x,y}$ will be of the form $\bar{k}_{x,y} \sum_n c_n \bar{k}_z^n$, with even powers of $\bar{k}_z$ coming from the hybridization, and odd powers from the kinetic energy. Once $\bar{k}_z \to -id/dz$ the $n = 1$ term vanishes from Eq. (C6), but all the other terms survive, and all contribute to the Dirac velocity. In addition, we will have terms $\sum_n d_n \bar{k}_z^n$ which belong to H_0.

These terms come from the same terms we just considered, but, with respect to the (001) surface, we will also have terms coming from higher terms in the expansion of $\sin k_i = \pm(k_i - k_i^3/6 + \ldots)$, $i = x,y,z$, which give rise to linear terms in $\bar{k}_{x,y}$ when rotated. As a consequence, a general theory becomes rather involved, and we stick to the linear order in Figs. 10– 12.

APPENDIX E: NUMERICAL k · p METHOD FOR SLAB GEOMETRY

In Fig. 3, together with the numerical solution of the tight-binding model and the analytical results described in detail in the paper, we also present the numerical solution of the $\mathbf{k} \cdot \mathbf{p}$ Hamiltonian in a slab configuration with N layers for the E_g-Γ_8 basis. Here, we quickly describe this numerical bulk $\mathbf{k} \cdot \mathbf{p}$ calculation, which loosely follows Ref. [36].

Around the $\bar{\Gamma}$ cone, with the usual substitution $k_z \to -id/dz$ in Eq. (23), the operator d/dz now acts on the basis $\psi_n(z) = \sin[\pi n z/(N+1)]$ (up to a normalization factor), where $z = 1, \ldots, N$ is the layer index and $n = 1, \ldots, N$ is a quantum number. The kinetic energy gives a diagonal term $\langle \psi_n | -d^2/dz^2 | \psi_n \rangle = 2 - 2\cos[\pi(n+1)/(N+1)]$, while the hybridization gives nondiagonal terms $\propto \langle \psi_m | d/dz | \psi_n \rangle$ which are evaluated numerically. This grants that the energies at $\bar{\Gamma}$ are exactly the same as those of the tight-binding model. We then take terms in $k_{x,y}$ as a perturbation. We finally numerically diagonalize the resulting Hamiltonian, of size $8N$ ($10N$ if one had to consider Γ_7 states as well), at each momentum close to $\bar{\Gamma}$ to obtain the dispersion. We note that to obtain the exact value of the Dirac velocities we need to retain the third-order terms as described in the previous appendix.

Around the $\bar{X}$ cone, we follow the same method but with $k_x \to -id/dx$, and terms in $k_{y,z}$ as a perturbation.

TABLE II. Definition of the pseudospin in the $\Gamma_8^{(1)}$ basis (above) and in the Γ_7 basis (below).

$(\hat{\sigma}_x, \hat{\sigma}_y, \hat{\sigma}_z)$	$\Gamma_8^{(1)}+$	$\Gamma_8^{(1)}-$
$\Gamma_8^{(1)}+$	$(0,0,-1)$	$(-1,i,0)$
$\Gamma_8^{(1)}-$	$(-1,-i,0)$	$(0,0,1)$
$(\hat{\sigma}_x, \hat{\sigma}_y, \hat{\sigma}_z)$	Γ_7+	Γ_7-
Γ_7+	$(0,0,-1)$	$(-1,i,0)$
Γ_7-	$(-1,-i,0)$	$(0,0,1)$

APPENDIX F: CALCULATION OF THE SEV

To determine the SEV $\langle \vec{\hat{S}} \rangle$ on our basis, we must trace out the orbital degree of freedom; this is trivial in the d shell since states are a direct product of a spin and an orbital part, which is no more true in the f shell, due to the spin-obit coupling. In this latter case we obtain the results of Table III [31]. In Table II, we report our definition of the pseudospin $\vec{\hat{\sigma}}$. The same can be done for the angular momentum $\langle \vec{\hat{L}} \rangle$: for d states it is completely quenched since we only take the E_g multiplet; while for f states we obtain that its expectation value is -8 times the SEV. This is true in any basis, for example, for $j = \frac{5}{2}$, $j_z = -\frac{5}{2}, \ldots, \frac{5}{2}$ states:

$$|j_z\rangle = \sqrt{\frac{1}{2} - \frac{j_z}{7}} \left| j_z - \frac{1}{2}, \uparrow \right\rangle - \sqrt{\frac{1}{2} + \frac{j_z}{7}} \left| j_z + \frac{1}{2}, \downarrow \right\rangle \tag{F1}$$

we find

$$\langle j_z | \hat{L}_z | j_z \rangle = \frac{8}{7} j_z, \quad \langle j_z | \hat{S}_z | j_z \rangle = -\frac{1}{7} j_z, \tag{F2}$$

and similar (matrix) relations hold for $\hat{L}_x, \hat{S}_x$ and $\hat{L}_y, \hat{S}_y$ (one can build a matrix like the one in Table III substituting $\vec{\hat{S}}$ with $\vec{\hat{L}}$ and multiplying all entries by -8).

As a consequence, for d states we find the following rules:

$$\langle \vec{\hat{L}}^d \rangle = 0, \tag{F3}$$

$$\langle \vec{\hat{J}}^d \rangle = \langle \vec{\hat{L}}^d \rangle + \langle \vec{\hat{S}}^d \rangle = \langle \vec{\hat{S}}^d \rangle, \tag{F4}$$

$$\langle \vec{\hat{L}}^d + 2\vec{\hat{S}}^d \rangle = 2\langle \vec{\hat{S}}^d \rangle, \tag{F5}$$

while for f states

$$\langle \vec{\hat{L}}^f \rangle = -8\langle \vec{\hat{S}}^f \rangle, \tag{F6}$$

$$\langle \vec{\hat{J}}^f \rangle = -7\langle \vec{\hat{S}}^f \rangle, \tag{F7}$$

$$\langle \vec{\hat{L}}^f + 2\vec{\hat{S}}^f \rangle = -6\langle \vec{\hat{S}}^f \rangle. \tag{F8}$$

For a generic state with α^2 weight on d states, and β^2 weight on f states ($\alpha^2 + \beta^2 = 1$):

$$\langle \vec{\hat{S}} \rangle = \langle \vec{\hat{S}}^d \rangle \alpha^2 + \langle \vec{\hat{S}}^f \rangle \beta^2, \tag{F9}$$

$$\langle \vec{\hat{L}} \rangle = -8\langle \vec{\hat{S}}^f \rangle \beta^2, \tag{F10}$$

$$\langle \vec{\hat{J}} \rangle = 2\langle \vec{\hat{S}}^d \rangle \alpha^2 - 7\langle \vec{\hat{S}}^f \rangle \beta^2, \tag{F11}$$

TABLE III. Expectation value of the spin in the Γ_7-Γ_8 basis.

$2(\hat{S}^x,\hat{S}^y,\hat{S}^z)$	$\Gamma_8^{(1)}+$	$\Gamma_8^{(1)}-$	$\Gamma_8^{(2)}+$	$\Gamma_8^{(2)}-$	Γ_7+	Γ_7-
$\Gamma_8^{(1)}+$	$\frac{11}{21}(0,0,-1)$	$\frac{5}{21}(-1,i,0)$	$(0,0,0)$	$\frac{2\sqrt{3}}{21}(-1,-i,0)$	$\frac{4\sqrt{5}}{21}(0,0-1)$	$\frac{2\sqrt{5}}{21}(1,-i,0)$
$\Gamma_8^{(1)}-$	$\frac{5}{21}(-1,-i,0)$	$\frac{11}{21}(0,0,1)$	$\frac{2\sqrt{3}}{21}(-1,i,0)$	$(0,0,0)$	$\frac{2\sqrt{5}}{21}(1,i,0)$	$\frac{4\sqrt{5}}{21}(0,0,1)$
$\Gamma_8^{(2)}+$	$(0,0,0)$	$\frac{2\sqrt{3}}{21}(-1,-i,0)$	$\frac{1}{7}(0,0,-1)$	$\frac{3}{7}(-1,i,0)$	$(0,0,0)$	$\frac{2\sqrt{15}}{21}(1,i,0)$
$\Gamma_8^{(2)}-$	$\frac{2\sqrt{3}}{21}(-1,i,0)$	$(0,0,0)$	$\frac{3}{7}(-1,-i,0)$	$\frac{1}{7}(0,0,1)$	$\frac{2\sqrt{15}}{21}(1,-i,0)$	$(0,0,0)$
Γ_7+	$\frac{4\sqrt{5}}{21}(0,0,-1)$	$\frac{2\sqrt{5}}{21}(1,-i,0)$	$(0,0,0)$	$\frac{2\sqrt{15}}{21}(1,i,0)$	$\frac{5}{21}(0,0,1)$	$\frac{5}{21}(1,-i,0)$
Γ_7-	$\frac{2\sqrt{5}}{21}(1,i,0)$	$\frac{4\sqrt{5}}{21}(0,0,1)$	$\frac{2\sqrt{15}}{21}(1,-i,0)$	$(0,0,0)$	$\frac{5}{21}(1,i,0)$	$\frac{5}{21}(0,0,-1)$

$$\langle\vec{\hat{L}}+2\vec{\hat{S}}\rangle = 2\langle\vec{\hat{S}}^d\rangle\alpha^2 - 6\langle\vec{\hat{S}}^f\rangle\beta^2, \tag{F12}$$

which shows that the expectation value of operator $\vec{\hat{L}}+2\vec{\hat{S}}$ must be comprised between $-6\langle\vec{\hat{S}}\rangle$ (pure f states) and $2\langle\vec{\hat{S}}\rangle$ (pure d states).

In Ref. [36], these quantities were computed for surface states using an *ab initio* approach; for in-plane components authors find on the $\bar{\Gamma}$ cone

$$\langle\hat{L}^{\bar{\Gamma}}_{x,y}+2\hat{S}^{\bar{\Gamma}}_{x,y}\rangle = -5.98\langle\hat{S}^{\bar{\Gamma}}_{x,y}\rangle, \tag{F13}$$

which is in excellent agreement with our results for f states, and the small difference is likely due to d weight on surface states; on the $\bar{X}$ cone,

$$\langle\hat{L}^{\bar{X}}_{x}+2\hat{S}^{\bar{X}}_{x}\rangle = -5.11\langle\hat{S}^{\bar{X}}_{x}\rangle, \tag{F14}$$

$$\langle\hat{L}^{\bar{X}}_{y}+2\hat{S}^{\bar{X}}_{y}\rangle = -5.43\langle\hat{S}^{\bar{X}}_{y}\rangle, \tag{F15}$$

where the larger disagreement with f state results can be interpreted as a larger d weight on surface states, or as the influence of the $j=\frac{7}{2}$ multiplet, for which spin and angular momentum are parallel instead of antiparallel. For the out-of-plane component, things are similar on the $\bar{X}$ cone

$$\langle\hat{L}^{\bar{X}}_{z}+2\hat{S}^{\bar{X}}_{z}\rangle = -5.27\langle\hat{S}^{\bar{X}}_{z}\rangle, \tag{F16}$$

but the disagreement is larger on the $\bar{\Gamma}$ cone

$$\langle\hat{L}^{\bar{\Gamma}}_{z}+2\hat{S}^{\bar{\Gamma}}_{z}\rangle = -7.47\langle\hat{S}^{\bar{\Gamma}}_{z}\rangle, \tag{F17}$$

and cannot be explained by our theory, probably due to the small basis used. We recall that all calculations involve single-particle states, hence do not include many-particles effects.

APPENDIX G: SURFACE STATES FOR A GENERIC SURFACE

In this appendix, we give details about the effective Hamiltonian for a generic surface.

1. Rotations

Given the (lm/n) triplet and angles θ and ϕ from Eqs. (89) and (90), we can perform a rotation in momentum space with Euler angles $\omega,\omega'=\theta,\omega''=\phi$ to obtain ($c_\theta\equiv\cos\theta$, $s_\theta\equiv\sin\theta$ and similar for ω and ϕ)

$$\begin{aligned}
\bar{k}_x &= (c_\omega c_\theta c_\phi - s_\omega s_\phi)k_x + (c_\omega c_\theta s_\phi + s_\omega c_\phi)k_y - c_\omega s_\theta k_z,\\
\bar{k}_y &= -(c_\omega s_\phi + s_\omega c_\theta c_\phi)k_x + (c_\omega c_\phi - s_\omega c_\theta s_\phi)k_y + s_\omega s_\theta k_z,\\
\bar{k}_z &= s_\theta c_\phi k_x + s_\theta s_\phi k_y + c_\theta k_z,
\end{aligned} \tag{G1}$$

which can be inverted to give

$$\begin{aligned}
k_x &= (c_\omega c_\theta c_\phi - s_\omega s_\phi)\bar{k}_x - (c_\omega s_\phi + s_\omega c_\theta c_\phi)\bar{k}_y + s_\theta c_\phi \bar{k}_z,\\
k_y &= (c_\omega c_\theta s_\phi + s_\omega c_\phi)\bar{k}_x + (c_\omega c_\phi - s_\omega c_\theta s_\phi)\bar{k}_y + s_\theta s_\phi \bar{k}_z,\\
k_z &= -c_\omega s_\theta \bar{k}_x + s_\omega s_\theta \bar{k}_y + c_\theta \bar{k}_z.
\end{aligned} \tag{G2}$$

In the main text, we take take $\omega=0$ to get

$$\begin{aligned}
\bar{k}_x &= k_x\cos\theta\cos\phi + k_y\cos\theta\sin\phi - k_z\sin\theta,\\
\bar{k}_y &= -k_x\sin\phi + k_y\cos\phi,\\
\bar{k}_z &= k_x\sin\theta\cos\phi + k_y\sin\theta\sin\phi + k_z\cos\theta
\end{aligned} \tag{G3}$$

and

$$\begin{aligned}
k_x &= \bar{k}_x\cos\theta\cos\phi - \bar{k}_y\sin\phi + \bar{k}_z\sin\theta\cos\phi,\\
k_y &= \bar{k}_x\cos\theta\sin\phi + \bar{k}_y\cos\phi + \bar{k}_z\sin\theta\sin\phi,\\
k_z &= -\bar{k}_x\sin\theta + \bar{k}_z\cos\theta.
\end{aligned} \tag{G4}$$

This shows that the $X=(0,0,\pi)$ point is projected at

$$\bar{\mathbf{k}}_X = (-\pi\sin\theta, 0) \tag{G5}$$

[see Eq. (G5)], so $\bar{k}_x$ is the direction which joins $\bar{\Gamma}$ to the position of the cone, unless $\theta=0$, which corresponds to the $\bar{\Gamma}$ cone on the (001) surface, for which $\bar{k}_x$ and $\bar{k}_y$ directions are equivalent. We can also notice from Eq. (G3) that $X'=(\pi,0,0)$ and $X''=(0,\pi,0)$ are projected, respectively, to

$$\bar{\mathbf{k}}_{X'} = \pi(\cos\theta\cos\phi, -\sin\phi), \tag{G6}$$

$$\bar{\mathbf{k}}_{X''} = \pi(\cos\theta\sin\phi, \cos\phi) \tag{G7}$$

[see Eqs. (92) and (93)], which are the positions of the two other Dirac cones in the BZ when $\omega=0$.

However, we do not want to describe these two other cones by projecting X' and X'', but, instead, always projecting X since this allows to safely neglect subspace 2. As a consequence, we now require X to be projected at $\bar{\mathbf{k}}_{X'}$ with angles ω',θ',ϕ', and at $\bar{\mathbf{k}}_{X''}$ with angles ω'',θ'',ϕ''; from Eq. (G1) we find that, when $\omega\neq 0, X$ is projected at

$\pi(-\cos\omega\sin\theta, \sin\omega\sin\theta)$. So, for $\bar{\mathbf{k}}_{X'}$ we get

$$-\cos\omega'\sin\theta' = \cos\theta\cos\phi,$$
$$\sin\omega'\sin\theta' = -\sin\phi, \tag{G8}$$

which gives

$$\tan^2\omega' = \tan^2\phi(\tan^2\theta+1) = \frac{m^2(l^2+m^2+n^2)}{l^2n^2}, \tag{G9}$$

$$\tan^2\theta' = \tan^2\phi\cot^2\theta + \tan^2\phi + \cot^2\theta = \frac{m^2+n^2}{l^2} \tag{G10}$$

with $-\pi \leqslant \omega' \leqslant -\pi/2$, $0 \leqslant \theta' \leqslant \pi/2$. Using our notation, this corresponds to a (mn/l) triplet.

For $\bar{\mathbf{k}}_{X''}$ we get

$$-\cos\omega''\sin\theta'' = \cos\theta\sin\phi, \tag{G11}$$

$$\sin\omega''\sin\theta'' = \cos\phi, \tag{G12}$$

which gives

$$\tan^2\omega'' = \cot^2\phi(\tan^2\theta+1) = \frac{l^2(l^2+m^2+n^2)}{m^2n^2},$$
$$\tan^2\theta'' = \cot^2\phi\cot^2\theta + \cot^2\phi + \cot^2\theta = \frac{n^2+l^2}{m^2} \tag{G13}$$

with $\pi/2 \leqslant \omega'' \leqslant \pi$, $0 \leqslant \theta'' \leqslant \pi/2$. This corresponds to a (nl/m) triplet. This means that we can then apply the theory of the following subsection using θ to get the effective Hamiltonian at $\bar{\mathbf{k}}_X$, θ' for $\bar{\mathbf{k}}_{X'}$ and θ'' for $\bar{\mathbf{k}}_{X''}$.

Angles $\omega = 0$, ω', and ω'' tell how we have to rotate our system in the surface plane to get the same coordinate system for all cones. If we ignore this, every cone will have its own coordinates, with $\bar{k}_x$ joining the position of the cone to the center of the BZ.

2. Details of the calculation

In this section, we find the effective surface Hamiltonian for a given (lm/n) triplet; this Hamiltonian is valid for small momenta around the surface point $\bar{\mathbf{k}}_X$ on which the bulk $X = (0,0,\pi)$ point is projected. We concentrate on subspace 1, so ignoring any coupling to subspace 2, and use only Γ_8 states, so the bulk $\mathbf{k}\cdot\mathbf{p}$ Hamiltonian is 4×4, and in the $|d^1\uparrow\rangle, |d^1\downarrow\rangle, |f^1+\rangle, |f^1-\rangle$ basis reads as

$$H = \begin{pmatrix} \epsilon_1^d(\mathbf{k})\sigma_0 & -iVH_h \\ iVH_h^\dagger & \epsilon_1^f(\mathbf{k})\sigma_0 \end{pmatrix}, \tag{G14}$$

$$H_h = h_1^v(k_x\sigma_x + k_y\sigma_y) + f_1^v k_z\sigma_z. \tag{G15}$$

When we perform the rotation from $\mathbf{k}$ to $\bar{\mathbf{k}}$ the kinetic energy becomes

$$\epsilon_1^a[\mathbf{k}(\bar{\mathbf{k}})] = \epsilon_1^a - t_a\left[g_1^a k_z^2(\bar{\mathbf{k}}) + l_1^a k_\parallel^2(\bar{\mathbf{k}})\right], \quad a = d/f \tag{G16}$$

and the hybridization

$$H_h = h_1^v[k_x(\bar{\mathbf{k}})\sigma_x + k_y(\bar{\mathbf{k}})\sigma_y] + f_1^v k_z(\bar{\mathbf{k}})\sigma_z, \tag{G17}$$

where one has to express $\mathbf{k}$ as a function of $\bar{\mathbf{k}}$.

When we use Eq. (G4), for the kinetic energy we find

$$\epsilon_1^a[\mathbf{k}(\bar{\mathbf{k}})] = \epsilon_1^a - t_a\{g_1^a(\bar{k}_x\sin\theta - \bar{k}_z\cos\theta)^2 + l_1^a[\bar{k}_y^2 + (\bar{k}_x\cos\theta + \bar{k}_z\sin\theta)^2]\}. \tag{G18}$$

Upon substitution of Eqs. (G4) into Eq. (G17), we see that the hybridization term in $\bar{k}_z$ contains terms in σ_x, σ_y, and σ_z. However, we would like it to be proportional just to σ_z, so that we can follow what we did in Appendix B. We see that this is achieved if we perform a Wigner transformation in the pseudospin space with angles $\omega, \omega_1' = \arctan[\tan\theta(h_1^v/f_1^v)], \omega'' = \phi$; we will denote this transformation matrix as U. This corresponds to the same rotation that we did in the momentum space, except for angle ω_1', which now depends on f_1^v and h_1^v, and that we take between 0 and π. The total rotation matrix is

$$U_t = \begin{pmatrix} U & 0 \\ 0 & U \end{pmatrix}, \tag{G19}$$

with

$$U = \begin{pmatrix} e^{i\phi/2}\cos(\omega_1'/2) & e^{-i\phi/2}\sin(\omega_1'/2) \\ -e^{i\phi/2}\sin(\omega_1'/2) & e^{-i\phi/2}\cos(\omega_1'/2) \end{pmatrix}. \tag{G20}$$

In the new basis, the hybridization (G17) takes the simpler form

$$H_h = \left(\bar{h}_{1xx}^v\sigma_x + \bar{h}_{1xz}^v\sigma_z\right)\bar{k}_x + h_1^v\sigma_y\bar{k}_y + \bar{f}_1^v\sigma_z\bar{k}_z \tag{G21}$$

with

$$\bar{h}_{1xx}^v = \frac{f_1^v|h_1^v|}{\sqrt{\left(f_1^v\right)^2\cos^2\theta + \left(h_1^v\right)^2\sin^2\theta}}, \tag{G22}$$

$$\bar{h}_{1xz}^v = \frac{\left[\left(h_1^v\right)^2 - \left(f_1^v\right)^2\right]\sin\theta\cos\theta}{\sqrt{\left(f_1^v\right)^2\cos^2\theta + \left(h_1^v\right)^2\sin^2\theta}}\,\mathrm{sgn}\left(h_1^v\right), \tag{G23}$$

$$\bar{f}_1^v = \sqrt{\left(f_1^v\right)^2\cos^2\theta + \left(h_1^v\right)^2\sin^2\theta}\,\mathrm{sgn}\left(h_1^v\right) \tag{G24}$$

[see Eq. (98)], while the kinetic energy, being the identity in the (pseudo)spin index, is left unchanged. In this way, when we set $\bar{k}_x = \bar{k}_y = 0$, the only hybridization term left is in σ_z, the Hamiltonian H_0 splits into two 2×2 blocks, and we can repeat the treatment of Appendix B.

In the kinetic energy part (G18), we obtain that the terms multiplying $\bar{k}_z^2$ are

$$\bar{g}_1^a = g_1^a\cos^2\theta + l_1^a\sin^2\theta < 0, \quad a = d/f \tag{G25}$$

[see Eq. (97)], and the only information we needed is that they are both negative, $\bar{g}_1^a < 0$, since $g_1^a<0, l_1^a<0$ (see Appendix B).

With the substitutions $g_1^a \to \bar{g}_1^a, f_1^v \to \bar{f}_1^v$, the basis at $\bar{k}_\parallel = 0$ is

$$|\bar{\psi}_+\rangle = \alpha|\bar{d}^1\uparrow\rangle + \beta|\bar{f}^1+\rangle,$$
$$|\bar{\psi}_-\rangle = \alpha|\bar{d}^1\downarrow\rangle - \beta|\bar{f}^1-\rangle, \tag{G26}$$

with $|\bar{d}\rangle = U|d\rangle$, $|\bar{f}\rangle = U|f\rangle$. The effective Hamiltonian up to the linear term in $\bar{\mathbf{k}}_\parallel$ [Eq. (94)] is

$$H_\theta^{\mathrm{eff}} = -2\alpha\beta V h_1^v\left(\frac{f_1^v}{\bar{f}_1^v}\bar{k}_x\hat{s}_y - \bar{k}_y\hat{s}_x\right) \equiv v_1\bar{k}_x\hat{s}_y - v_2\bar{k}_y\hat{s}_x = |v_1|w\bar{k}_x\hat{s}_y - |v_2|\bar{k}_y\hat{s}_x \tag{G27}$$

[see Eq. (94)].

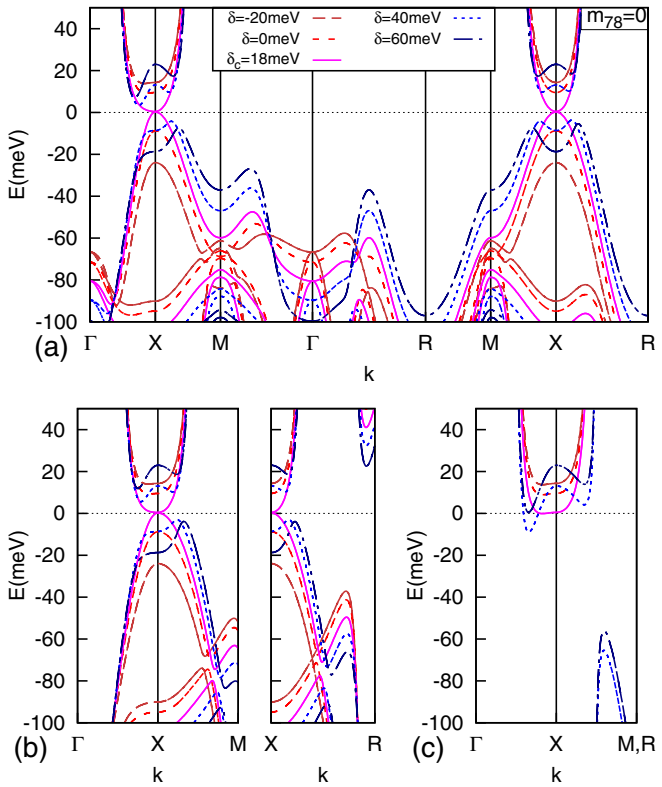

FIG. 20. Same as Fig. 17 but with $\eta_{x7}^{f2} = 0$, i.e., without any direct coupling between the Γ_7 and Γ_8 subspaces, which leads to $m_{78} = 0$ in the $\mathbf{k} \cdot \mathbf{p}$ Hamiltonian. In this case, the gap closes at X.

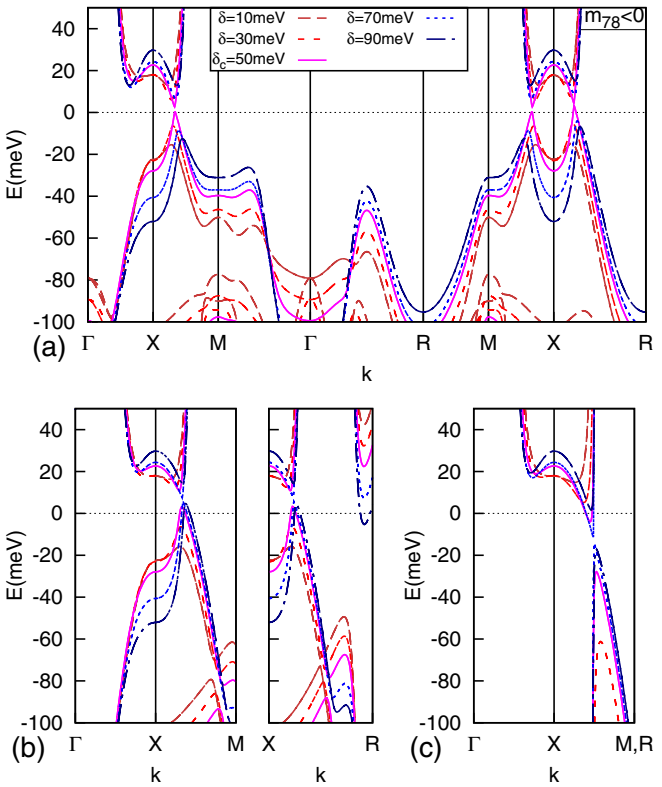

FIG. 21. Same as Fig. 17 but with $\eta_{x7}^{f2} = -0.16$, which leads to $m_{78} < 0$ in the $\mathbf{k} \cdot \mathbf{p}$ Hamiltonian. In this case, the gap closes along X-M and X-R approximatively at the same energy, which is slightly inaccurate in the $\mathbf{k} \cdot \mathbf{p}$ method.

There is now an additional term coming from $\bar{k}_z \bar{k}_x$ of the kinetic energy (G18): however, with the substitution $\bar{k}_z \to -id/dz$, it gives rise to an integral of the form $\int_{-\infty}^{0} \psi(z)\psi'(z)dz \propto \psi^2(0) - \psi^2(-\infty) = 0$ [see Eq. (C6)].

APPENDIX H: FURTHER TOPOLOGICAL PHASE TRANSITIONS

In Figs. 20 and 21, we present the analogousness of Fig. 17 but with $m_{78} = 0$, and $m_{78} < 0$. It can be observed that this parameter controls where the gap closes, i.e., along X-Γ for $m_{78} > 0$, along X-R and X-M for $m_{78} < 0$, and at X for $m_{78} = 0$.

APPENDIX I: REMARKS ON DFT RESULTS

As noted in the main text, the available *ab initio* results do not appear fully consistent regarding the question of whether the Γ_7 and Γ_8 multiplets, when taken alone, yield distinct topological phases. If true, varying the relative multiplet energy drives a topological transition as discussed in Sec. VII B.

While this applies to the *ab* initio results obtained for PuB_6 [30,31], the *ab* initio based $\mathbf{k} \cdot \mathbf{p}$ expansion for SmB_6 from Ref. [36] appears problematic. We have analyzed their results, and upon varying the relative multiplet energy we do *not* find topological phase transition. This is what we expect when both multiplets, taken alone, realize the same topological phase, i.e., $\mathrm{sgn}(f_1^v h_1^v) = \mathrm{sgn}(f_7^v h_7^v)$, and m_{78} is such that w from Eq. (62) never vanishes (if m_{78} has the opposite sign, a double transition $w = \pm 1 \leftrightarrow w = \mp 1 \leftrightarrow w = \pm 1$ could be in principle achieved). Which phase is exactly realized depends on the exact knowledge of the basis used in Ref. [36] (including phase factors); based on the reported spin structure (which disagrees with experiment [14]) we guess it is the $w = -1$ phase.

Possible explanations are that hybridization terms in SmB_6 and PuB_6 are so different as to place the two materials into two different topological phases when considering just one or both multiplets; or that in particular cases the $\mathbf{k} \cdot \mathbf{p}$ expansion is not good enough to describe the topological phase transition, for example, because more terms must be kept in the small-momentum expansion. It also possible that a particular choice of complex phases of the basis states has led us to wrong conclusions about that work.

For completeness, we quote numerical values which we extracted from Ref. [36]: $|f_1^v| = |c_2 \cos\phi + c_3 \sin\phi|/2\pi V = 0.79$, $|h_1^v| = |c_1 \cos\phi + c_4 \sin\phi|/2\pi V = 0.73$, $|f_7^v| = |-c_2 \sin\phi + c_3 \cos\phi|/2\pi V = 0.52$, $|h_7^v| = |-c_1 \sin\phi + c_4 \cos\phi|/2\pi V = 0.56$ ($\cos\phi = \sqrt{5/6}$, $\sin\phi = \sqrt{1/6}$, c_i's are given numerically there), when measured in units $V = 0.1$ eV. These are about one order of magnitude smaller than our values for PuB_6 given in Appendix A [Eqs. (A43) and (A45)]. This difference in the absolute value is most likely due to the renormalization by the Gutzwiller method and the fact that PuB_6 has a larger f kinetic energy than SmB_6, hence is likely to have also a larger

hybridization. However, we stress that absolute values do *not* affect the spin structure. The latter instead hinges on signs, and this is where the above numbers would require a crosscheck.

[1] T. Takimoto, J. Phys. Soc. Jpn. **80**, 123710 (2011).
[2] F. Lu, J. Z. Zhao, H. Weng, Z. Fang, and X. Dai, Phys. Rev. Lett. **110**, 096401 (2013).
[3] V. Alexandrov, M. Dzero, and P. Coleman, Phys. Rev. Lett. **111**, 226403 (2013).
[4] M. Dzero, K. Sun, V. Galitski, and P. Coleman, Phys. Rev. Lett. **104**, 106408 (2010).
[5] S. Wolgast, C. Kurdak, K. Sun, J. W. Allen, D.-J. Kim, and Z. Fisk, Phys. Rev. B **88**, 180405(R) (2013).
[6] D. J. Kim, J. Xia, and Z. Fisk, Nat. Mater. **13**, 466 (2014).
[7] X. Zhang, N. P. Butch, P. Syers, S. Ziemak, R. L. Greene, and J. Paglione, Phys. Rev. X **3**, 011011 (2013).
[8] Y. Nakajima, P. Syers, X. Wang, R. Wang, and J. Paglione, Nat. Phys. **12**, 213 (2015).
[9] M. Neupane, N. Alidoust, S. Xu, T. Kondo, Y. Ishida, D.-J. Kim, C. Liu, I. Belopolski, Y. Jo, T.-R. Chang, H.-T. Jeng, T. Durakiewicz, L. Balicas, H. Lin, A. Bansil, S. Shin, Z. Fisk, and M. Z. Hasan, Nat. Commun. **4**, 2991 (2013).
[10] N. Xu, X. Shi, P. K. Biswas, C. E. Matt, R. S. Dhaka, Y. Huang, N. C. Plumb, M. Radovic, J. H. Dil, E. Pomjakushina, K. Conder, A. Amato, Z. Salman, D. M. Paul, J. Mesot, H. Ding, and M. Shi, Phys. Rev. B **88**, 121102 (2013).
[11] J. Jiang, S. Li, T. Zhang, Z. Sun, F. Chen, Z. R. Ye, M. Xu, Q. Q. Ge, S. Y. Tan, X. H. Niu, M. Xia, B. P. Xie, Y. F. Li, X. H. Chen, H. H. Wen, and D. L. Feng, Nat. Commun. **4**, 3010 (2013).
[12] C.-H. Min, P. Lutz, S. Fiedler, B. Y. Kang, B. K. Cho, H.-D. Kim, H. Bentmann, and F. Reinert, Phys. Rev. Lett. **112**, 226402 (2014).
[13] J. D. Denlinger, J. W. Allen, J.-S. Kang, K. Sun, B.-I. Min, D.-J. Kim, and Z. Fisk, arXiv:1312.6636.
[14] N. Xu, P. K. Biswas, J. H. Dil, R. S. Dhaka, G. Landolt, S. Muff, C. E. Matt, X. Shi, N. C. Plumb, M. Radović, E. Pomjakushina, K. Conder, A. Amato, S. Borisenko, R. Yu, H.-M. Weng, Z. Fang, X. Dai, J. Mesot, H. Ding, and M. Shi, Nat. Commun. **5**, 4566 (2014).
[15] Z.-H. Zhu, A. Nicolaou, G. Levy, N. P. Butch, P. Syers, X. F. Wang, J. Paglione, G. A. Sawatzky, I. S. Elfimov, and A. Damascelli, Phys. Rev. Lett. **111**, 216402 (2013).
[16] E. Frantzeskakis, N. de Jong, B. Zwartsenberg, Y. K. Huang, Y. Pan, X. Zhang, J. X. Zhang, F. X. Zhang, L. H. Bao, O. Tegus, A. Varykhalov, A. de Visser, and M. S. Golden, Phys. Rev. X **3**, 041024 (2013).
[17] P. Hlawenka, K. Siemensmeyer, E. Weschke, A. Varykhalova, J. Sánchez-Barriga, N. Y. Shitsevalova, A. V. Dukhnenko, V. B. Filipov, S. Gabáni, K. Flachbart, O. Rader, and E. D. L. Rienks, arXiv:1502.01542.
[18] B. S. Tan, Y.-T. Hsu, B. Zeng, M. Ciomaga Hatnean, N. Harrison, Z. Zhu, M. Hartstein, M. Kiourlappou, A. Srivastava, M. D. Johannes, T. P. Murphy, J.-H. Park, L. Balicas, G. G. Lonzarich, G. Balakrishnan, and S. E. Sebastian, Science **349**, 287 (2015).
[19] M. Ye, J. W. Allen, and K. Sun, arXiv:1307.7191.
[20] L. Fu, Phys. Rev. Lett. **106**, 106802 (2011).
[21] P. P. Baruselli and M. Vojta, Phys. Rev. Lett. **115**, 156404 (2015).
[22] M. Legner, A. Rüegg, and M. Sigrist, Phys. Rev. Lett. **115**, 156405 (2015).
[23] P. G. Silvestrov, P. W. Brouwer, and E. G. Mishchenko, Phys. Rev. B **86**, 075302 (2012).
[24] F. Chen, C. Shang, Z. Jin, D. Zhao, Y. P. Wu, Z. J. Xiang, Z. C. Xia, A. F. Wang, X. G. Luo, T. Wu, and X. H. Chen, Phys. Rev. B **91**, 205133 (2015).
[25] S. Roessler, L. Jiao, D.-J. Kim, S. Seiro, K. Rasim, F. Steglich, L. H. Tjeng, Z. Fisk, and S. Wirth, arXiv:1512.07072.
[26] J. D. Denlinger, S. Jang, G. Li, L. Chen, B. J. Lawson, T. Asaba, C. Tinsman, F. Yu, K. Sun, J. W. Allen, C. Kurdak, D.-J. Kim, Z. Fisk, and L. Li, arXiv:1601.07408.
[27] B. Roy, J. Hofmann, V. Stanev, J. D. Sau, and V. Galitski, Phys. Rev. B **92**, 245431 (2015).
[28] C.-X. Liu, X.-L. Qi, H. J. Zhang, X. Dai, Z. Fang, and S.-C. Zhang, Phys. Rev. B **82**, 045122 (2010).
[29] C.-J. Kang, J. Kim, K. Kim, J. Kang, J. D. Denlinger, and B. I. Min, J. Phys. Soc. Jpn. **84**, 024722 (2015).
[30] X. Deng, K. Haule, and G. Kotliar, Phys. Rev. Lett. **111**, 176404 (2013).
[31] P. P. Baruselli and M. Vojta, Phys. Rev. B **90**, 201106 (2014).
[32] J. C. Y. Teo, L. Fu, and C. L. Kane, Phys. Rev. B **78**, 045426 (2008).
[33] A. C. Hewson, *The Kondo Problem to Heavy Fermions* (Cambridge University Press, Cambridge, 1993).
[34] M. Hohenadler and F. F. Assaad, J. Phys.: Condens. Matter **25**, 143201 (2013).
[35] J. Kim, K. Kim, C.-J. Kang, S. Kim, H. C. Choi, J.-S. Kang, J. D. Denlinger, and B. I. Min, Phys. Rev. B **90**, 075131 (2014).
[36] R. Yu, H. Weng, X. Hu, Z. Fang, and X. Dai, New J. Phys. **17**, 023012 (2015).
[37] B. Roy, J. D. Sau, M. Dzero, and V. Galitski, Phys. Rev. B **90**, 155314 (2014).
[38] V. Alexandrov, P. Coleman, and O. Erten, Phys. Rev. Lett. **114**, 177202 (2015).
[39] P. P. Baruselli and M. Vojta, 2D Mater. **2**, 044011 (2015).
[40] R. Peters, Y. Tsuneya, S. Hirofumi, and N. Kawakami, arXiv:1510.06476.
[41] S. Rößler, T.-H. Jang, D.-J. Kim, L. H. Tjeng, Z. Fisk, F. Steglich, and S. Wirth, Proc. Natl. Acad. Sci. USA **111**, 4798 (2014).
[42] M. M. Yee, Y. He, A. Soumyanarayanan, D.-J. Kim, Z. Fisk, and J. E. Hoffman, arXiv:1308.1085.
[43] P. P. Baruselli and M. Vojta, Phys. Rev. B **89**, 205105 (2014).
[44] M. Legner, A. Rüegg, and M. Sigrist, Phys. Rev. B **89**, 085110 (2014).